Design of Nanocluster Based Magnetic Materials with Multifunctionality

2000

Tadachika NAKAYAMA

Department of Materials Chemistry
Graduate School of Engineering
Osaka University

JAPAN

Design of Nanocluster Based Magnetic Materials with Multifunctionality

（ナノクラスターによる多機能型磁性材料の設計）

2000

Tadachika NAKAYAMA

Department of Materials Chemistry
Graduate School of Engineering
Osaka University
JAPAN

Preface

The studies presented in this thesis were carried out under the guidance of Professor Koichi Niihara at Department of Materials Chemistry, Graduate School of Engineering, Osaka University.

Nanocluster systems possess many special physical, chemical and biological properties. They have found applications in diverse fields, including materials synthesis, microcontamination, biotechnology, emission control, sensors, electronics, health effects, instrumentation and studies of fundamental transfer processes. However, the nanoscale phenomena and processes are not fully understood and the resulting structures should be controlled and manipulated.

This thesis concerned with a new material design concept for nanocluster based magnetic materials. The development of nanocluster based magnetic materials with multifunctionality was attempted by using both chemical and physical nanoprocessings. This thesis also investigated the influence of various sizes from 1 nm to several μm and dispersions of pure iron, its alloy or oxides on the improved multifunctionality.

The author hopes that the concepts, findings and strategies obtained in this study will contribute to the progress in science and engineering.

Tadachika Nakayama

Tadachika NAKAYAMA
(中山　忠親)

Department of Materials Chemistry
Graduate School of Engineering
Osaka University
2-1, Yamada-oka, Suita, Osaka 565-0871
JAPAN

January, 2000

Design of Nanocluster Based Magnetic Materials with Multifunctionality

Contents

CHAPTER 1

Introduction

1.1 General Introduction

Nanotechnology is concerned with development and utilization of structures and devices with organizational features at the intermediate scale between individual atoms and about 100 nm where novel properties occur as compared to bulk materials [1-5]. It implies the capability to build up tailored nanostructures and devices for given functions by control at the atomic and molecular levels [6,7]. Nanotechnology is recognized as an emerging enabling technology for the 21st century, in addition to the already established areas of information technology and biotechnology. This is because of the scientific convergence of physics, chemistry, biology, materials and engineering at nanoscale, and of the importance of the control of matter at nanoscale on almost all technologies. Nanoparticle manufacturing is an essential component of nanotechnology because the specific properties are realized at the nanocluster, nanoparticle, nanocrystal or nanolayer level, and assembling of precursor particles and related structures is the most generic route to generate nanostructured materials [1-7].

Assemblies of nanoclusters, nanoparticles or nanofibers with an interstitial materials are defined here as "*nanodispersions*" This term will mark the difference as compared to ordinary dispersions because of the specific properties and phenomena developed at nanoscale (dispersed phase dimension or interstitial gap).

1.2 Nanocluster

Materials with grain sizes less than 10 nm defined as "*nanocluster*" have been studied to take advantage of several kinds of effects.

i) New physical, chemical or biological properties are caused by size scaling

ii) New phenomena are related to size reduction to the point where interaction length scales of physical, chemical or biological phenomena becomes comparable to the size of the nanocluster

iii) New atomic, molecular and macro molecular structures of materials are formed by using various nanoprocessing.

iv) The degree of complexity and speed of nanophenomena increase significantly in particulate systems.

Nanoscale phenomena and processes are not fully understood and the resulting structures should be controlled and manipulated. Critical length and time scales, surface and interface phenomena are essential aspects to be defined. Novel mechanical, optical, electric, magnetic, thermal, chemical and biological properties occur as compared to bulk behavior because of the small structure size and short time scale, but only a small part of these properties have been fully identified and quantified [1].

1.3 Nanoprocessing

1.3.1 Overview of Nanoprocessing

Nanoprocessings of nanoclusters, nanoparticles or nanofibers have received wide attention because of their novel properties and important applications in various fields. In view of this, nanoclusters have been widely investigated with investigated with the aim to synthesize powders which are nanosized, highly reactive, highly pure, monodispersed, spherical, and of a narrow size distribution. These particles have a very strong surface effect, and the specific heat, thermal expansion coefficient and magnetic susceptibility are greatly different from those of large grain-

Table 1-I Methods for synthesizing nanosized powders and nanoclusters [8].

Starting phase	Nanoprocessing
Vapor	Inert Gas Condensation (IGC)
	Sputtering
	Cluster Beam Deposition
	Plasma Processing
Liquid	Solution Process
	Physical and Chemical Vapor Deposition
	Electrodeposition
	Rapid Solidification
	Sol-gel Processing
	Hydrothermal Pyrolysis
Solid	Mechanical Alloying/Milling
	Sparc Erosion

sized materials. Hence the nanoprocessing technology of nanoclusters is the cornerstone for the development of nanostructured materials. The various methods were developed to to synthesize nanosized powders and nanocluster (Table 1-I).

1.3.2 Inert Gas Condensation Method

In the inert gas condensation method pioneered by Gleiter and coworkers, a metallic or inorganic material, e.g. a suboxide, is vaporized using thermal evaporation sources such as Joule heated refractory crucibles, electron beam evaporation devices or sputtering sources in an atmosphere of 1 - 50 mbar He (or another inert gas) (Fig.1.1) [2, 9]. Cluster is formed in the vicinity of the source by homogeneous nucleation in the gas phase and grow by coalescence and incorporation of atoms from the gas phase. Granqvist and Buhrman studied the process in detail: the cluster or particle size depends critically on the residence time of the particles in the growth regime and can be influenced by the gas pressure, the kind of inert gas, i.e. He, Ar or Kr, and on the evaporation rate/vapor pressure of the evaporating material [10]. The average particle size of the nanoparticles increases with increasing gas pressure, vapor pressure and mass of the inert gas used. Lognormal size distributions have been found experimentally and have been explained such as the low pressure combustion flame synthesis where a number of chemical reactions are involved the size distributions are determined to be lognormal.

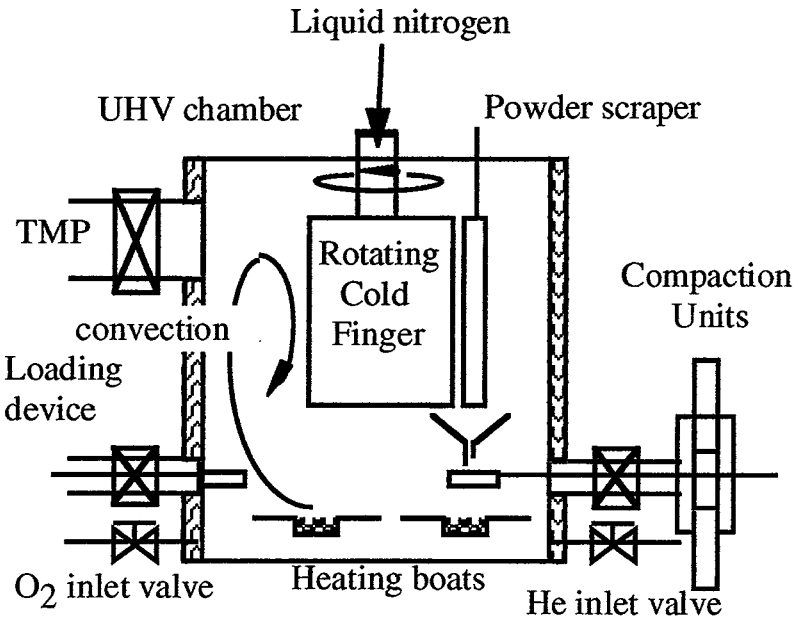

Fig. 1.1 Schematic drawing of inert gas condensation chamber to synthesize the nanocluster composites.

Originally, a rotating cylindrical device cooled with liquid nitrogen was employed for the particle collection: the nanoparticles are extracted from the gas flow by thermophoretic forces and deposited loosely on the surface of the collection device as a powder of low density and no agglomeration. Subsequently, the nanoparticles are removed from the surface of the cylinder by means of a scraper of a metallic plate. In addition to this cold finger device, several techniques known from aerosol science have now been implemented for the use in gas condensation systems such as corona discharge, etc. These methods allow for the continuous operation of the collection device and are better suited for larger scale synthesis of nanopowders. However, these methods can only be used in a system designed for static gas. A major advantage over convectional gas flow is the improved control of the particle sizes. It has been found that the particle size distributions in static gas systems, which are also lognormal, are shifted towards smaller average values with an appreciable reduction of the standard deviation of the distribution [11, 12].

The synthesis of nanocrystalline pure metals is relatively straightforward as long as evaporation can be done from refractory metal crucibles (W, Ta or Mo). If metals with high melting points or metals which react with the crucibles, are to be prepared, sputtering, i.e. for W and Zr, or electron beam evaporation has to be used. Synthesis of alloys or intermetallic compounds by thermal evaporation can only be done in the exceptional cases that the vapor pressure of the constituent elements is similar. As an alternative, sputtering from an alloy or mixed target can be employed. Composite materials such as Fe/Ag, Gd/Ti or Cu/Ce have been synthesized by simultaneous evaporation from two separate crucibles onto a rotating collection device. It has been found that excellent intermixing can be obtained in the scale of the particle size. However, control of the composition of the element is difficult and reproductibility is poor.

1.4 Size Effect of Magnetic Property

The coercive field (coercive force) H_C is defined as the field at which the magnetization is reduced from remanence to zero. For a magnetization loop with peak magnetization M_{max}, $4H_CM_{max}$ gives the order of magnitude of the loop area, which shows that H_C is a measure of the energy dissipation accompanying the magnetization process. Coercive field values span an astonishingly wide interval, from less than 1 A/m (≈0.125 Öe) in very soft Ni-Fe or amorphous alloys to nearly 10^7 A/m(≈1.25×10^5 Öe) in the best hard magnets. There is a great variety of chemical, metallurgical, and structural factors that may substantially affect the coercive field, not to say the influence of geometrical aspects, through shape anisotropy. The hysteresis loop and

coercivity, is not a property of individual volumes of a given element or alloy. Very pure bulk iron may have a coercive field around 1 A/m (≈0.125 Öe), commercial polycrystalline iron around 100 A/m (≈1.25 Öe) , and single domain iron particles beyond 10^4 A/m(≈125 Öe) [13].

The behavior of coercivity in systems made up to fine particles or fine grains is qualitatively summarized in Fig. 1.2 [14]. Permanent magnets and magnetic recording media are examples of systems of this kind. On the abscissa we have the particle diameter D, and on the ordinate the expected coercivity. The size dependence of the coercivity is connected with the domain structure and the grain size. In bulk samples, magnetization reversal occurs due to domain structure and the grain oriented domains grow at the expense of those not aligned with the applied field. As domain walls move through a sample, they can become pinned at grain boundaries, and additional energy is needed for them to continue moving. Pining the main source of the coercivity.

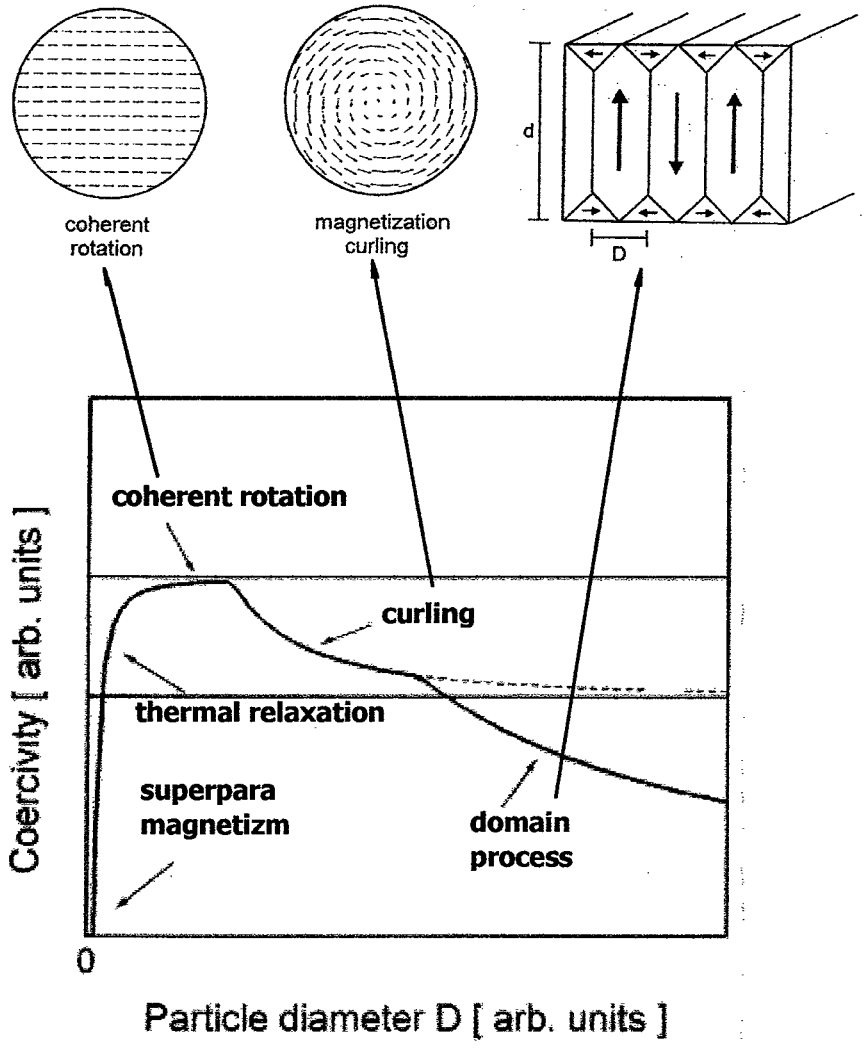

Fig. 1.2 Qualitative behavior of coercivity versus particle diameter.

Therefore, the decrease in the grain size creates more pinning sites and increases H_C. This is true for large grain sizes, but below a certain value, H_C decreases rapidly. This threshold is the maximum size, d_{Cr}, for a single magnetic domain with coherent magnetization reversal, which is predicted to be

$$d_{Cr} = \pi S \left(\frac{J}{K a_0} \right)^{\frac{1}{2}}. \tag{1-1}$$

where S is the spin moment per atom, J is the exchange energy density, and a_0 is the lattice constant. Single domain sizes range from ≈45 nm in bcc Fe to ≈2 μm for $SmCo_5$. In single domain particles with $d < d_{Cr}$, such as the nano particle, the spins coherently rotate their direction while maintaining their ferromagnetic coupling to reverse the particle magnetization. The energy needed to rotate the spins depends on the number of spins. Therefore, H_C decreases as the particle size is reduced for single domain particles.

Below another size threshold, the coercivity drops to zero, and the particles are to be superparamagnetic [15]. Until now, we have ignored thermal effects, but they are also important in determining magnetic behavior. Above the *Curie* temperature of a ferromagnet, there is sufficient thermal energy to overcome the magnetic forces which tend to align the spins, and the material becomes paramagnetic, but thermal forces are still active well below this temperature. A soft material like an iron nail can be magnetized in a strong field. For a short time, the nail itself attracts other ferromagnetic objects, but this ability decays in different directions. Magnetic recording media are made from harder magnetic materials so that thermal fluctuations are unlikely to erase information.

Superparamagnetic particles have single magnetic domains, but they are small enough that thermal fluctuations can easily reverse the direction of their magnetic moment [16]. The experimental signature of superparamagnetism is $H_C = 0$ and a magnetization proportional to a Langevin function, $L(a)$,

$$\frac{M}{M_S}(T=0) = L(a) = \coth(a) - \frac{1}{a} \quad . \tag{1-2}$$

where T is the temperature, and $a = \mu H/kT$, and $\mu = M_S V$ is the particle magnetic moment. Whether or not the particle moment is reversed depends both on the timeframe of the magnetization measurement and the time required for equilibration [17].

1.5 Mechanical Sensing

The mechanisms responsible for magnetocrystalline anisotropy also give rise to energy variations when the relative position of the magnetic ions in the lattice is modified, that is, when the lattice is distorted. Due to the presence of this magnetoelastic coupling to the lattice, the system will spontaneously deform in order to minimize its total free energy, and the ensuing deformation will be a function of the magnetic state of the system [18]. The phenomenon, in which a magnetic material gets deformed when it is magnetized, is called magnetostriction. A complementary role is played by the so-called inverse magnetostrictive effect, or stress anisotropy, in which, again through magnetostrictive coupling, the deformation produced in the system by an externally applied stress makes certain magnetization directions energetically favored, so that the system will tend to align its magnetization to those directions [19].

Magnetostrictive materials reveal the large change of magnetoelastic energy at an applied stress as given in the following equation.

$$E = \frac{3}{2}\lambda\sigma\sin^2\theta \qquad (1\text{-}3)$$

where, E is the magnetoelastic energy, λ is the appropriate magnetostrictive constant, σ is the applied uni-axial stress, θ is the angle between magnetic field and anisotropic axis[20]. As the result of change of the magnetoelastic energy, saturation magnetization and permeability in an relationship should be shifted as shown schematically in Fig. 1.3 [21].

This magnetization change under applied stress has opened up a range of possibilities for the utilization of ferromagnetic materials in practical applications such as the remote sensing of the mechanical stress [22, 23].

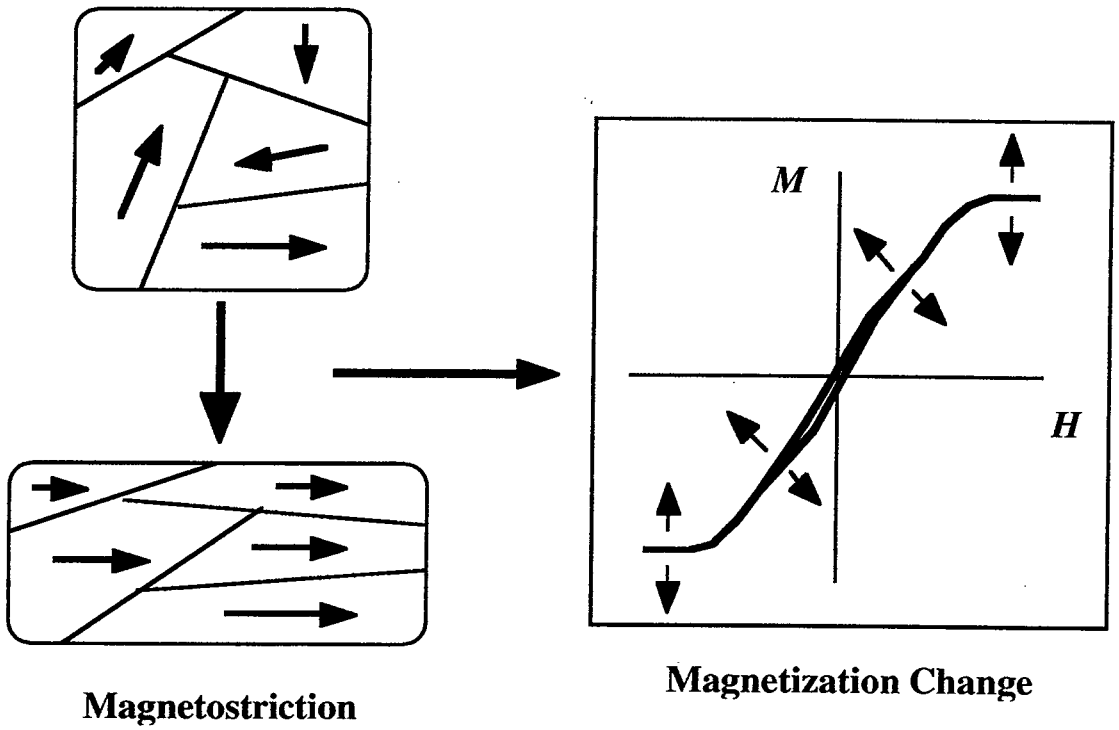

Fig. 1.3 Schematic drawings of remote sensing of applied stress by magnetostrictive effect in a ferromagnetic material.

1.6 Materials Advances Magnetic Refrigeration

1.6.1 Magnetic Refrigeration

Magnetic refrigeration exploits the magnetocaloric effect, the remarkable ability of some metals to be hot when magnetized and cool when demagnetized [24, 25]. Some of the major losses present in conventional gas-compression refrigerators are absent in magnetic refrigerators, and thus it is expected that cooling systems based on this new technology can attain substantially higher efficiency than conventional gas-compression coolers [26-28].

A key difference between vapor cycle refrigerators and magnetic refrigerators is the amount of energy loss incurred during the refrigeration cycle. In current vapor cycle refrigerators, energy loss during compression/expansion is significant. There is virtually no energy loss during magnetizing/demagnetizing in magnetic refrigerators. Magnetic refrigerators can reach levels of efficiency as high as 60 percent of the theoretical limit, compared to only about 40 percent efficiency for the best conventional gas-compression refrigerators. Therefore, there is a potential to reduce total energy consumption on refrigeration needs as much as 30 percent compared to current

levels [29].

Another advantage of magnetic refrigerator is not to utilize ozone-damaging chlorofluorocarbons (CFCs), hydrochlorofluorocarbons (HCFCs) and ammonia as a heat transfer medium, thereby eliminating a substantial environmental threat. Near-room temperature magnetic refrigerators use water as a heat transfer medium. Antifreeze can be added to the water to prevent freezing for sub-zero temperature applications [28].

Further development of magnetic refrigeration could lead to the production of cheap liquid hydrogen, an environmentally safe and endless alternative energy source. Magnetic refrigeration can efficiently span the large temperature difference needed to produce liquid hydrogen. Because of this large temperature difference, even a small improvement in efficiency would result in huge energy savings [28, 29].

1.6.2 Magnetocaloric Effect of Nanocluster Composite

The present magnetic refrigeration system employing a paramagnetic working substance such as gadolinium gallium garnet works only lower than about 30 K and needs a field of several Tesla obtained usually by a superconducting magnet [30]. If a new material makes the magnetic refrigeration system to work under moderated magnetic field such as those with permanent magnets and/or at temperatures around liquid nitrogen temperature, it would impact the industry by developing new applications [31]. To approach this ultimate objective, a breakthrough in materials science is necessary and urged [32-35].

The superparamagnetism occurs when single domained ferromagnetic grains are distant too far to magnetically interact each other, and their crystalline anisotropic energies are smaller than thermal energy at a given temperature. This magnetism is simplest of novel magnetisms that may occur in magnetic nanocomposites, so that it is easy to study its magnetic behavior in comparison with the relevant theoretical model [34]. On the basis of the model of magnetical phase transition, the superparamagnet is predicted to enhance the magnetocaloric effect because of its nanostructures [35].

In this work, magnetic entropy change, ΔS, of the samples was evaluated from their data sets of $M-H$ relations measured at various temperatures, T, where M is magnetization, H applied magnetic field. By using thermodynamic Maxwell's relation,

$$\left(\partial S / \partial H\right)_T = \left(\partial M / \partial T\right)_H, \tag{1-4}$$

these data set was converted into ΔS accompanied by a demagnetization, $H \rightarrow 0$, at T.

$$\Delta S = \int_H^0 (\partial S / \partial H)_T dH = \int_H^0 (\partial M / \partial T)_H dH . \tag{1-5}$$

This ΔS was numerically calculated by substituting the magnetization data, in which differentials and integrals were replaced with finite differences and trapezoid areas, respectively. Equation (1-6-1) is valid only when M is regarded as a state property determined by independent variables of T and H. The ideal superparamagnet has magnetization described as vector sum of magnetic moment vectors which are independent of each other, which is expressed by using Langevin function $L(x)$ as,

$$M = N\mu L(x), \tag{1-6}$$

$$L(x) = \coth x - 1/x, \tag{1-7}$$

where $x = \mu H / k_B T$, k_B is the Boltzmann's constant, μ is size of the elemental moment, N is number of moments existing in the substance. By inserting eqs. (1-6) and (1-7) into eq. (1-5), formulation for ΔS of the ideal superparamagnet is obtained as

$$\Delta S / N k_B = -1 + x \coth x - \ln\{(\sinh x)/x\}. \tag{1-8}$$

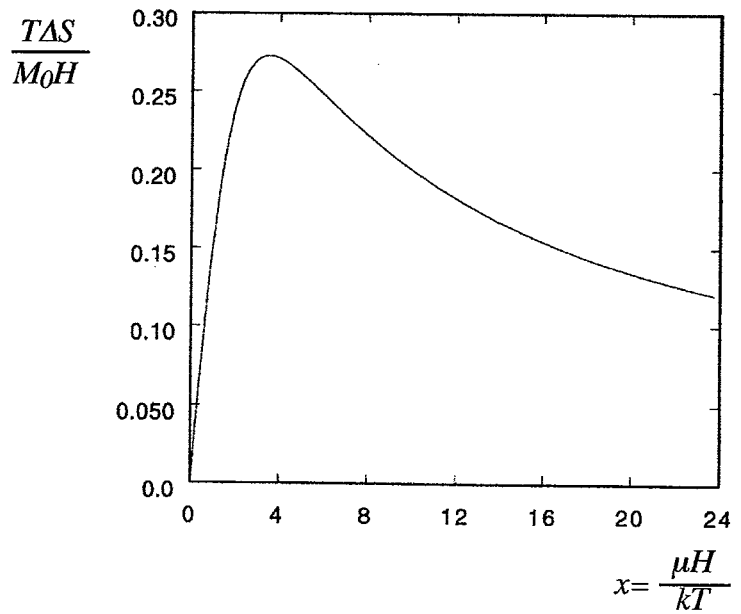

Fig. 1.3 Entropy change ΔS of a superparamagnet as a function of the unit moment μ, induced by removal of a field H at a temperature T.

This equation gives the magnetic entropy change from each grain, which is illustrated in Fig. 1.3. This curve has the maximum at

$$x = \frac{\mu H}{kT} \approx 3.5. \tag{1-9}$$

Assuming that M_0, T and H are constant values, eq. (1-8) is a function of only μ [35]. It should be noticed that a performance of a nanocluster composite would be optimized by adjusting the unit moment, μ, in material [35, 36].

References

[1] K. Niihara, *Materials Integration*, **12** (1999) 3.
[2] H.Gleiter, *Progress Materials Science*, **33** (1989) 223.
[3] H. Gleiter, *Nanostruct. Materials*, **6** (1995) 3.
[4] R.W. Siegel, *Nanostruct. Materials*, **3** (1993) 3.
[5] R.D. Shull, *Nanostruct. Materials*, **2** (1993) 213.
[6] C.L. li, D.-H. Riu, T. Sekino and K. Niihara, *Key Eng. mat.*, **161-163** (1999) 161.
[7] D.-H. Riu, C.L. Li, H.-E. Kim and K. Niihara, *Key Eng. mat.*, **161-163** (1999) 521.
[8] C. Suranarayana, Int. Mater. Rev., **40** (1995) 41.
[9] H.W. Hahn, J.A. Eastman, R.W. Siegel, *Ceramic Transactions*, **1b** (1988) 1115.
[10] C. Granqvist, R. Buhrman, *J. Appl. Phys.*, **2200** (1976) 47.
[11] H.W. Hahn, *Nanostruct. Materials*, **9** (1997) 3.
[12] T. Yamamoto, M. Adachi, K. Kawabata, K. Kimura, H.W. Hahn, *Appl. Phys. Lett.*, **63** (1993) 3020.
[13] F.E. Luborsky and T.O. Paine, *J. appl. Phys.*, **31** (1960) 68S.
[14] G. Bertotti, "*Hysteresis in Magnetism*", Academic Press, Inc. (1998) p. 375.
[15] M. Blanco-Mantecon, K. O'Grady, *J. Magn. Magn. Mater.*, **203** (1999) 50.
[16] B.D. Culity, : "*Introduction to Magnetic Materials*", Addison-Wesley, Reading, MA (1972) p. 410.
[17] H.D. Williams, K. O'Grady, M. El-Hilo, R.W. Chantrell, *J. Magn. Magn. Mater.*, **122** (1993) 129.
[18] S. Tikazumi, : "*Kyoziseitai-no-Butsuri*", Syokabo Press, (1984) p. 112.
[19] T. Honda, K. Arai and M. Yamaguchi, *J. Appl. Phys.*, **76** (1994) 6994.
[20] B.D. Culity, : "*Introduction to Magnetic Materials*", Addison-Wesley, Reading, MA (1972) p. 266.
[21] M. Awano, M. Sando and K. Niihara, *Proceedings of the 14th International Japan-Korea Seminar on Ceramics* (Kanazawa, Japan, 1997) p. 172.
[22] S.-T. Oh, M. Sando and K. Niihara, *Scripta Mat.*, **39** (1998) 1413.
[23] S.-T. Oh, M. Sando and K. Niihara, *J. Am. Ceram. Soc.*, **81** (1998) 3013.
[24] J.R. van Geuns, *Phillips Rep. Suppl.*, **1** (1966) 6.
[25] G. V. Brown, *J. Appl. Phys.*, **47** (1976) 3673.
[26] T. Hashimoto, T. Ikegami and T. Osada, *Jpn. J. Appl. Phys.*, **19** (1980) L215.
[27] T. Hashimoto, T. Numazawa, M. Shiino and T. Okada, *Cryogenics*, **21** (1981) 647.
[28] K.A. Gschneidner, Jr., *Adv. Cryog. Engin.*, **39** (1994) 1457.

[29] V.K. Pecharsky and K.A. Gschneidner, Jr., *Adv. Cryog. Engin.*, **42** (1996) 423.
[30] H. Nojiri, Y. Shimamoto, N. Miura, M. Hase, K. Uchinokura, H. Kojima, I. Tanaka and Y. Shibuya, *Phys. Rev. B*, **52** (1995) 12749.
[31] L.H. Bennett, R. D. McMichael, R. D. Shull and L. J. Swartzendruber, *J. Appl. Phys.*, **73** (1993) 6507.
[32] R.D. Shull, J.P. Cline, I. Bakler and F. Liu, *J. Appl. Phys.*, **79** (1996) 6028.
[33] R.D. McMichael, J.J. Ritter and R.D. Shull, *J. Appl. Phys.*, **73** (1993) 6946.
[34] L. H. Bennett, R. D. McMichael, L.J. Swartzendruber, R. D. Shull and R. E. Watson, *J. Magn. Magn. Mater.*, **104-107** (1992) 1094.
[35] R.D. Shull, H.M. Kerch and J.J. Ritter, *J. Appl. Phys.*, **75** (1994) 6840.
[36] T.A. Yamamoto, M. Tanaka, K. Shiomi, T. Nakayama, K. Nishimaki, T. Nakagawa, T. Numazawa, M. Katsura and K. Niihara, "*Proceedings of Material Research Society Symposium* " (in press).

CHAPTER 2

Fabrication of Magnetic Alloy Dispersed MgO Based Nanoparticles for Multifunctional Nanocomposite

2.1 Introduction

Iron metal and its oxides (and its alloys) are rather sensitive to conditions of synthesis, which may affect its morphological and structural properties [1-7]. Some properties of iron based materials are summarized in Table 2-I [1]. When these materials are synthesized at low temperatures, highly reactive materials of small particle size and high surface area are produced [8-11]. These materials play an important role in many industrial applications such GMR [12-17], magnetic recording media [18, 19] , catalysis, photocatalysis and adsorption [20-22] and pigment technologies [23, 24]. In particular, the GMR has been observed in metal-insulator films such as Co-Al_2O_3 [13], Fe-SiO_2 and Fe-MgO [14] when the volume fraction of the magnetic component is below the percolation threshold. In these cases, metal-insulator system show superparamagnetic behavior and the spin-dependent tunneling process is important.

Most applications are extremely sensitive to the surface-related properties. Traditionally, the ceramic method involving high reaction treatments was used for their synthesis. In contrast, current research efforts are focused towards the development of low temperature synthesis methods in order to prepare materials of easily designed and controlled surface area and particle size [8-11].

Recently, chemical processing was applied to fabricate Al_2O_3/Ni [25-29], ZrO_2/Ni [30] and MgO/Ni [31] nano-sized mixture. From these researchers, the chemical processing is thought to be the most promising method to realize desirable microstructures in ceramic/metal systems. Also, this method allowed the total recovery of the nickel or cobalt content from the industrial waste as Ni and Co, a material of highly added value.

The present investigation describes the application of the above procedure to the synthesis of Fe, FeNi and FeCo and MgO mixture. The nanostructure and magnetic properties relationships will be also discussed.

Table 2-I Summary of properties of magnetic materials

Material	Molecular Weight	density	T_c [K]	$\mu_0 M_S$ (R.T.) [T]	M_S (R.T.) [emu/g]	μ (0 K) [μ_B]	K_1 [10^5 Jm^{-3}]	λ_S [$\times 10^6$]
Fe	55.847	7.874	1044	2.16	217.2	2.216	0.48	-9
Co	58.9332	8.9	1388	1.82	164.8	1.715	5.28	
Ni	58.69	8.908	631	0.62	55.1	0.616	-0.057	-35
FeCo (Permendur)	57.39	8.387	1373	2.45	230.1	2.425		+65
FeNi (Permalloy)	57.27	8.391	816	1.60	151.6	1.7		+28
Fe_3O_4 (Magnetite)	231.6	5.24	858	0.60	98.0	4.1	-0.13	+40
γ-Fe_2O_3 (Maghemite)	159.7	5.07	848	0.52	81.0	2.3	-0.046	-5
Gd	157.25	7.895	293	0.00	0.0	7.56		
$Nd_2Fe_{14}B$	1081.121	7.60	585	1.61	169.8	28.8 (R.T.)	50	

R.T. : Room temperature

T_c : Curie temperature

$\mu_0 M_S$: Spontaneous magnetic polarization

M_S : Spontaneous magnetization

μ : magnetic morment per unit cell

K_1 : uniaxial magnetic anisotropy

λ_S : magnetostrictive constant

2.2 Experimental Procedure

2.2.1 Preparation of Materials

The solution chemistry route was selected to obtain the powder mixtures used for the composites. High-purity Fe, Ni and Co-nitrate ($Fe(NO_3)_3 \cdot 9H_2O$, $Ni(NO_3)_2 \cdot 6H_2O$) and $Co(NO_3)_2 \cdot 6H_2O$) (Wako Pure Chemical Industries, Ltd., Japan) were used as source materials for metal dispersion. Weighted nitrate corresponding to 0 to 40 vol% of metal in final specimens was dissolved in alcohol. Subsequently, MgO powder (average particle size ≈ 100 nm) (Ube Material Industries, Ltd., Japan) was mixed with above-mentioned solution and ball-milled for 24 hr. After dried, the mixtures were dry ball-milled for 12 hr and calcined at 673 K for 3 hr in air to obtain MgO/oxides (γ-Fe_2O_3, NiO and CoO) mixed powders. The obtained oxide powder mixtures were reduced to MgO/metal or alloy under hydrogen gas flow at 1373 K for 1 hr. During this processes, MgO was not reduced by hydrogen.

2.2.2 Phase Analysis and Characterization

Simultaneous thermogravimetry and differential thermal analyses (TG-DTA) (DTG-50, SHIMADZU Ltd., Japan) of the MgO/iron nitrate mixtures were performed in air at a heating rate of 10 K/min up to 673 K. The phase composition of the powders was examined by X-ray diffraction (XRD) using Cu*ka* radiation (Model DMS-2000 system, Scintag Co., U.S.A) even at high temperatures. Scanning electron microscopy (SEM) (Model S-5000, Hitachi Ltd., Japan) with energy dispersive X-ray spectroscopy (EDS) (EMAX-5770, HORIBA Ltd., Japan) and transmission electron microscopy (TEM) (Model H-8100, Hitachi Ltd., Japan) were used to observe the morphology of composite powders and the microstructures of sintered materials.

2.2.3 Magnetic Properties

Magnetization measurements at room temperature were performed by a SQUID magnetometer (Model, MPMS-5, QUANTUM DESIGN, USA) with a maximum field at 10 kÖe (=1 Tesla). Low-field magnetization versus temperature measurements in field cooled (FC) and zero-field cooled (ZFC) states were made in the following way. The sample was demagnetized at 300 K, and then cooled to 5 K in 30 Öe (=0.003 Tesla) and zero field, respectively. And the magnetization was measured in 30 Öe at each temperature up to 300 K.

2.3 Results and Discussion

2.3.1 Phase Composition of Powders

TG-DTA curves of the MgO/Fe-nitrate mixtures (corresponding to MgO/20 vol% Fe composite powder) shown in Fig. 2.1 demonstrate that almost all weight loss occurs below 673 K due to the loss of water of hydration and the decomposition of the nitrate salts. After further heating for 1 hr at 673 K, the weight loss was complete.

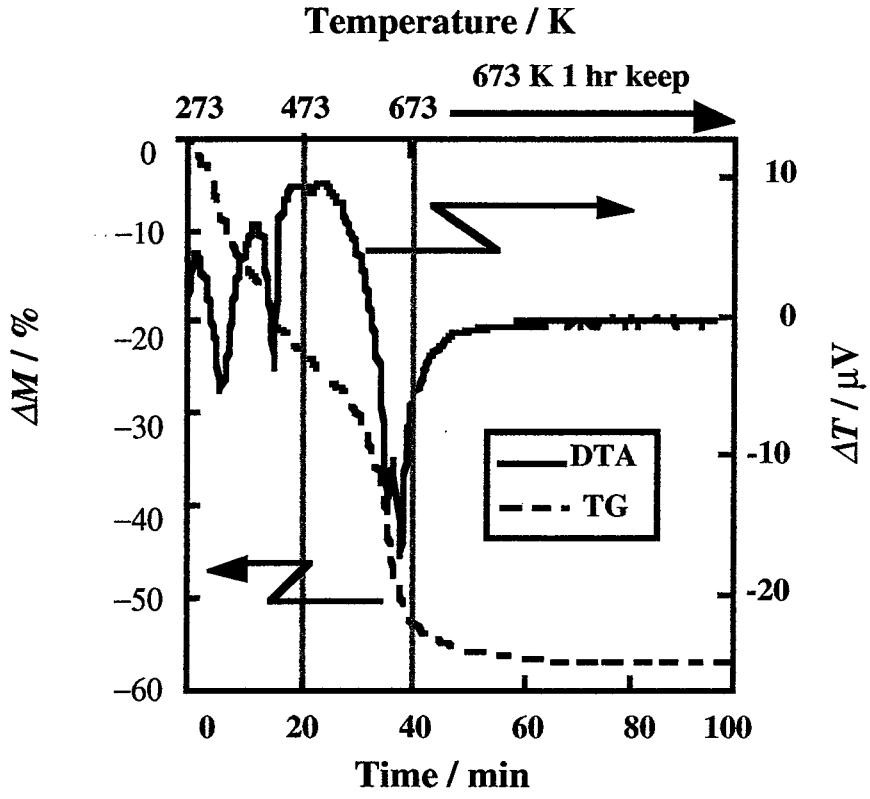

Fig. 2.1 TG-DTA curves for MgO/Fe-nitrate mixtures (heating at 10 K/min up to 673 K).

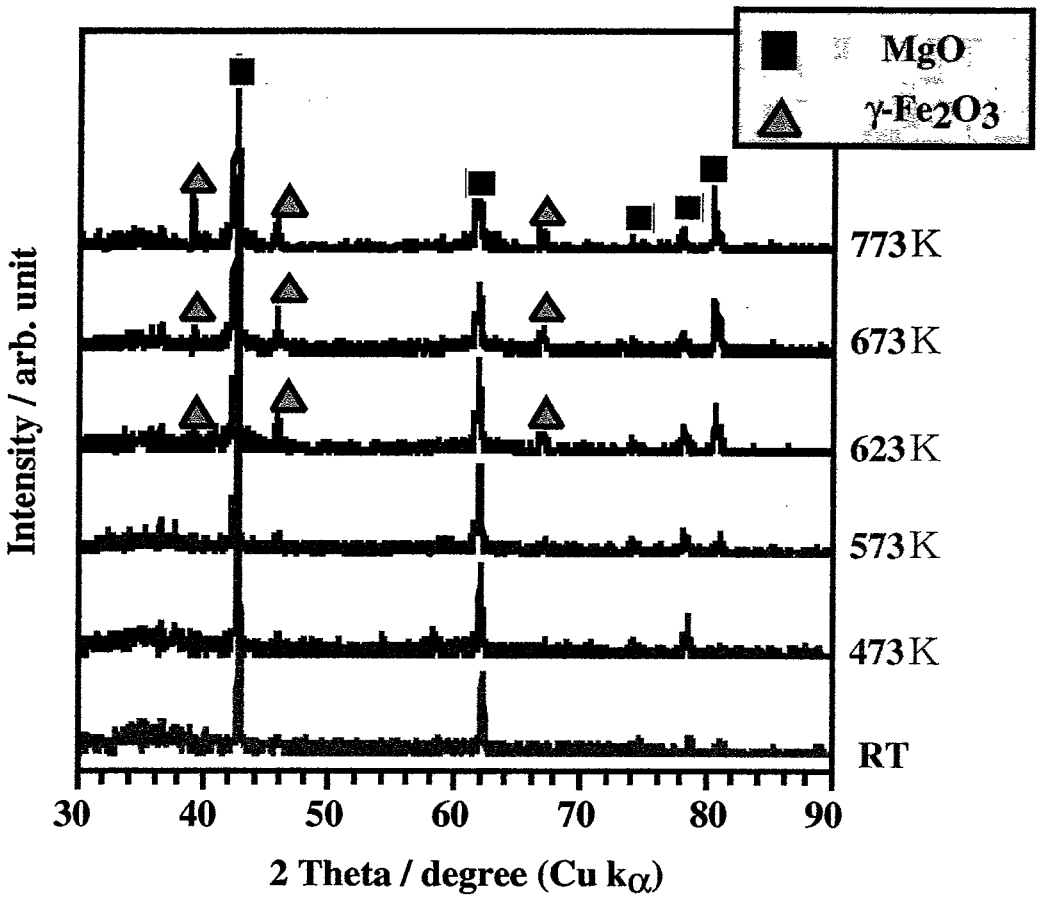

Fig. 2.2 High temperature XRD profiles for MgO/Fe-nitrate mixtures heated in air.

High temperature XRD patterns for MgO/Fe nitrate mixtures are shown in Fig. 2.2. γ-Fe_2O_3 appeared above 573 K. No reaction phases such as Mg- spinel was observed in this experiment. From these results, the calcination temperature was to be 673 K for MgO/Fe nitrate mixtures.

The XRD patterns for the MgO/20 vol% Fe composite prepared by calcining, reducing, and subsequent sintering processes are shown in Fig. 2.3. The XRD pattern after drying contains the characteristic peaks for MgO, $Mg(OH)_2$ and $Fe(NO_3)_3 \cdot 9H_2O$ (Fig. 2.3 (a)). After calcined at 673 K, the Fe nitrate forms γ-Fe_2O_3 (Fig. 2.3 (b)). No reaction phases such as Mg spinel was observed in this experiment. After reduced at 1373 K, γ-Fe_2O_3 is reduced to metallic iron and no reaction phases are observed (Fig. 2.3 (c)). In addition, MgO matrix was not reduced in this experiment.

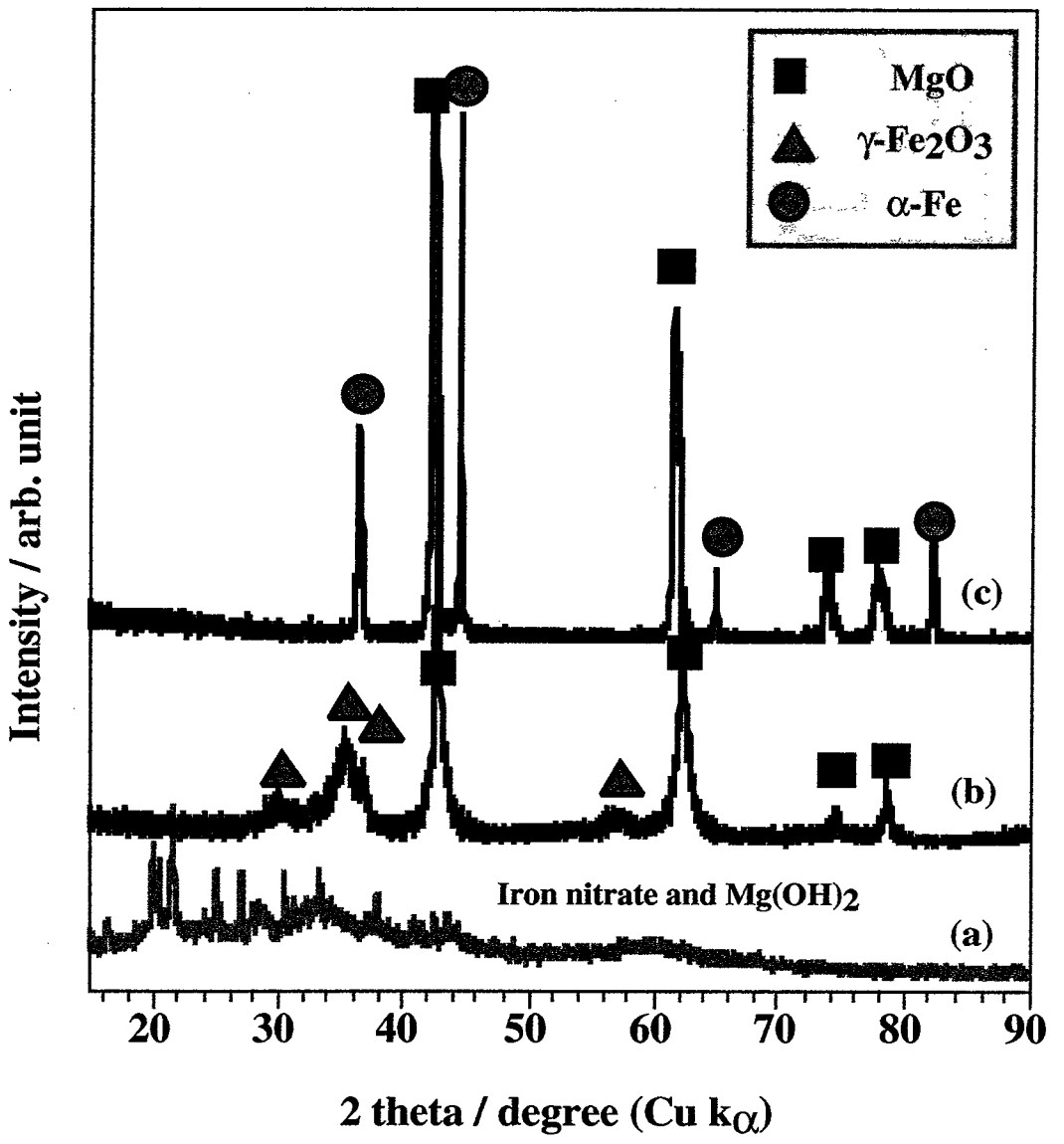

Fig. 2.3 XRD profiles for the starting mixtures prepared by solution chemistry route for the mixture of MgO and $Fe(NO_3)_3 \cdot 9H_2O$ after drying (a), after calcination in air (b) and after reduction (c).

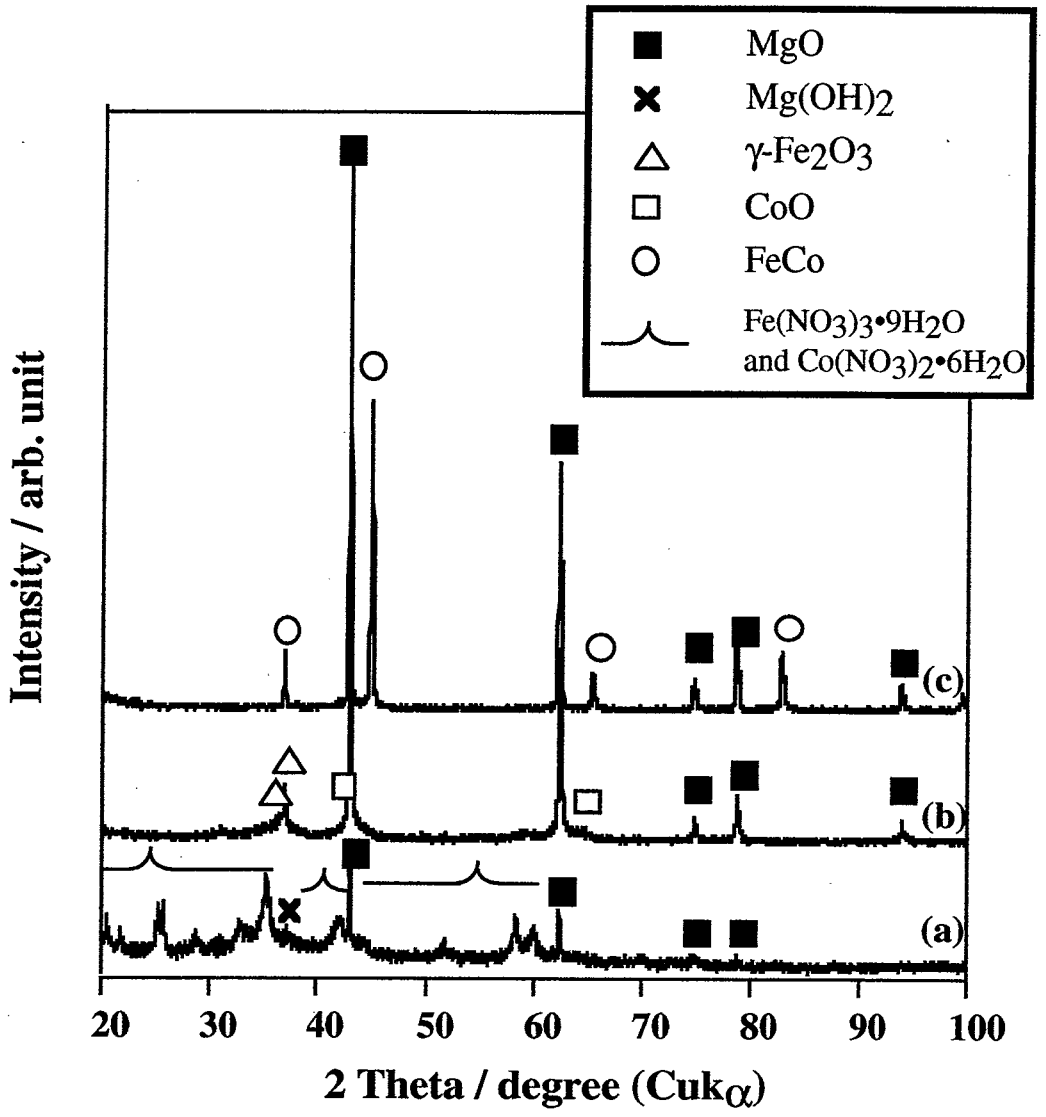

Fig. 2.4 XRD patterns for the starting mixtures prepared by solution chemistry route for the mixture of MgO, $Fe(NO_3)_3 \cdot 9H_2O$ and $Co(NO_3)_2 \cdot 6H_2O$ after drying (a), after calcination (b) and after reduced (c).

The XRD patterns for the MgO/Fe-Co composite prepared by calcining and reducing processes are shown in Fig. 2.4. This system also shows almost same results as MgO/Fe system (Fig. 2.3). The XRD pattern after drying contains the characteristic peaks for MgO, $Mg(OH)_2$, $Fe(NO_3)_3 \cdot 9H_2O$ and $Co(NO_3)_2 \cdot 6H_2O$(Fig. 2.4 (a)). After calcination at 673 K, the iron and cobalt nitrate form γ-Fe_2O_3 and CoO(Fig. 2.4 (b)). After reduced at 1373 K, γ-Fe_2O_3 and CoO vary to iron-cobalt alloy and no reaction phases are observed (Fig. 2.4 (c)). In addition, MgO

matrix was not reduced in this experiment. No cobalt spinel was also identified under this condition.

The key phenomenon in the fabrication process was the reduction of additives to metallic second phases. The thermodynamic conditions of reduction process for Al_2O_3/Ni nanocomposites have been well accomplished by Sekino *et. al.*[27]. To reduce the nickel, cobalt and iron oxides in present experimental condition, the calculated reduction temperature from the Ellingham diagram was 973, 1073 and 1273 K (see Fig. 2.5) [32]. However, because the actual experimental condition (reduction temperature and time) depends on the amounts of powder (20 to 50 grams for 1 batch for reduction) and the components of mixture powders (corresponding to 5 and 40 vol% of each metal in the final mixtures), the oxide mixtures were reduced to MgO/Fe, Fe-Ni and Fe-Co under hydrogen gas flow at 1373 K for 2 h. Below this reduction temperatures for each mixture, the remainder of oxide phases were observed.

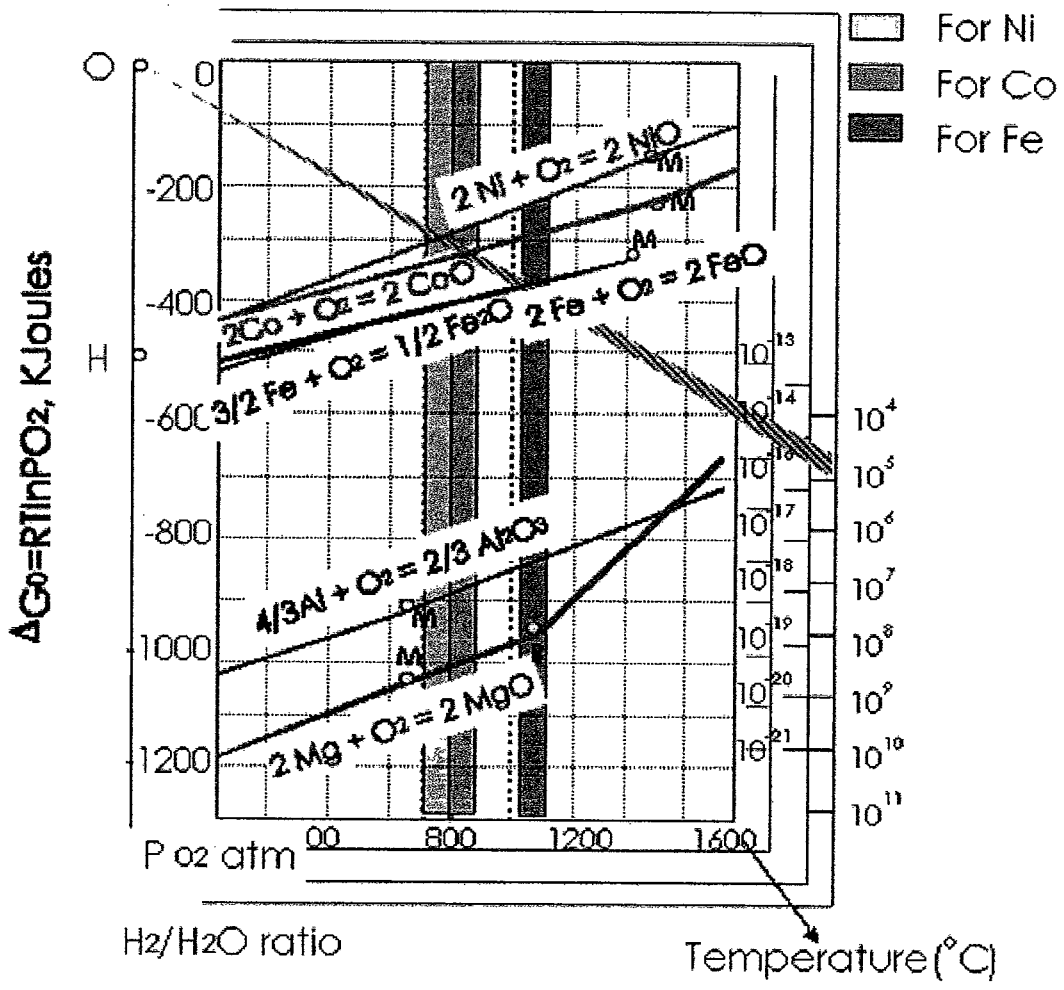

Fig. 2.5 Ellingham diagrams of Mg-O, Fe-O, Ni-O and Co-O systems.

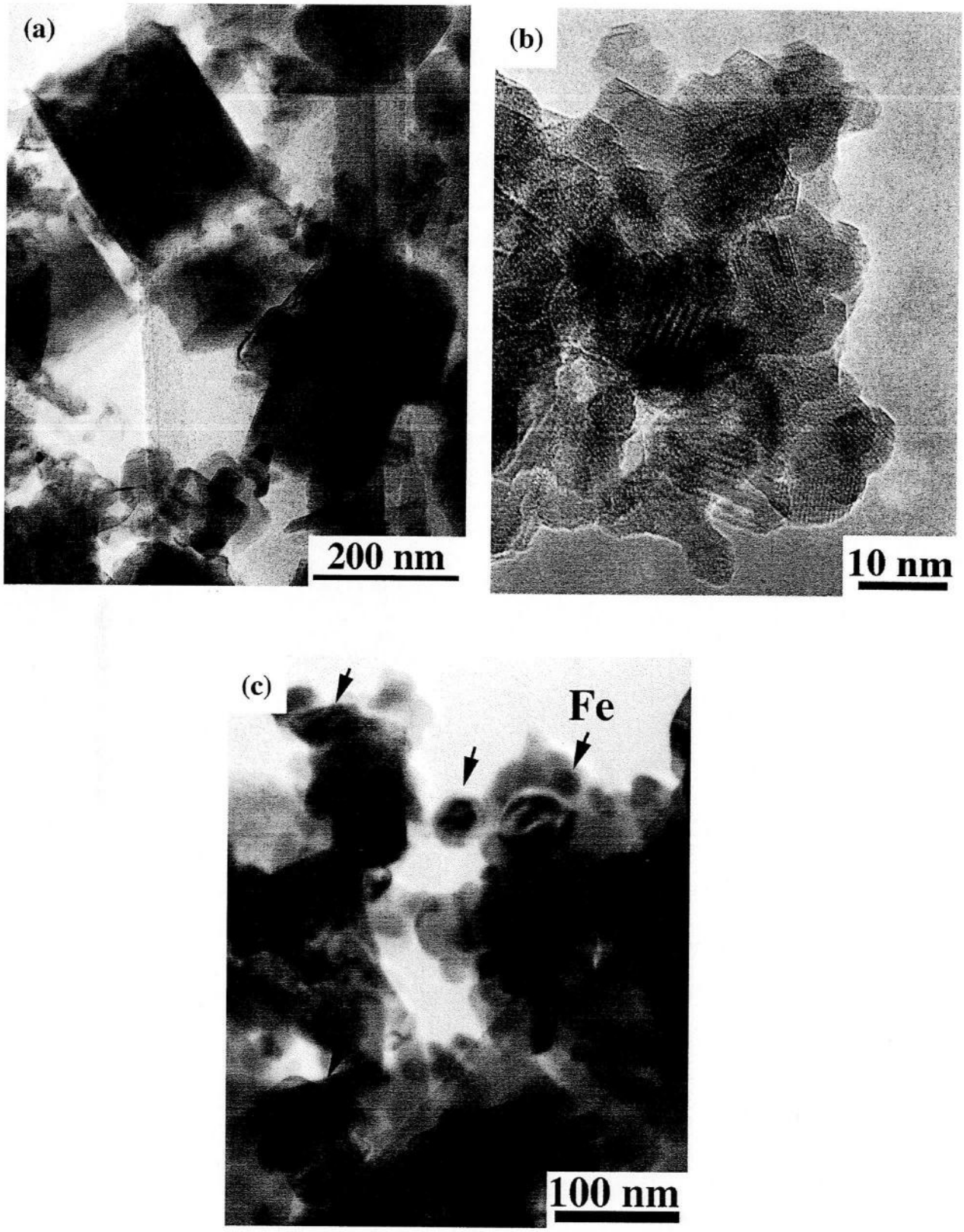

Fig. 2.6 TEM micrographs of (a) as received MgO powder, (b) after calcined MgO/20 vol % γ-Fe_2O_3 mixture and (c) after reduced MgO/20 vol % Fe mixture.

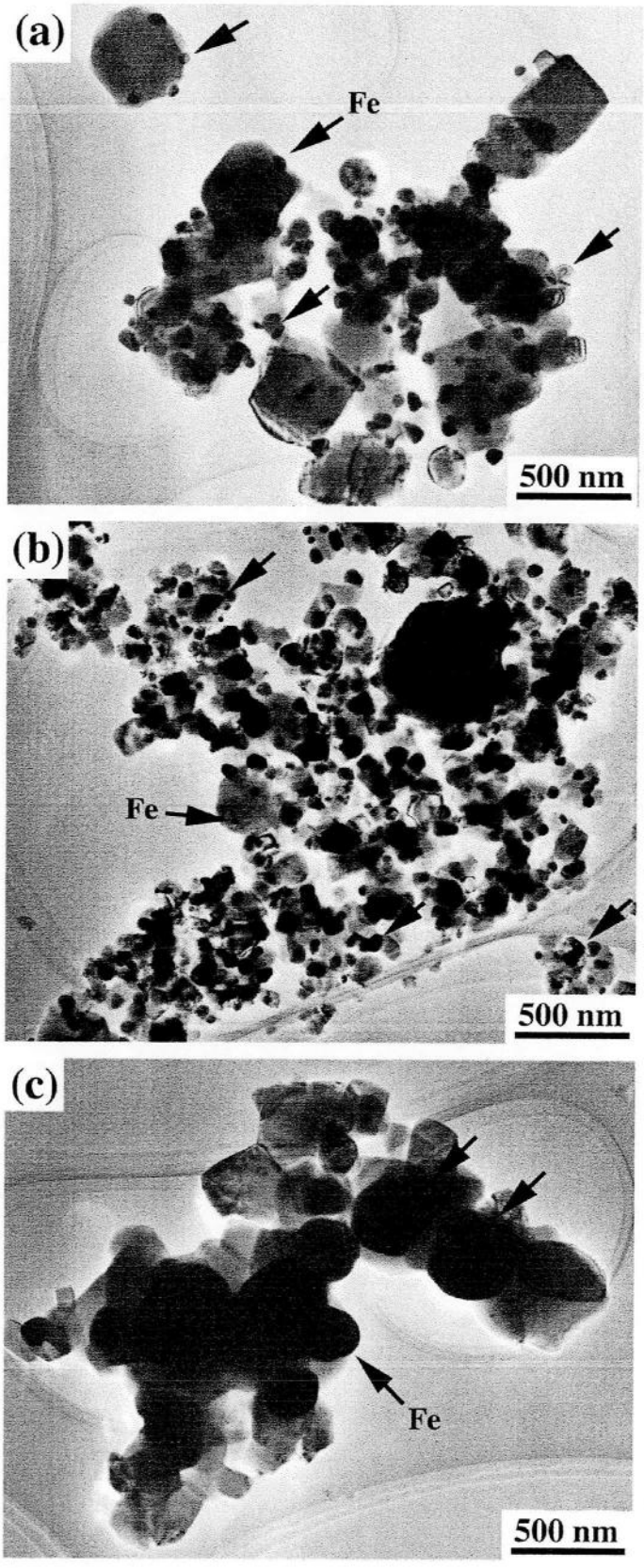

Fig. 2.7 TEM micrographs of MgO and (a) 5 vol.%, (b) 10 vol.% and (c) 20 vol.% Fe-Co alloy reduced mixture (1373 K).

The XRD analysis revealed $Mg(OH)_2$ peaks before calcination as shown (a) in Fig. 2.3 and 2.4. The reason to identify the $Mg(OH)_2$ phase may be found in the hydrationof the MgO powder. The composite powders contain a large amount of water from nitrate. Because chemical stability of MgO toward the hydration is relatively easy [33], specially the hydration and deliquescence will be enhanced during the wet-milling process.

Thus, a part of MgO powder reacted with water in nitrate, and sequentially the particle size of MgO is decreased when $Mg(OH)_2$ decomposed to MgO by calcination at 673 K (eq. (3)).

$Fe(NO_3)_3 \cdot 9H_2O$ + alcohol ---> $Fe(NO_3)_3 + 9H_2O$ + alcohol (1) (in alcohol)

$MgO(s) + H_2O(l)$ ---> $Mg(OH)_2$ (s) (2) (during the wet-milling)

$Mg(OH)_2$--->$MgO+H_2O(g)$ (3) (during the calcination)

This feature is easily understood by the fact that the XRD analysis reveals peaks of $Mg(OH)_2$ peaks before calcination as shown Fig. 2.3 (a) and Fig. 2.4(a).

2.3.2 Morphology of Powder Mixtures

The morphological characteristics of the mixtures were investigated by TEM for (a) as received MgO powder, (b) after calcined MgO/20 vol % γ-Fe_2O_3 mixture and (c) after reduced MgO/20 vol % Fe mixture (Fig. 2.6). A surprising result is that the particle size of MgO with around 100 nm (see Fig. 2.6 (a)) decreases into 9 nm for MgO and γ-Fe_2O_3 mixture after calcined at 673 K for 3 hr. These unique observations will be contributed to the hydration (the formation of $Mg(OH)_2$) of the MgO powder. This fact shows that MgO and γ-Fe_2O_3 nanocluster mixture are easily and economically fabricated by chemical solution process.

After hydrogen treatment at optimized reduction temperature, the source materials for Fe to be reduced to elemental metallic nanoparticles were identified by XRD analysis (see Fig. 2.3). The particle size of iron is about 40 nm (Fig. 2.6 (c)). And TEM observation showd that, the iron nanoparticle existed not only outside of MgO nanoparticle but also inside of the MgO nanoparticle, as seen from Fig. 2.6.

Figure 2.7 shows TEM micrograph of the reduced powders of MgO/FeCo system. This system also show almost same morphology of MgO/Fe system (Fig. 2.6(c)). Fine FeCo alloy particles were found to precipitate uniformly outside and inside the MgO particles even after reduction process. In general, the magnetic particles are easily connected into a chain owing to their magnetism [12] Nevertheless, the magnetic particles show good dispersion and these are not

connected each other.

In case of MgO/5 and 10 vol.% FeCo alloy, the particle size of FeCo alloy was almost same (40-60 nm). The distance of the particles in the sample MgO/10 vol.% FeCo alloy is relatively shorter than the sample MgO/5 vol.% FeCo alloy. In the case of MgO/20 vol.% FeCo, on the contrary, the particle size of FeCo alloy was dramatically increased (270 nm). As a result, the size and distance of the nano-sized particles could be varied by changing the composition of FeCo in the system.

2.3.3 Magnetic Properties of Powders

It was found that the after-calcined mixtures have no significant width of the hysteresis loop at room temperature for the MgO/20 vol% γ-Fe_2O_3 mixture (Fig. 2.8). Quarter loops were measured sequentially by cooling down the sample in the maximum field. Magnetization data sets measured at these temperatures were plotted against, *H/T*. Where *T* is temperature and *H* is applied magnetic field. The data points fall onto a single curve in a temperature range as shown in Fig. 2.8, providing evidence for the occurrence of the Langevin superparamagnetism above 100 K. This facts show that these powder mixtures contain the single domain magnetic particles in nanometer size.

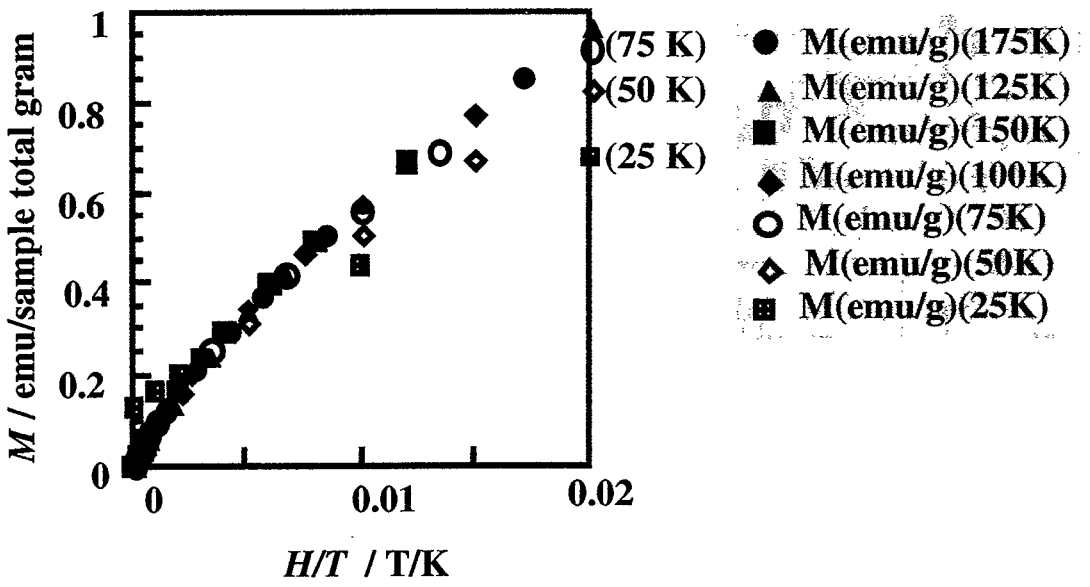

Fig. 2.8 *M* vs *H/T* plots indicating superparamagnetism occurrence in the MgO/20 vol.% γ-Fe_2O_3 mixture.

Figure 2.9 shows 30 Öe field cooled (FC) and zero-field cooled (ZFC) magnetization as a function of temperature measured in 30 Öe in the MgO/20 vol% γ-Fe_2O_3 mixture. The peak in the ZFC curve is generally associated with the mean superparamagnetic blocking temperature (T_B). The mean superparamagnetic blocking temperature is referred to the mean magnetic particle size and mean distance between magnetic particles [34-36]. The mean superparamagnetic blocking temperature of MgO/γ-Fe_2O_3 20 vol.% mixtures (Fig. 2.9 (a)) is higher than that of MgO/γ-Fe_2O_3 10 vol.% mixtures (Fig. 2.9 (b)). These results are in good agreement with TEM observations.

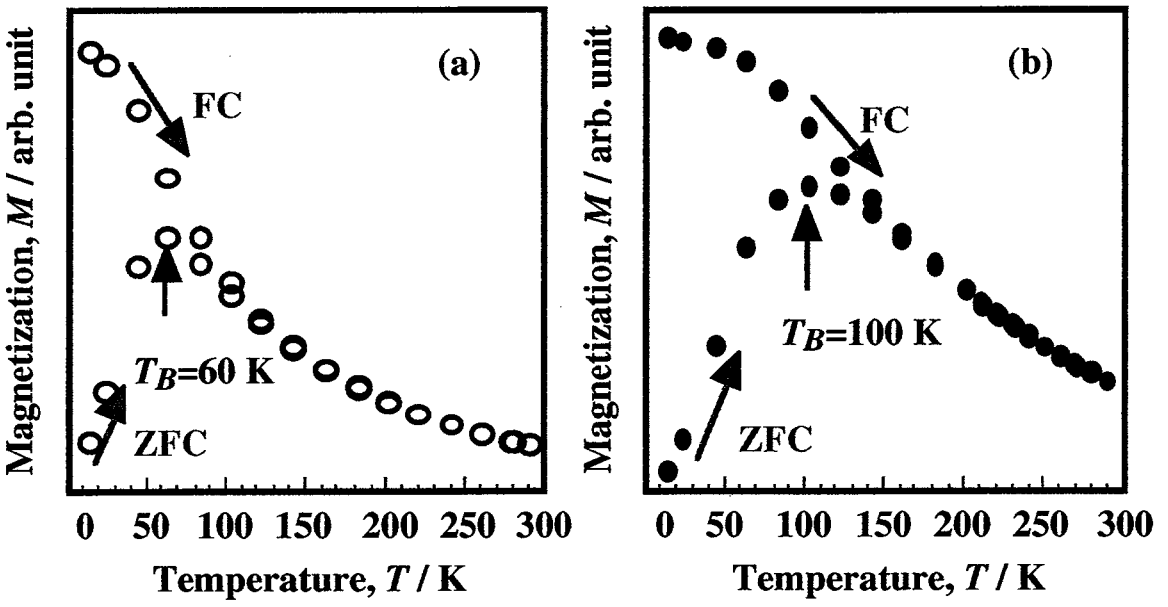

Fig. 2.9 DC magnetization versus temperature curves (FC and ZFC) for the after-calcined of (a) MgO/10 vol.% γ-Fe_2O_3 and (b) MgO/10 vol.% γ-Fe_2O_3 mixtures.

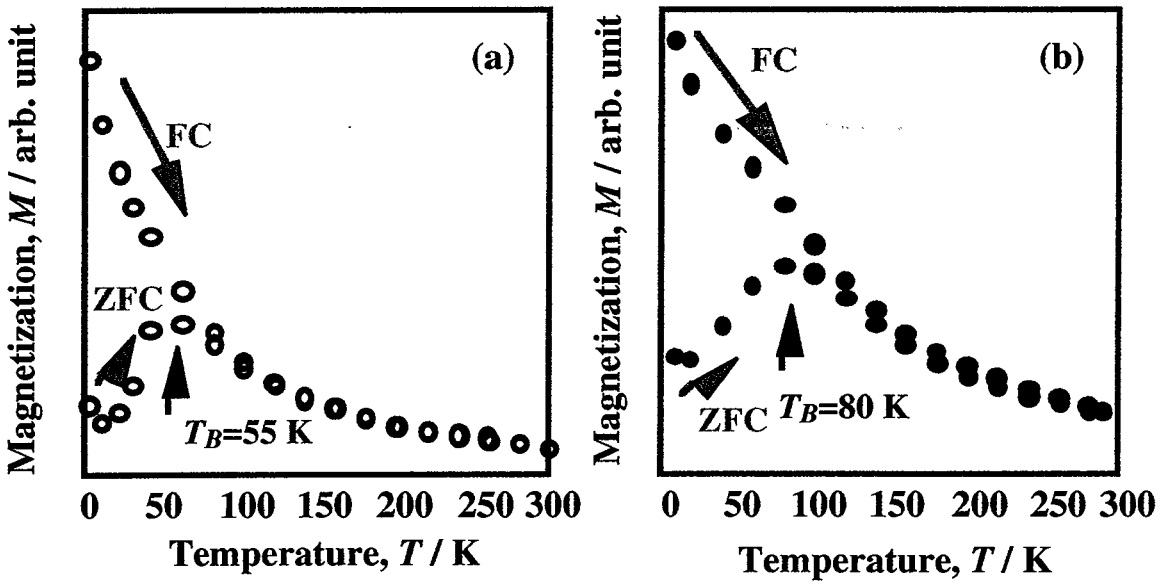

Fig. 2.10 DC magnetization versus temperature curves (FC and ZFC) for the mixtures after-calcined of (a) MgO/10 vol.% γ-Fe_2O_3 and CoO and (b) MgO/10 vol.% γ-Fe_2O_3 and CoO mixtures.

Figure 2.10 shows 30 Öe field cooled (FC) and zero-field cooled (ZFC) magnetization as a function of temperature measured in 30 Öe in the MgO/10 vol.% and 20 vol.% γ-Fe_2O_3 and CoO mixture. The mean superparamagnetic blocking temperature(T_B) of MgO/20 vol.% γ-Fe_2O_3 and CoO mixture (Fig. 2.10 (a)) is higher than that of MgO/10 vol.% γ-Fe_2O_3 and CoO mixture (Fig. 2.10 (b)). These results are in good agreement with TEM observations. And that, these blocking temperature (T_B) is rather lower than that of MgO/γ-Fe_2O_3 system. This fact is attributed to the exist of CoO. The magnetic property of both MgO and CoO is unti-ferromagnetic. These kind of material can be insulate the magnetic interaction of γ-Fe_2O_3.

For the MgO/10 vol.% Fe mixture, the hysteresis loop of the *M-H* curve was obtained by SQUID magnetometer measured at 300 K (Fig. 2.11), clearly showing the ferromagnetism of iron metal dispersed in the MgO matrix. The saturation magnetization (M_S) is estimated by Arrott plot [37]. M_S is found to be 192 emu/Fe gram (mixture), which is almost same value of coarse-grained standard Fe sample at room temperature, 217.2 emu/gram (see Table 2-II).

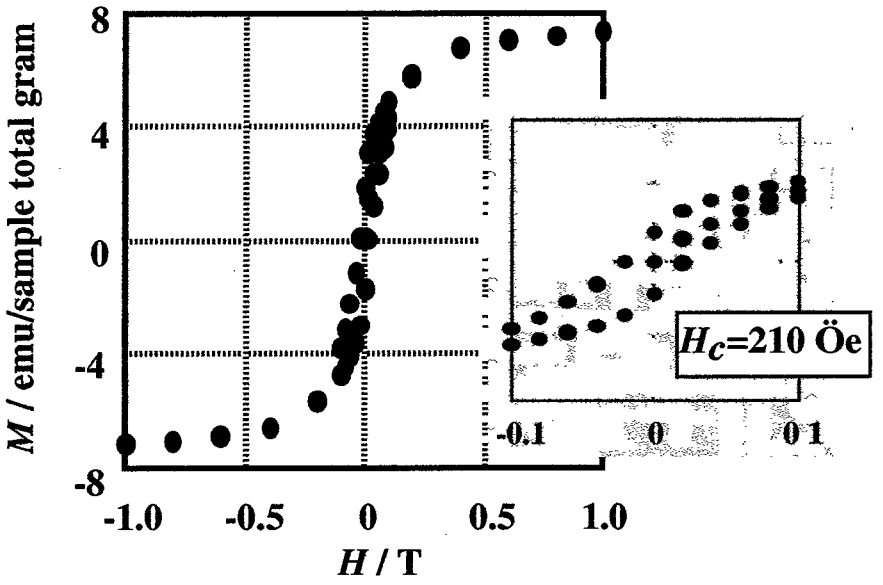

Fig. 2.11 Magnetization Curves for MgO/Fe 10 vol.% mixture. Inset shows enlargement of the plot near the origin.

Table 2-II Magnetic properties and average grain sizes of MgO/FeCo alloy mixtures.

Materials	Saturation magnetization $M_{s\,total}$ (emu/ total gram) ($M_{s\,FeCo}$) (emu/ alloy gram)	Coercive force H_C (Öe)	Average grain size $d_{av.}$ (nm)
MgO/5vol.% FeCo	20 (181)	225	47
MgO/10vol.% FeCo	39 (189)	215	63
MgO/20vol.% FeCo	76 (206)	87	270

Table 2-II shows the coercive force and average grain sizes of MgO/FeCo alloy mixtures. It has previously found in many materials that H_C varies as $1/d$ as single-domain size is approached. The maximum coercive force was 225 Öe for iron-cobalt alloy and this maxima occurred at an average particle size of 47 nm. *Luborsky* and *Paine* [38-39] reported that the coercive force at 76 K was about 700 Öe for iron-cobalt alloy at a diameter of 50 nm. It looks that the coercivity force is rather small value. In this study, the magnetic particles are isolated by MgO. We consider that

magnetic particles are sufficiently isolated from another. In case of this kinds of nano-sized magnetic particle, the coercivity force is assumed to be derived mainly from crystal anisotropy, shape anisotropy and internal stress anisotropy [37]. The iron-cobalt alloy the crystal anisotropy constant, K_1, becomes zero at 55 % iron at room temperature [38]. So, the coercive forces of iron-cobalt alloy mixtures is assumed to be derived mainly from shape anisotropy. However, the shape of iron-cobalt alloy mixtures were almost sphere as seen in Fig. 2.7. This is because the coercivity force of MgO/FeCo alloy mixture is rather small.

2.4. Conclusion

MgO based nanocluster and nanoparticle mixture with ferromagnetic particle dispersions were successfully fabricated by calcination and reduction process of MgO/Fe, Ni or Co nitrate mixtures prepared using a solution chemical route. This process was more easy and economical than another nanoprocess. The nanostructure of the mixtures was investigated using SEM and TEM and the magnetic properties of the mixtures were investigated using SQUID magnetometer. The obtained micrographs and magnetic properties revealed the following results:

(1) The particle size of the MgO and γ-Fe_2O_3 mixture after calcined at 673 K for 3 hr could be controlled by varying the iron (nickel, cobalt) content. These mixtures show the superparamagnetic behavior even at 100 K. And, the superparamagnetic blocking temperature of these mixtures were different and it corresponded to the nanocluster size.

(2) The typical microstructure of MgO/Fe mixture showed that the dispersed Fe particles are located both inside and outside of the MgO nanoparticle. This peculiar microstructure was due to migration and coalescence of metallic Fe particles during the reduction process. Furthermore, MgO/Fe composites showed the enhanced coercive force compared to pure Fe materials, and this is due to single domained iron nanoparticles.

References

[1] W. D. Kingery, H. K. Bowen and D. R. Uhlmann, "*Introduction to Ceramics*", John Wiley and Sons (1976) pp. 987-1015.

[2] K. Kusaka, N. Wada and A. Tasaki, *Jap. J. Appl. Phys.*, **8** (1969) 599.

[3] A. Tasaki, S. Tomiyama, S. Iida, N. Wada and R. Uyeda., *Jap. J. Appl. Phys.*, **4** (1965) 707.

[4] D.L. Leslie-Pelecky and R.D. Rieke, *Chem. Mater.*, **8** (1996) 1770.

[5] Q. A. Pankhurst and R.J. Pollard, *Condens. Mater.*, **5** (1993) 8487.

[6] T. Nakayama, Y.-H. Choa, T. A. Yamamoto and K. Niihara, *J. Jap. Soc.of Pow. and Pow. Metal.*, **42** (1998) 1207-1210.

[7] Y.-H. Choa, T. Nakayama, T. Sekino and K. Niihara, *Metals and Materials*, **5** (1999) 135-139.
[8] B.H. Shon, R.E. Cohen and G.C. Papaefthymiou, *J. Magn. Magn. Mat.*, **182** (1998) 216.
[9] J. L. Martin de Viedales, A. Lopez-Delgado, E. Vila and F.A. Lopez, *J. Alloys Compd.*, **287** (1999) 276.
[10] X. Li, G.X. Lu, H.L. He, T. Xu and K. Xu, *J. Alloys Compd.*, **235** (1996) 150.
[11] M. Sisk, J. Kilbride and A.J. Barkers, *J. Mat. Sci. Lett.*, **15** (1996) 1842.
[12] J. S. Helman and B. Ables, *Phys. Rev. Lett.*, **22** (1976) 1429.
[13] H. Fujimori, S. Mitani and S. Ohnuma, *Mater. Sci. Eng.*, **31** (1995) 219.
[14] T. Furubayashi and I. Nakatani, *Mat. Sci. Eng.*, **A21** (1996) 307.
[15] B. Bian and Y. Hirotsu, *Jpn. J. Appl. Phys.*, **36** (1997) L1232.
[16] B. Bian, Y. Hirotsu and A. Makino, *Nanostruct. Mat.*, 8 (1998) 1057.
[17] K. Sato, B. Bian, Y. Hirotsu and A. Makino, *J. Mag. Soc. Jpn.*, **23** (1999) 1177.
[18] T. J. Swoboda, P. Arther, Jr., N. L. Cox, J. N. Ingraham, A. L. Oppegard and M. S. Sadler, *J. Appl. Phys.*, **32** (1961) 374 S.
[19] J. R. Thomas, *J. Appl. Phys.*, **37** (1966) 2914.
[20] R. K. Melita, K. Yang and m. Misra, *J. Mater. Sci.*, **31** (1996) 1873.
[21] M. Pincda, J. L. Ficrro, J. M. Palacios, C. Cillcruclo and J. V. Ibarra., *J. Mater. Sci.*, **30** (1995) 6171.
[22] M. C. Woods, S. K. Gangwall, D. P. Harrison, K. Jothimurngesan, *Ind. Eng. Chem. Res.*, **30** (1991) 100.
[23] J. J. Liu, G.X. Lu, H.L. he, T. Xu and k. Xu, *Mater. Res. Bull.*, **31** (1996) 1049.
[24] Z. Solc. M. Trojan, D. Brandov and M. Kuchler, *J. Thermal. Anal.*, **33** (1988) 463.
[25] T. Sekino, T. Nakajima and k. Niihara, *Mat. Lett.*, **29** (1996) 165.
[26] K. Niihara and T. Sekino, *Mem. Inst. Sci. Ind. Res., Osaka Univ.*, **52** (1995) 57.
[27] T. Sekino, T. Nakajima, S. Ueda and K. Niihara, *J. Am. Ceram. Soc.*, **80** (1997) 1139.
[28] R.Z. Chen and W.H. Tuan, *Key Eng. mat.*, **161-163** (1999) 415.
[29] M. Awano, M. Sando and K. Niihara, "*Extended Abstracts of the Third International Symposium on Sinergy Ceramics*", 1999 Osaka, p.68.
[30] H. Kondo, T. Sekino, Y.-H. Choa and K. Niihara, *Key Eng. mat.*, **161-163** (1999) 419.
[31] Y.-H. Choa, H. Hayashi, T. Sekino and K. Niihara, *Key Eng. mat.*, **161-163** (1999) 493.
[32] Y.-H. Choa, T. Nakayama, T. Sekino and K. Niihara,*The Korean Journal of Ceramics* (in press).
[33] T. Sata, in "*Advances in Ceramics*", ed by W. D. Kingery, Am. Ceram. Soc., **10** (1985) 541.
[34] C. Papusoi, Jr., Al. Stancu, J.L. Dormann, *J. Magn. Magn. Mat.*, **174** (1997) 236.
[35] H. Kronmuller, R. Fischer, M. Bachmann and T. Leineweber, *J. Magn. Magn. Mat.*, **203** (1999) 12.
[36] F. Bodker, S. Morup, M.S. Pedersen, P. Svedlindh, G. T. Jonsson, J. L. Garcia-Palacios and F. J. Lazaro, *J. Magn. Magn. Mat.*, **177-181** (1998) 925.
[37] S. Chikazumi, "*Physics of Ferromagnetism-Magnetic Characteristics and Engineering Applications*; 1st ed. Syokabo, Tokyo, 1984.
[38] F. E. Luborsky, L. I. Mendelsohn and T. O. Paine, *J. Appl. Phys.*, **28** (1957) 344.
[39] F. E. Luborsky and T. O. Paine, *J. Appl. Phys.*, **31** (1960) 68S.

CHAPTER 3

Nano-sized Ferromagnet Dispersed MgO Nanocomposites for Magnetic Remote Sensing

3.1 Introduction

Recent investigations have led to the development of ceramic-metal nanocomposites such as Al_2O_3/Ni [1-5], Al_2O_3/Ni-Co [6, 7], ZrO2/Ni [8], MgO/Co and MgO/Ni [9, 10]. In this field, reinforcement models underline the interest of a homogeneous dispersion of nano-sized metal particles in a ceramic matrix. The microstructure of nanocomposite is schematically shown in Fig. 3.1 [11-13]. Mechanical properties such as fracture strength and toughness are expected to be simultaneously improved by the nanocomposites technology for MgO/metal system.

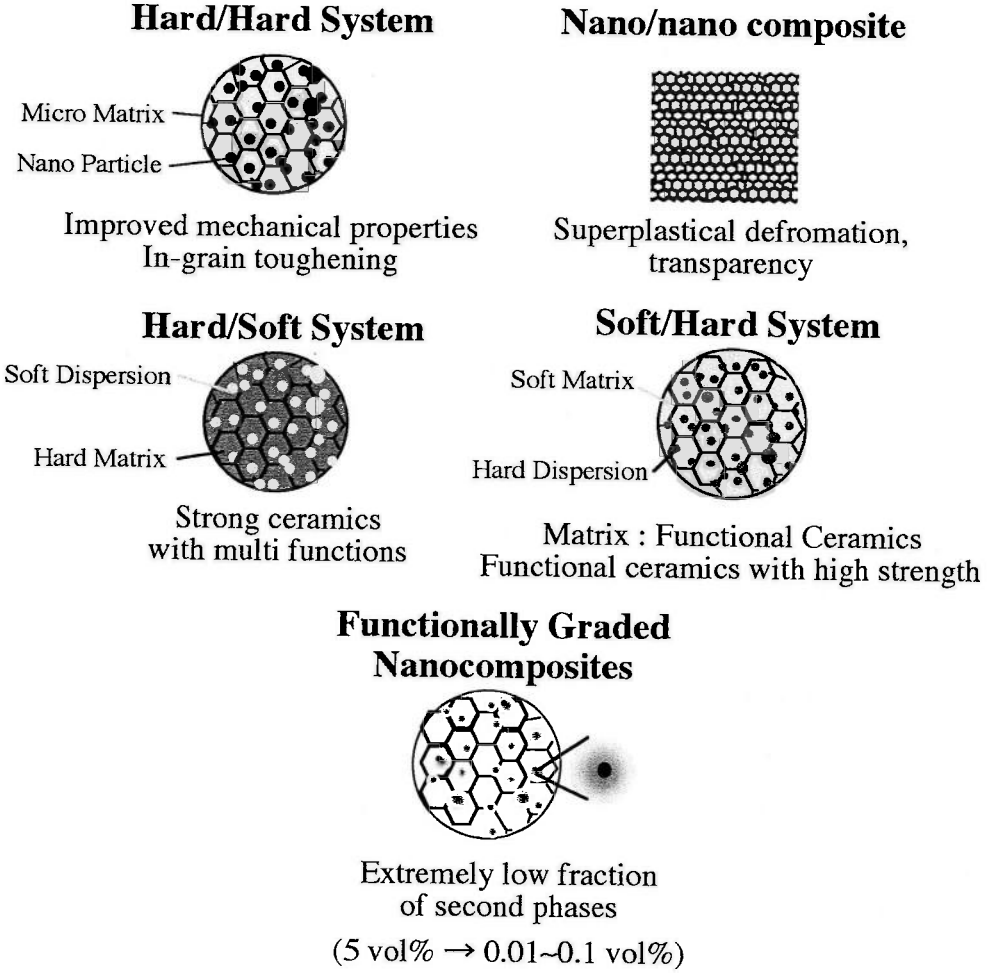

Fig. 3.1 The classification of ceramic nanocomposites [13].

In addition, the the studies of the ceramic/metal interface and the mechanical, magnetic and electrical properties represent other interesting subjects for futuer researches. With the recent progress in chemical processing, it is now possible to obtain desirable microstructures with homogeneous dispersions of nano-sized metal phases and which show unique physical properties [1-10].

However, in order to develop such a material, optimization of the powder preparation and sintering process and an understanding of the roles of the nano-sized dispersions are still required to solve. Recently, pulse electrical current sintering (PECS) method [14-20] is much interested in as a new process which is similar to hot-pressing (HP) because the pressure is applied during heating.

In the present study, we have selected the iron and its alloy (iron, 50 at% iron-50 at.% nickel and 50 at% iron-50 at.% cobalt) as the dispersant, because of this system show not only good mechanical properties but also high magnetic and magnetomechanical properties [21]. In this chapter, differences in the preparation process and in the resulting microstructural and mechanical characteristics will be described for the MgO/Fe, FeNi and FeCo systems. In addition, the magnetic remote sensing of applied stress by nanocomposite of ceramics matrix with ferromagnetic dispersoids will be discussed in this chapter.

3.2 Outline of Pulse Electrical Current Sintering Method

Pulse Electrical Current Sintering (PECS) is a newly developed process - a synthesis and processing technique - which makes possible sintering and sinter-bonding at low temperatures and in short periods by changing the intervals between powder supply with electrical energy and effectively by applying a high temperature spark generated momentarily. It is regarded as a rapid sintering method, using the self-heating action from inside the powder, similar to self-propagating high temperature synthesis (SHS) and microwave sintering. PECS systems offer many advantages over conventional systems such as hot press (HP) sintering, hot isostatic pressing (HIP) and atmospheric furnace sintering [14-19].

The PECS process features a very high thermal efficiency because of the direct heating of the sintering graphite mold and stacked powder materials by a large spark pulse current [14, 15]. It can easily consolidate a homogeneous, high-quality sintered compact because of the uniform heating, surface purification and activation made possible by dispersing the spark points. Figure 3.2 shows the basic configuration of typical PECS system. The system consists of a PECS machine with a vertical single-axis pressurization part, specially designed punch electrodes incorporating a water cooler, a water-cooled vacuum chamber, a vacuum/air/argon/nitrogen-gas atmosphere control

part, a special DC-pulse sintering power generator, a cooling water control part, a temperature measuring unit, an applied pressure display unit and various interlock safety units [15].

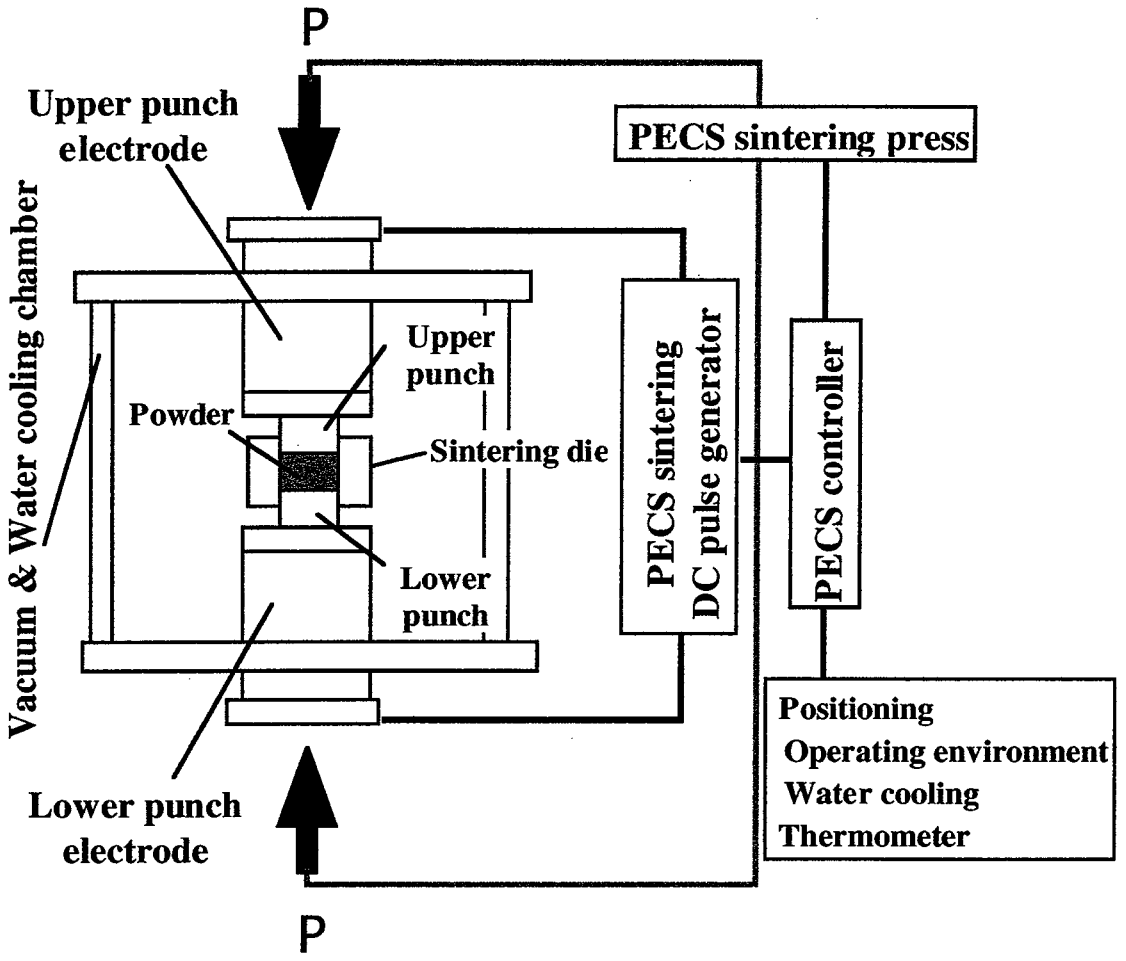

Fig. 3.2 The Pulse Electrical Current Sintering (PECS) system configuration [14].

The ON-OFF DC pulse energizing method generates: (1) spark impact pressure, (2) Joule heating and (3) an electrical field diffusion. In the PECS process, the powder particle surfaces are more easily purified and activated than in conventional electrical sintering processes and material transfers at both the micro and macro levels are promoted, so that a high-quality sintered compact is obtained at a lower temperature and in a shorter time than with conventional sintering processes [22-25].

Figure 3.3 illustrates how pulse current flows through powder particles inside the PECS sintering die [14].

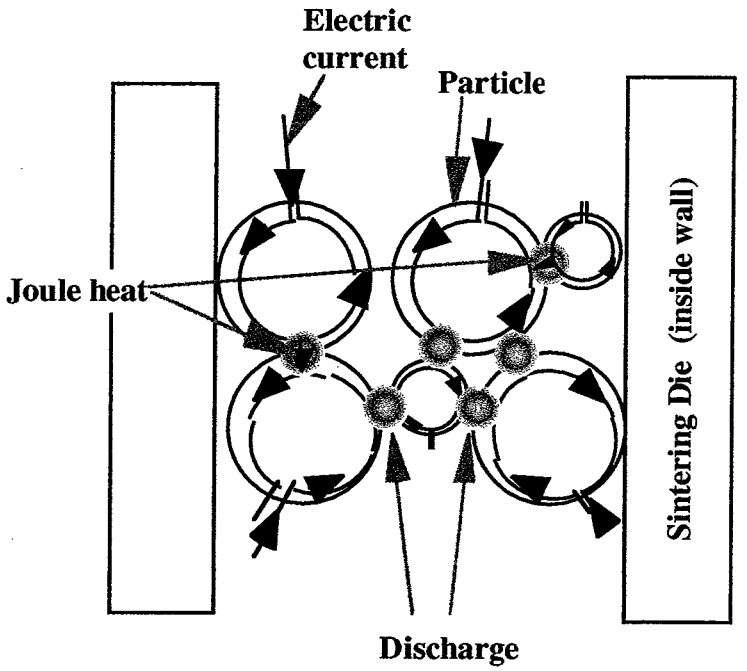

Fig. 3.3 Pulsed current flow through powder particles [14].

Conventional electrical hot press processes use DC or commercial AC power, and the main factors promoting sintering in these processes are the Joule heat generated by the power supply and the plastic flow of materials due to the application of pressure. The PECS process is an electrical sintering technique which applies an ON-OFF DC pulse voltage and current from a special pulse generator to a powder of particles, and in addition to the factors promoting sintering described above, also effectively discharges between particles of powder occurring at the initial stage of the pulse energizing is important for sintering. A spark impact pressure eliminates adsorptive gas and impurities existing on the surface of the powder particles. The action of the electrical field causes high-speed diffusion due to the high-speed migration of ions [14-19].

3.3 Experimental Procedures

3.3.1 Preparation of Materials

The solution chemistry route was selected to obtain the powder mixtures used for the composites. High-purity iron nitrate ($Fe(NO_3)_3 \cdot 9H_2O$, 99.9%), nickel nitrate ($Ni(NO_3)_2 \cdot 6H_2O$, 99.9%) and cobalt nitrate ($Co(NO_3)_2 \cdot 6H_2O$,99.9%) (Wako Pure Chemical Industries, Ltd., Japan) were used as source materials for Fe and alloy dispersions. Weighted nitrate corresponding to 0 to 40 vol% of Fe, $Fe_{0.5}Ni_{0.5}$ and $Fe_{0.5}Co_{0.5}$ alloy in final specimens was dissolved in alcohol.

Subsequently, MgO powder ($d_{av.}$=100 nm) (Ube Material Industries, Ltd., Japan) was mixed with above-mentioned solution and ball-milled for 24 hr. After dried, the mixtures were dry ball-milled for 12 hr and calcined at 673 K for 3 hr in air to obtain oxide (γ-Fe_2O_3, NiO and CoO) mixture powders. The obtained oxide powder mixtures were reduced to MgO/metal or alloy under hydrogen gas flow at 1373 K for 1 hr.

3.2.2 Pulse Electric Current Sintering

Pulse electric current sintering by using PECS (SPS 3.20 MK-IV; Sumitomo Coal Mining Co., Ltd.) with an applied uni-axial pressure of 100 MPa was made at 1473 K for 5 min under an argon gas atmosphere for reduced powder mixtures. The heating rate was fixed at 200 K/min for all sinterings (applied current; 3500 A, and applied voltage; 4 V). After the given time, the pressure was relaxed and the specimens were immediately cooled. The sintered specimens, 20 mmϕ in diameter, were polished with 9, 3 and 0.5 μm diamond pastes to posses mirror surfaces.

3.2.3 Evaluation

Relative density

Density of the specimen was measured by the Archimedes method using toluene or distilled water at room temperature. The relative density was determined by dividing the apparent density by the theoretical density which was calculated as the average of the raw materials.

Characterization

The phase composition of the powders was examined by X-ray diffraction (XRD) using Cu*ka* radiation (λ = 0.15418 nm) (Model DMS-2000 system, Scintag Co., U.S.A) even at high temperatures. The microstructure of the powders was observed by transmission electron microscopy (TEM) (Model H-8100, Hitachi Lid., Japan) and scanning electron microscopy (SEM) (Model S-5000, Hitachi Lid., Japan).

Mechanical Properties

The hardness (H_V) was evaluated by Vickers indentation under a condition of 98 N load with loading duration of 15 s in air. The fracture toughness (K_{IC}) at room temperature was determined simultaneously by the indentation fracture (IF) method[10] using an empirical equation for a median crack [26]. H_V [GPa] and K_{IC} values were calculated by Eqs. 3.1 and 3.2,

$$H_v = \frac{2P\sin(\alpha/2)}{d^2}, \tag{3.1}$$

$$K_{IC} = 0.203\left(\frac{c}{a}\right)^{-3/2} H_v a^{1/2}. \quad (3.2)$$

where P is the indentation pressure, α (=136°) is the angle comprised between the two opposite faces of the pyramidal indenter, d [μm] is the diagonal of the indentation measured by an optical microscope, c is the length of median crack and a is the half length of the diagonal impression.

Magnetic Property

The magnetization curve of the composites was measured using a SQUID magnetometer (Model, MPMS-5, QUANTUM DESIGN, U.S.A) with an applied magnetic field up to ±10 kÖe (= 1Tesla) at 300 K.

3.4 Results and Discussion

3.4.1 Phase Composition and Microstructure of the Composites

Relative densities of above 98 % were obtained with PECS at 1473 K at an applied pressure of 100 MPa. This temperature is 100-150 K lower than that by hot-pressing for obtaining dense MgO specimen [9, 10, 27-29]. The XRD patterns for the MgO/Fe nanocomposite prepared by sintering processes are shown in Fig. 3.4. Even after sintering, The XRD pattern contains the only MgO and metallic iron. This tendency was observed all other specimens, MgO/FeNi and FeCo alloy systems.

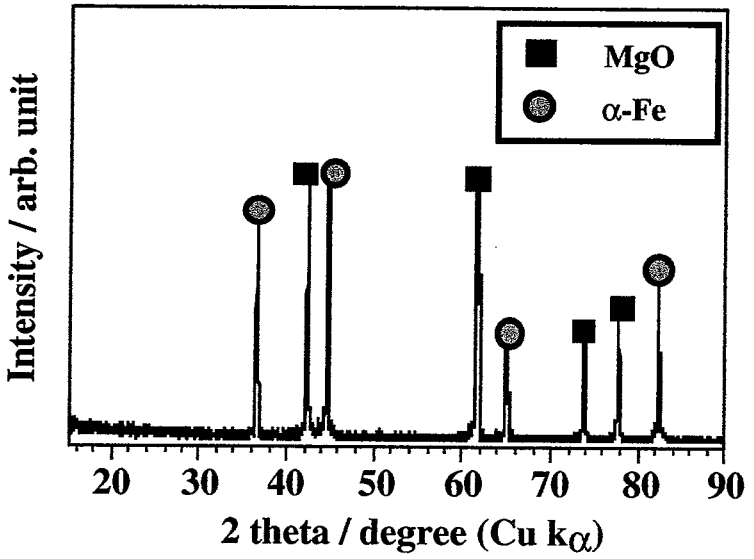

Fig. 3.4 XRD patterns for MgO/20 vol.% Fe composites.

Figure 3.5 shows the TEM micrograph of the MgO/20 vol% Fe composite. Densely sintered MgO/Fe nanocomposites show the bimodal distribution of the particle size of metallic Fe dispersions, that is, 10 to 50 nm for intragranular dispersions and 300-500 nm for intergranular dispersions at grain boundaries and triple junctions. The size of intergranular particle increased with increasing iron volume content. From these results, it is clearly understood that intergranular Fe particles were grown with increasing temperature during the sintering and volume fraction of Fe. This feature was due to migration and coalescence of metallic Fe particles, which the mobility of metallic Fe particles as a second phase in MgO/Fe system larger than that of MgO grain boundaries during the sintering (see Fig. 3.6). As a result, metallic Fe particles which located at MgO grain boundary or triple junction were migrated with the movement of MgO grain boundaries, and the coalescence of metallic Fe particles was occurred. After metallic Fe particles were coalesced, the drag force of Fe particles was enhanced for the movement of MgO grain boundary, as a result, the growth of MgO grain was inhibited.

MgO matrix grain size for MgO/20 vol% Fe composite sintered at 1473 K was approximately 1.3 μm and increased to be around 2.5 μm when the specimen was sintered at 1673 K. For MgO monolith, the grain size was about 4.2 μm when the specimen was sintered at 1673 K. It is, therefore, thought that the iron particulate dispersion can inhibit the matrix grain growth as likely to the SiC [30-32] and Ni [9, 10] dispersion in MgO.

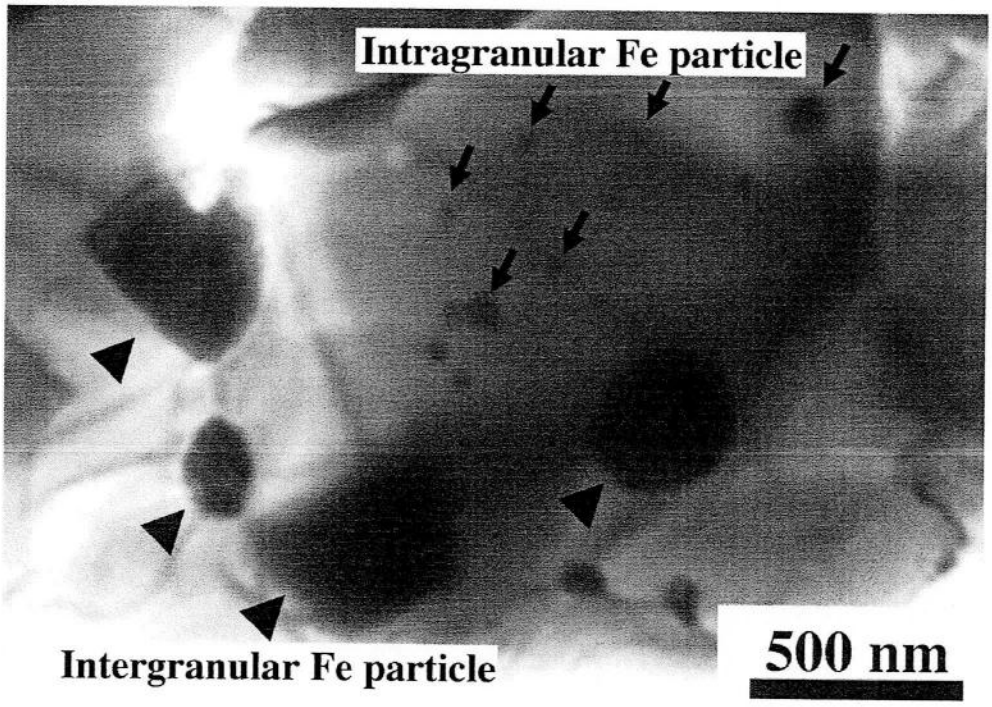

Fig. 3.5 The transmission electron microscopy micrograph of the MgO/20 vol% Fe composite.

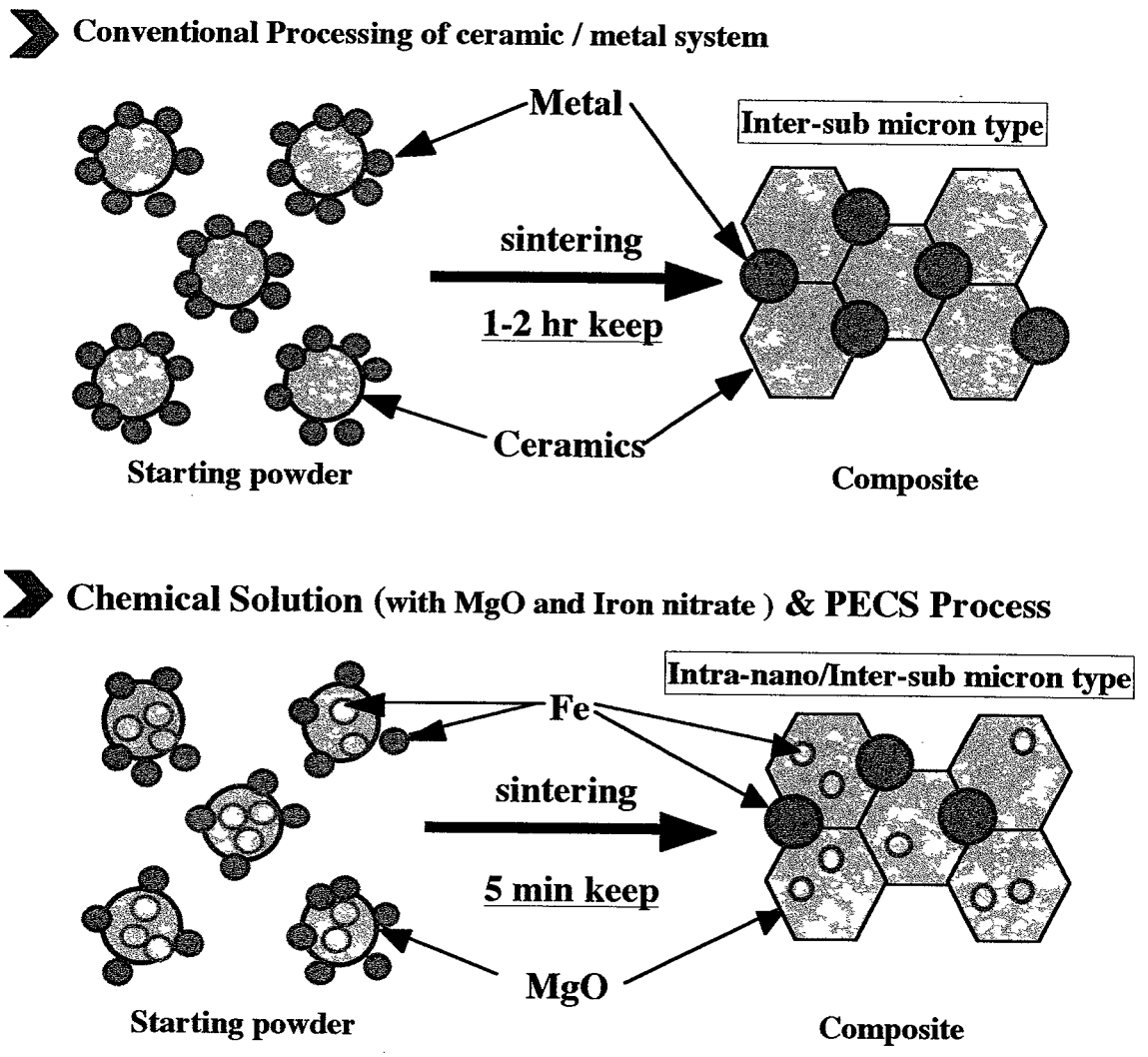

Fig. 3.6 Schematic drawings of the sintering mechanisms during the pulse electrical current sintering.

Figure 3.7 shows the TEM micrograph of the MgO/20 vol% FeNi composite. Almost same results were observed in this system. It shows the bimodal distribution of the particle size of metallic FeNi dispersions, that is, 20 to 80 nm for intragranular dispersions and 500-800 nm for intergranular dispersions. The defference of grain size is affected by lower melting temperature of FeNi alloy (ca. 100 K below Fe).

The high-resolution transmission electron microscopy (HREM) micrograph of the interface between the matrix and the intergranular large FeNi particles observed for the MgO/20 vol% FeNi composite is shown in Fig. 3.8. An intermediate phase, such as oxide or spinel, was not found in this image. This result suggests that the bonding between MgO and alloy dispersions is strong.

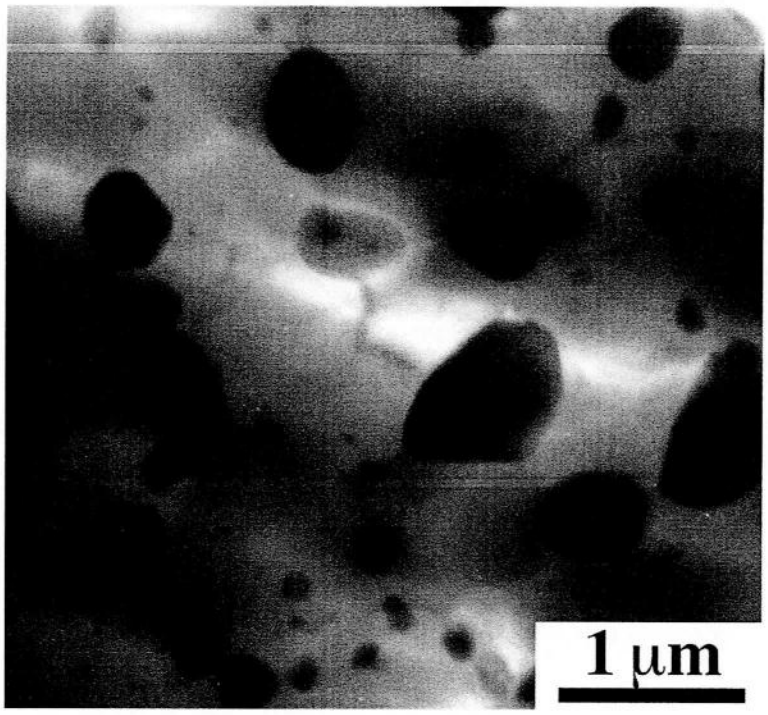

Fig. 3.7 The transmission electron microscopy micrograph of the MgO/20 vol% FeNi composite.

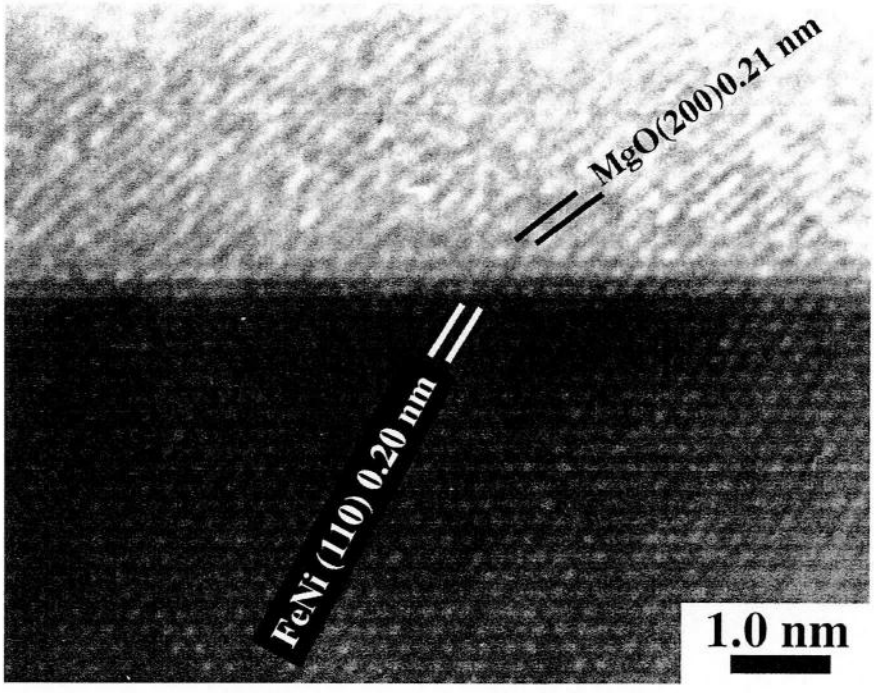

Fig. 3.8 The high-resolution transmission electron microscopy micrograph of the MgO/20 vol% FeNi composite.

3.4.2 Mechanical Properties

Figure 3.9 shows the effect of iron content on Vicker's hardness(H_V) and fracture toughness(K_{IC}) for MgO/Fe composites sintered at 1473 K. The Vicker's hardness decreased with increasing volume fraction of iron. On the other hand, the fracture toughness of 1.85 MPam$^{1/2}$ was achieved for the MgO containing only 10 vol% of iron, whereas highest toughness of 2.35 MPam$^{1/2}$ was obtained for MgO/40 vol.% Fe composites. The SEM image of the crack propagation in MgO/Fe 20vol% composite was shown in Fig. 3.10. It was found that the crack was partly deflected and partly bridging by intergranularly dispersed sub-miron sized iron particles. This result is in good agreement with HREM result that MgO and metal interface is strong.

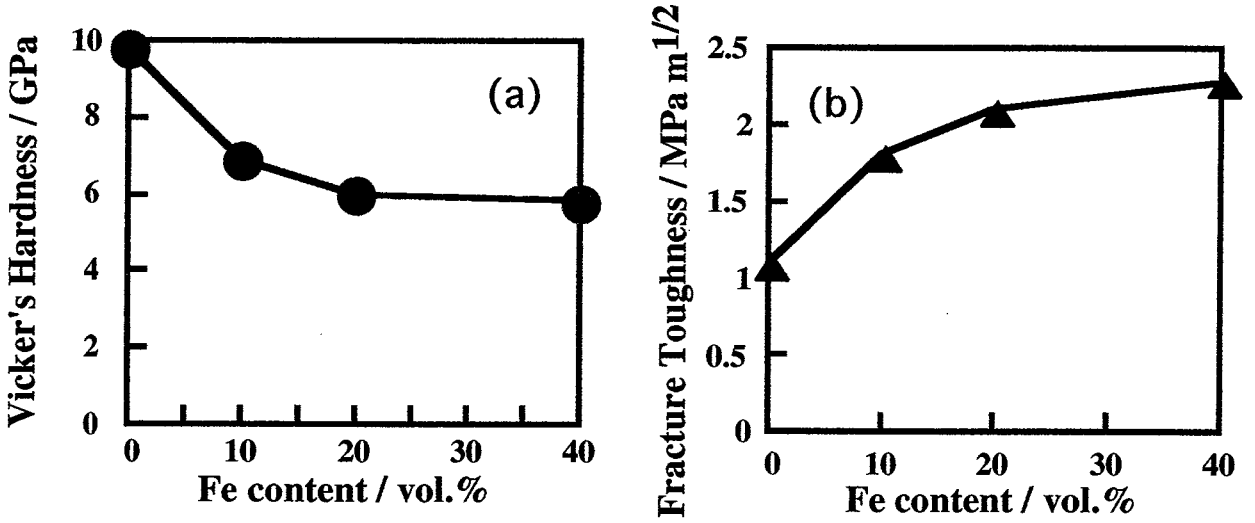

Fig. 3.9 Vicker's hardness(H_V) (a) and fracture toughness(K_{IC}) (b) for MgO/Fe composites sintered at 1473 K.

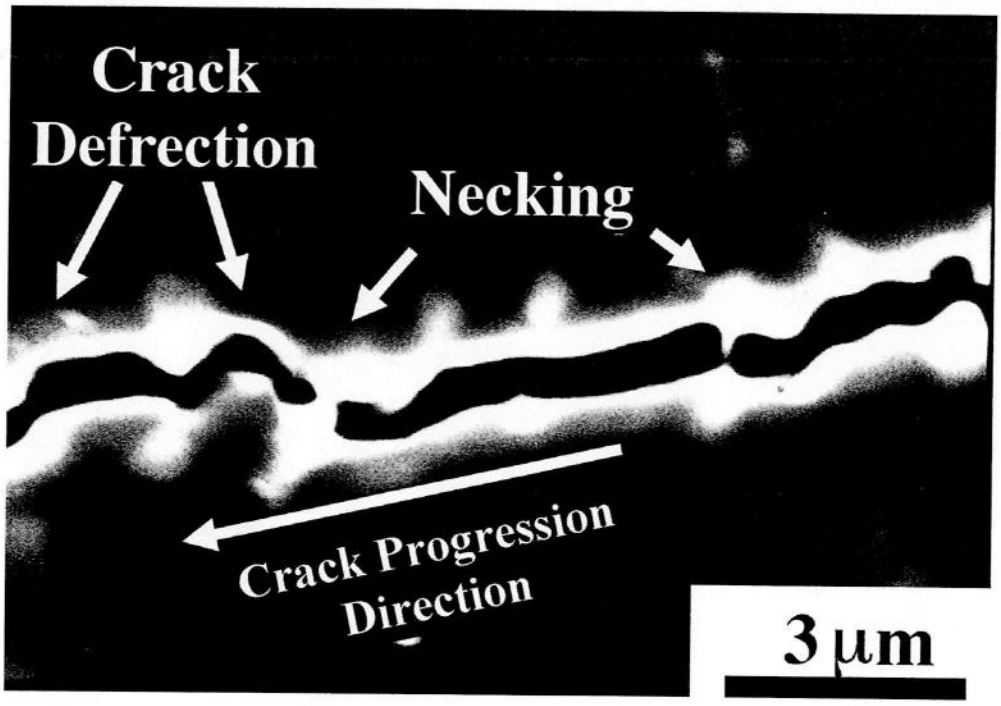

Fig. 3.10 The SEM image of the crack propagation in MgO/Fe 20vol% composite.

On the other hand, the SEM image of the crack propagation in MgO/Fe 40vol% composite was shown in Fig. 3.11. It was also found that the crack was partly deflected and partly bridging by intergranularly dispersed iron sub-miron sized particles. In this sample, iron coagulate of 1-5 μm was observed. In the metal/ceramic system, the main factors promoting PECS sintering are the Joule heat generated by the metal power and the plastic flow of metals due to the application of pressure, and then the excess metallic iron was preferentially agglomerated.

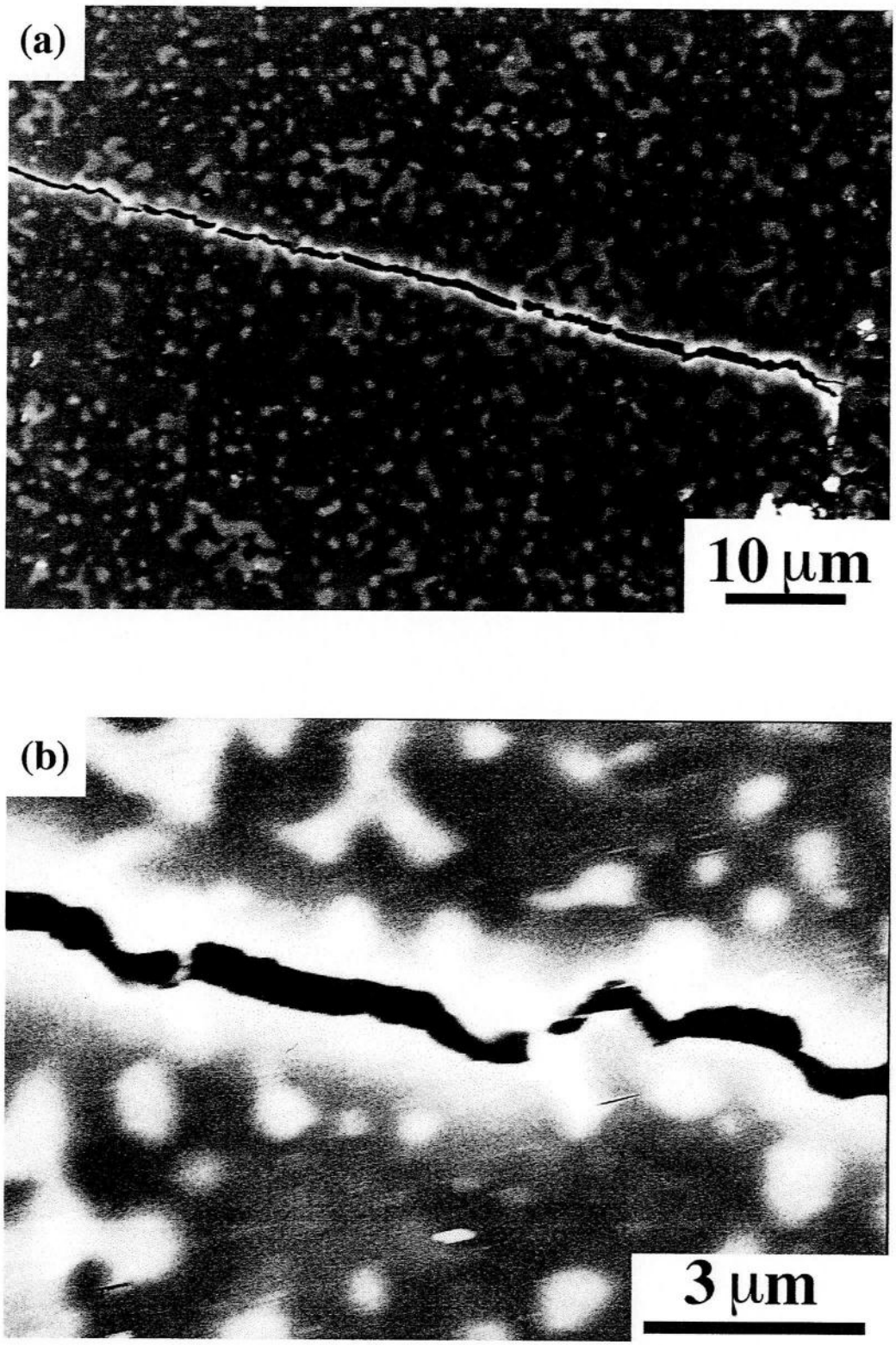

Fig. 3.11 The scanning electron microscopy image of the crack propagation in MgO/Fe 40 vol% composite, (a) low magnification and (b) high magnification.

For the MgO/20 vol.% Fe and 5 vol.% FeCo composite systems a hysteresis loop of the *I-H* curve (Fig. 3.12 and Fig. 3.13) was obtained by SQUID magnetometer measured at 300 K, clearly showing the ferromagnetism of iron dispersed in the MgO matrix. The coercive force (H_C) is 55 Öe(Fe) and 195 Öe(FeCo), which is approximately two orders of magnitude larger than that of pure iron metal (0.14-1.4 Öe (≈11-111 A/m)) [33]. H_C is well known to be strongly dependent on the grain size and dislocation density [33, 34]. When the particle size of a magnetic material decreased, its magnetic structure varies from a multi domain state to a single domain state, to reduce the total energy of the system; hence H_C is presented [34]. The extremely high value of H_C was reported for particle size in the range of several 10 nm, with corresponds to the magnetic single domain structure. In this composite, the size of intragranular iron particle is almost same of this range. It seems that the this type of iron dispersions might have a single domain structure.

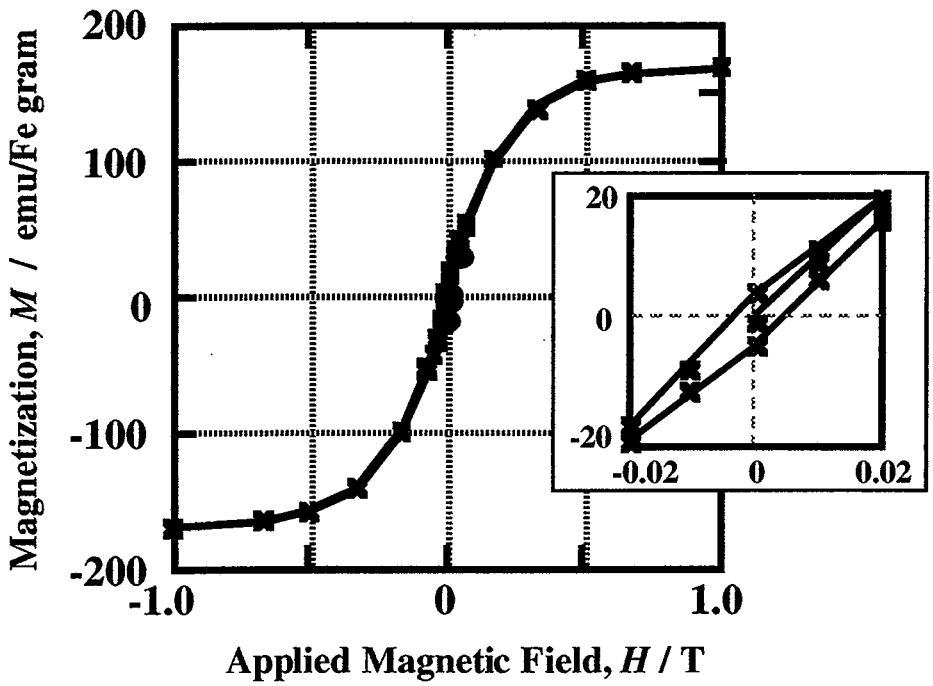

Fig. 3.12 Room temperature magnetization versus applied field curve for the MgO/20 vol.% Fe composite. Inset shows enlargement of the plot near the origin.

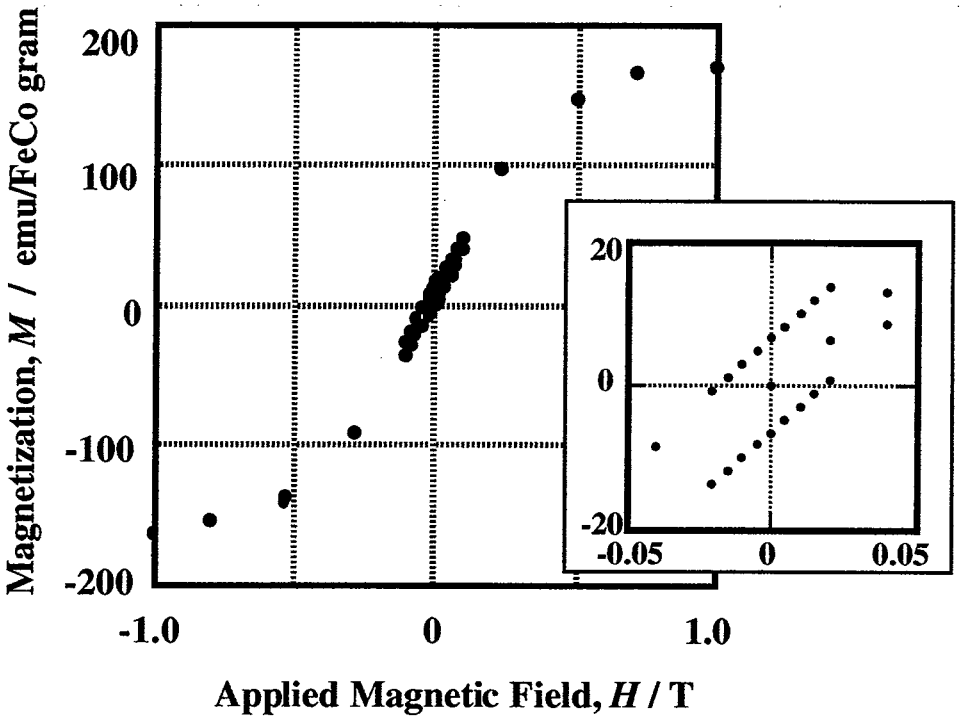

Fig. 3.13 Room temperature magnetization versus applied field curve for the MgO/5 vol.% FeCo alloy composite. Inset shows enlargement of the plot near the origin.

The saturation magnetization (M_S) of the MgO/20 vol.% Fe, FeNi and FeCo composite are estimated by Arrott plot (Table 3-I) [35]. These values are close value of reference data [35, 36] at room temperature (see Table II-1 in Chapter 2). This result also support the XRD and HREM results that no reaction phases are observed.

A relationship between applied stress and deviation of magnetization (permeability) in MgO/metal or alloy nanocomposites were measured by the DC susceptibility measurement under uni-axial compressional stress applied through alumina rod. DC susceptibility was measured in applied weak magnetic field (5 Öe) under applied stress varied from 0 to 300 MPa uni-axially. Figure 3.14 shows the relationship between magnetization change ($\Delta M/M_0$) in the applied stress of 0-300 MPa of the various phases.

Table 3-I Magnetic Properties and average grain sizes of MgO/Fe, Fe-Ni and FeCo composites.

Materials	Saturation magnetization M_S^{Metal} (emu/ metal gram)	Coercive force H_C (Öe)	Average grain size $d_{av.}$ (nm)
MgO/20vol.% Fe composite	188	55	400
MgO/20vol.% FeNi composite	137	27	420
MgO/5vol.% FeCo composite	167	195	220
MgO/10vol.% FeCo composite	183	98	390
MgO/20vol.% FeCo composite	205	90	430

It is evident that the magnetization change in all the composites increased as the applied stress increased in Fig. 3.14. Also, FeNi and FeCo alloys are considered to be effective in amplifying the magnetization sensitivity. Table 3-II shows the value of the magnetization change at the applied stress of 200 MPa and the saturated magnetostriction of standard bulk materials [35, 37]. These results suggest that the high volume magnetostriction factor contribute to the inverse magnetostrictive response of the MgO-based composites.

Figure 3.15 shows the relationship between magnetization change in the applied pressure of 0-200 MPa and the amount of FeCo dispersoids was varied from 5 to 20 vol.%. The tendency of increasing magnetization change with increasing dispersoid contents is shown in this figure. This is because the particle size of dispersoid of MgO/5 vol.% FeCo composite is smaller than that of 20 vol.% FeCo composite. Efficiency of actual stress introduced in each FeCo particles, as the result of coincident relationship between matrix and dispersoids, is a possible explanation of increasing response of magnetization change for decreasing size which make better fitting of grain boundaries [5-7].

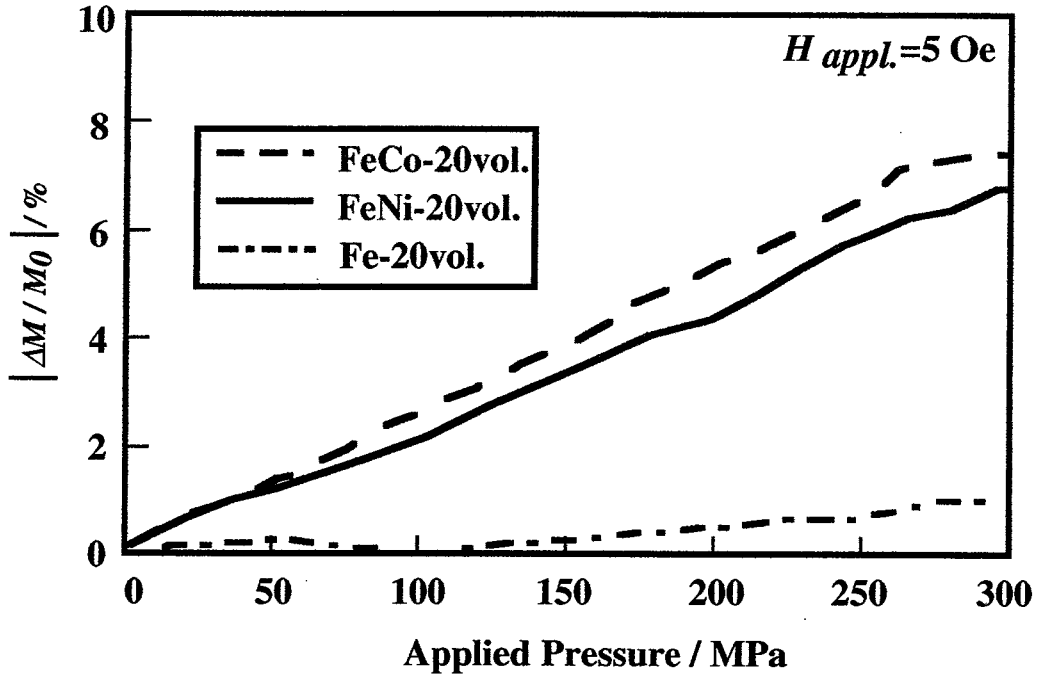

Fig. 3.14 The relationship between magnetization change ($\Delta M/M_0$) in the applied stress of 0-300 MPa.

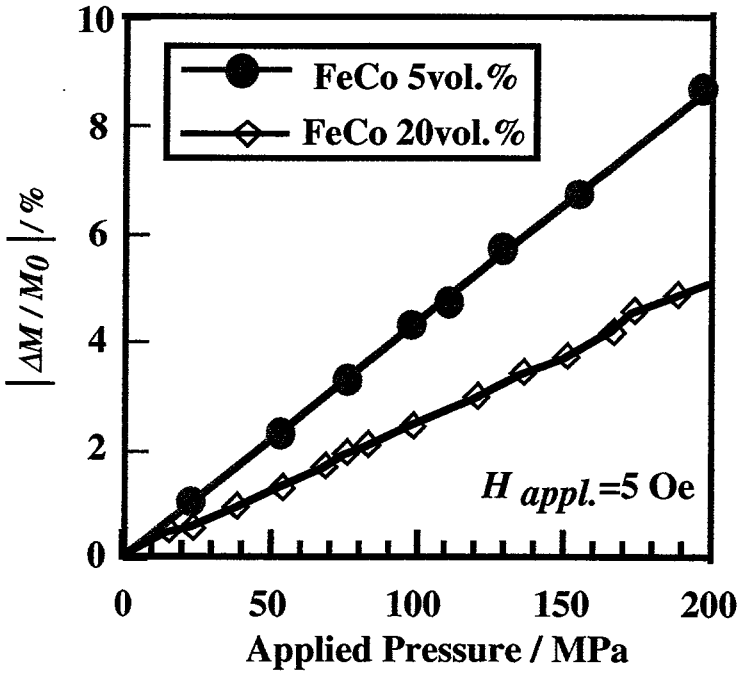

Fig. 3.15 The relationship between magnetization change ($\Delta M/M_0$) in the applied stress of 0-200 MPa.

Table 3-II The value of the magnetization change at the applied stress of 200 MPa and the saturated magnetostriction (λ_S) of standard samples.

	$\lvert\Delta M/M_0\rvert$(%)	λ_S (10^{-6})
MgO/ 20 vol.% Fe composite	0.1.5	-9
MgO/ 20 vol.% FeNi composite	4.1	28
MgO/ 20 vol.% FeCo composite	4.8	65

3. 5 Conclusions

MgO based composites with a homogeneous dispersion of nano-sized ferromagnetic dispersoids have been successfully fabricated by reducing and PECS of MgO/metal oxide composite powders prepared using a solution chemical route. These mixtures were easily obtained from the MgO and corresponding nitrate by calcination in air at a low temperature. The intergranularly dispersed ferromagnetic nano-particles inhibited grain growth of the MgO matrices. The fracture toughness increased with increasing volume fraction of iron. The increased toughness due to the plastic deformation of metal was confirmed for the composites containing large amount of metal dispersion. The ferromagnetism of nanometer-sized ferromagnetic particles to exhibit the high coercive force was contributed to the microstructure of ferromagnetic dispersions in MgO-based composites. Magnetization response to applied uni-axial stress in the nanocomposites was observed by the amplified magnetostriction effect of nanodispersoids. This magnetization change observed with the applied stress implies that the MgO/ferromagnetic metal nanocomposites have a strong possibility to use the stress/fracture sensing. Remote sensing of the applied stress on the structural ceramics combining with the fracture mechanics enhances reliability of ceramics by controlling the operating condition.

These results suggested that the method used in this study is found to be of great advantage to fabricate ceramic/metal nanocomposites possessing desirable microstructure for the multi functional composites.

References

[1] T. Sekino, T. Nakajima and K. Niihara, *Mat. Lett.*, **29** (1996) 165.

[2] K. Niihara and T. Sekino, *Mem. Inst. Sci. Ind. Res., Osaka Univ.*, **52** (1995) 57.

[3] T. Sekino, T. Nakajima, S. Ueda and K. Niihara, *J. Am. Ceram. Soc.*, **80** (1997) 1139.

[4] R.Z. Chen and W.H. Tuan, *Key Eng. mat.*, **161-163** (1999) 415.

[5] M. Awano, M. Sando and K. Niihara, "*Extended Abstracts of the Third International Symposium on Sinergy Ceramics*", 1999 Osaka, p.68.

[6] S.-T. Oh, M. Sando and K. Niihara, *Scripta Mat.*, **39** (1998) 1413.

[7] S.-T. Oh, T. Sekino and K. Niihara, *J. Eur. Ceram. Soc.*, **18** (1998) 31.

[8] H. Kondo, T. Sekino, Y.-H. Choa and K. Niihara, *Key Eng. mat.*, **161-163** (1999) 419.

[9] Y.-H. Choa, H. Hayashi, T. Sekino and K. Niihara, *Key Eng. mat.*, **161-163** (1999) 493.

[10] Y.-H. Choa, T. Nakayama, T. Sekino and K. Niihara,*The Korean Journal of Ceramics* (in press).

[11] K. Niihara, A. Nakahira, T. Sekino and Y.-H. Choa, *J. Jap. Soc.of Pow. and Pow. Metal.*, **44** (1997) 887.

[12] K. Niihara, *Mat. Integration*, **vol. 12** No.1 (1999) 1.

[13] K. Niihara, *New Ceramics*, **vol. 11** No.5 (1998) 1.

[14] M. Tokita, "*Proceedings of NEDO International Symposium on Functionally Graded materials*", Tokyo, Japan, 1999, p. 23.

[15] Y. Nakayama, "*Proceedings of NEDO International Symposium on Functionally Graded materials*", Tokyo, Japan, 1999, p. 35.

[16] M. Tokita, *J. Soc. Pow. Tec. Jpn.*, **30** (1993) 790.

[17] M. ishiyama; "*Proceedings of 1993 Powder Metall. World Congress.*" Ed. by Y. Mando and K. kosuge, Kyoto, Japan (1993) 931.

[18] M. Tokita, *J. Soc. Powder. Tech. Jpn.*, **30** (1993) 790.

[19] N. Murayama, *Ceramics, J. Ceram. Soc. Jpn.*, **32** (1997) 445.

[20] I. Kondoh, T. Tanaka and N. Tamai, *J. Ceram. Soc. Jpn.*, **102** (1994) 505.

[21] T. Nakayama, Y.-H. Choa, T. Sekino and K. Niihara, *J. Ceram. Soc. Jpn.* (in contribution).

[22] M. Omori and T. Hirai, *New Ceramics Japan*, **7** (1994) 4.

[23] L. Gao, H.Z. Wang, J.S. Hong, H. Miyamoto, K. Miyamoto, S.D. De la Torre and Y. Nishikawa, *Key Eng. mat.*, **161-163** (1999) 401.

[24] M. Omori, A. Okubo, G.H. Kang and T. Hirai; "*Functionally Graded Materials 1996*", Ed. by I. Shiota and Y. Miyamoto, Tsukuba, Japan (1997) 767.

[25] M. Omori, A. Okubo, K. Gilhan and T. Hirai, *J. Mater. Syuth. Proc.*, **5** (1997) 279.

[26] K. Niihara, R. Morena and D.P.H. hasselman, *J. mater. Sci. Lett.*, **1** (1982) 13.

[27] A.G. Evans and R.W. Davidge, *Phill. Mag.*, **20** (1969) 373.

[28] K. Yasuda, S.D. Kim, Y. Kanemichi, Y. Matsuo and S. kimura, *J. Ceram. Soc. Jpn.*, **98** (1990) 1103.

[29] Y.-H. Choa, T. Kusunose, A. Nakahira and K. Niihara, "*Proceedings of 4th International SAMPE Symposium*" (1995) 400.

[30] Y.-H. Choa, A. Nakahira, T. Sekino and K. Niihara, *J. Korean Pow. met. Inst.*, **4** (1997) 151.

[31] Y.-H. Choa, Y.-K. Jeong, T. Kusunose, T. Sekino and K. Niihara, "*Proceedings of the 14th International Japan-Korea Ceramic Seminar on Ceramics*" (1997) 166.
[32] Y.-H. Choa, H. Kawaoka, T. Sekino and K. Niihara, *Key Eng. Mat.*, **132-136** (1997) 2009.
[33] F.E. Luborsky, L.I. Mendelsohn and T.O. Paine, *J. Appl. Phys.*, **28** (1957) 344.
[34] F.E. Luborsky and T.O. Paine, *J. Appl. Phys.*, **31** (1960) 68S.
[35] S. Chikazumi, "*Physics of Ferromagnetism-Magnetic Characteristics and Engineering Applications*; 2nd ed. Syokabo, Tokyo, 1984.
[36] W.D. Kingery, H.K. Bowen and D. R. Uhlmann, "*Introduction to Ceramics*", John Wiley and Sons (1976) pp. 987-1015.
[37] Y. Masiyama, *Sci. Rep Tohoku Univ.* **20** (1931) 574.

CHAPTER 4

Structure and Magnetic Properties of Iron Oxide Disperesed Silver Based Nanocluster Composite

4.1 Introduction

4.1.1 Nanoclustered Composite

Nanostructured magnetic materials exhibit novel enhanced properties that derive from the nanoscale dimensions of the magnetic constituents, abundance of interfaces, and degrees of magnetic communication, controlled by the extent of dispersion of nanostructures within non-magnetic supporting matrices [1-8]. Due to the large surface-to-volume ratio (Table 4-I) the magnetic properties are dominated by surface effects and particle-support interactions. They exhibit magnetic anisotropy constants two orders of magnitude larger than their bulk counterparts and correspondingly enhanced coercivities [9].

Table 4-I Surface to volume ratio of various size particles.

Number of surface atom	8	98	488	58800	6×10^6
Number of total atom	8	125	1000	1×10^6	1×10^9
Ratio of surface atom (%)	100	78.4	48.8	5.9	0.6
Particle diameter			ca. 1.5 nm **nanocluster**	ca.15 nm **nanoparticle**	ca.150 nm **sub-micron particle**

The support or matrix, within which nanostructures are synthesized, plays an active role in determing their physical properties in addition to providing a means of particle dispersion [10, 11]. The macroscopic magnetic properties of nanocomposites reflect the combined action of quantum-size effects [12-15], strain and surface effects [16-20], interfaces between nanostructures and the matrix [21], matrix properties, and morphologies of nanostructures. These parameters, or degrees of freedom, can be strategically controlled for the design of artificially structured materials with

tailored properties.

An extensive previous researches on iron, iron-oxide and ferrite nanostructures and their nanocomposites [1, 22] attests to the vast technological importance of these materials for broad application in the nanotechnologies of information storage [23], color imaging [24], bioprocessing [25, 26], magnetic resonance imaging enhancement [27, 28], giant magnetoresistance devices [29-34], advanced working substances for magnetic refrigeration [35-40], and quantum size effects [12-15]. Thus, the design and synthesis of magnetic nanostructures with controlled size and uniform dispersion is an important subject of current materials research [41].

In this chapter, a binary iron-silver system has been chosen for the reason that a complete phase separation (see Fig. 4.1). The solubility of silver in solid iron reaches a maximum of approximately 0.022 at.% at 1398 °C in the γ phase [42]. Furthermore, silver is the the non-magnetic insulator for magnetic iron or iron oxide nanoclusters and its thermal conductivity is quite large (0.999 cal sec^{-1} cm^{-2} $°C^{-1}$ cm^{-1}, at 0 °C) [43], and then his is the fitly for the working substances for magnetic refrigeration. The nanocluster composites of the magnetic iron or iron oxide with the grain sizes in the range from 1 to 10 nm and nano sized silver matrix were synthesized by Inert Gas Condensation (IGC) method combined with post annealing treatment. Inert gas condensation processing was chosen for its flexibility in modification of synthesis parameters. And, the post annealing treatment has a possibility to modify the phase transformation, morphology and magnetic properties of iron or iron oxide.

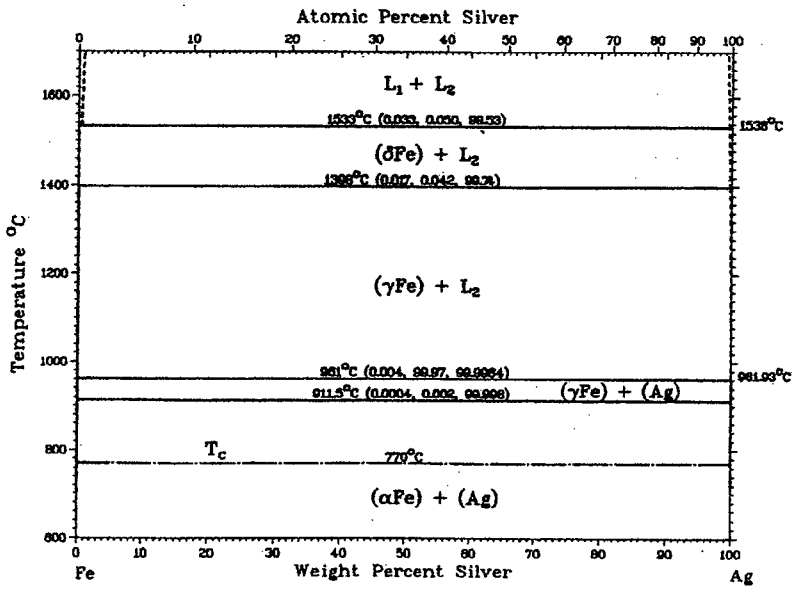

Fig. 4.1 Phase diagrams of Ag-Fe system [44].

The Fe-O system has four equilibrium compounds (see, Fig. 4.2), ferromagnetic Fe_3O_4 and γ-Fe_2O_3, and antiferromagnetic α-Fe_2O_3 and FeO, which provides not only versatility in synthesizing magnetic nanocluster composites but also problems in characterizing materials containing them [45]. To identify the iron-containing phase responsible for the magnetism of our nanocluster composite, it is necessary to overcome both the grains embedded in the heavy silver matrix.

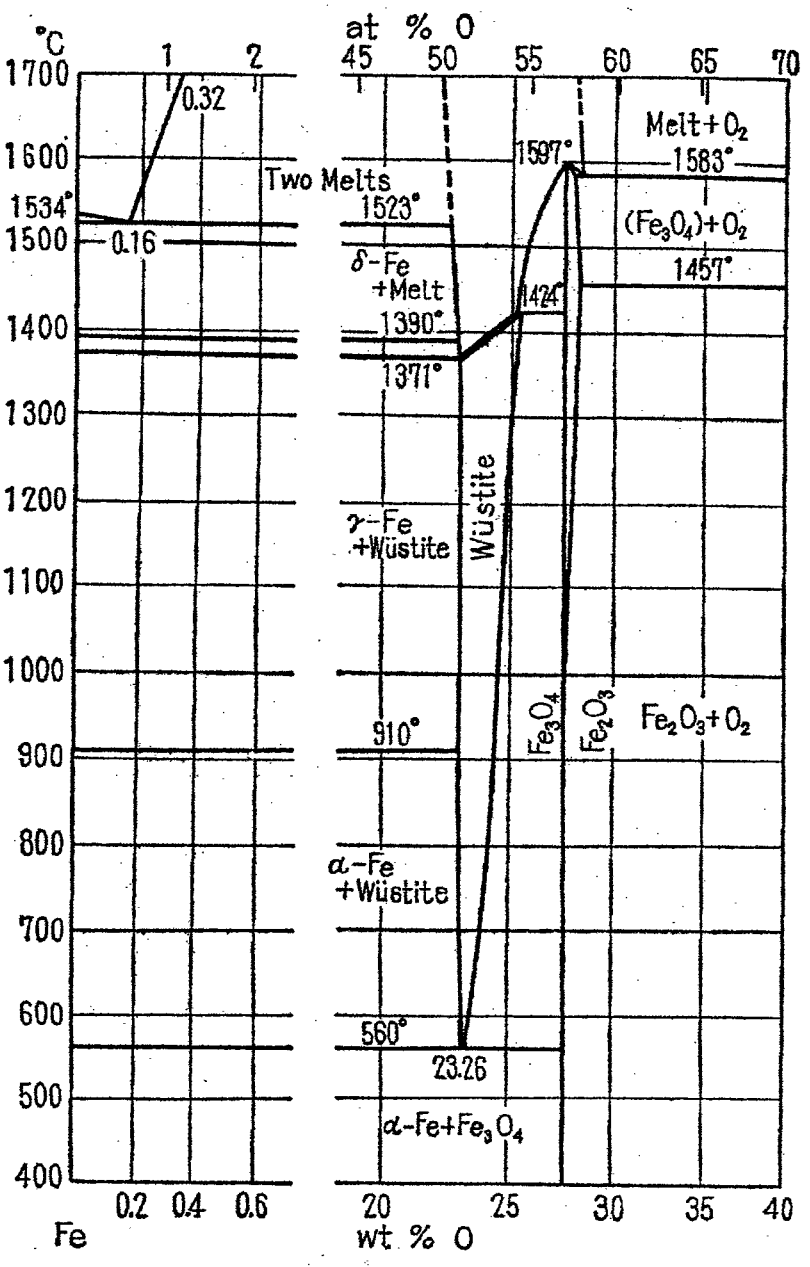

Fig. 4.2 Phase diagrams of Fe-O system [45].

4.1.2 XANES Measurement

When X-rays pass through any sort of material, a proportion of them will be absorbed. Measuring the amount of absorption with increasing X-ray energy reveals so-called edge structures, where the level of absorption suddenly increases [46-48]. This happens when X-ray has sufficient energy to free or excite a bound electron within the material. Usually, small oscillations can be seen superimposed on the edge step. These gradually die away as the X-ray energy increases. The oscillations, which occur relatively close to the edge (within about 40 eV) are known as NEXAFS (Near Edge X-ray Absorption Fine Structure) or XANES (X-ray Absorption Near Edge Structure) [46, 47]. Analysis of these XANES oscillations in the spectrum of a particular sample can provide information about vacant orbitals, electronic configuration and site symmetry of the absorbing atom. Theoretical multiple scattering calculations can be compared with the experimental spectrum to determine the geometrical arrangement of the atoms surrounding the absorbing atom. The absolute position of the edge also contains information about the oxidation state of the absorbing atom [48].

4.2 Experimental Procedure

4.1.1 Sample Preparation

Iron oxide dispersed metallic silver based nanocluster composites were synthesized by the IGC method combined with a co-evaporation process [36-40]. Evaporation chamber used in the present work is shown in Fig. 4.3. Metallic iron and silver were used as source materials, and these metals were evaporated by resistance heated boats in a chamber filled with helium gas. Table 4. II shows the evaporation technical data for silver/iron system. Because of reactivity to Ta and Mo, the material of heating boat was selected to tungsten. The particle size of the metallic iron and silver mixture was controlled by the inert helium gas pressure of 1 to 10 Torr. The helium gas quenches the metallic vapor, and nanoparticles are formed above the boats and transported to the surface of a particle collector cooled by liquid nitrogen. The collector is cylindrical and rotates during the evaporation process to obtain a homogeneous mixture of the two phases. After evaporation, only the iron particles are stabilized by oxygen gas exposure up to 1.0 Torr. Subsequently, the silver and iron oxide powder mixture is scraped off the collector surface and transported *in situ* to a chamber for compaction. The compaction condition is 400 MPa at room temperature. From these samples, one was post-annealed in an oxidizing atmosphere of 10%-O_2 / Ar at 473 K for 1 h to investigate the oxidation effect on the phase transformation of iron and iron oxide.

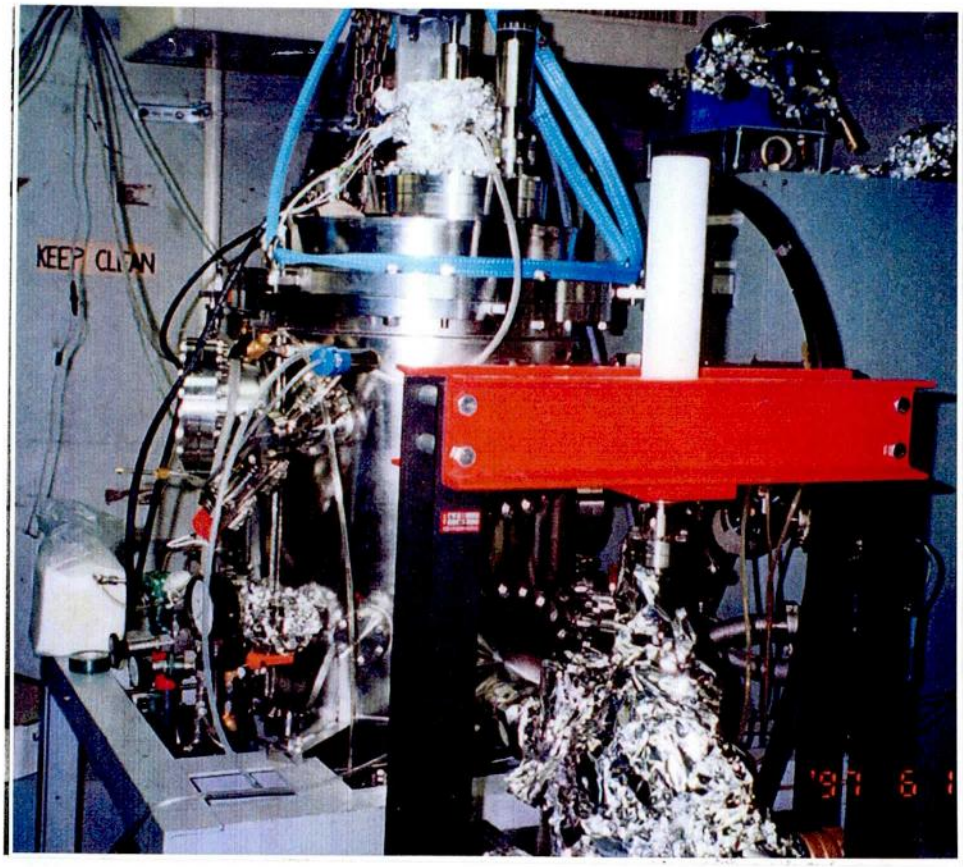

Fig. 4.3 Image of IGC chamber to synthesize the nanocluster composites.

Table 4-II Evaporation technical data

Substance	Melting point [°C]	Boiling point [°C]	Temperature [°C] at vapor pressure [mbar]		Evaporation source ● =good, ○ =possible			
			10^{-2}	10^{-1}	W	Mo	Ta	Al_2O_3
Fe	1536	3070	1430	1580	●	○	—	—
Fe_2O_3	1594	—	~1200	—	○	○	—	—
Ag	961	2212	1020	1150	●	●	—	●

4.2.2 Evaluation

The microstructure of the nanocluster composites was studied by SEM and TEM. The iron concentration in the material was determined by SEM-EDS and TEM-EDS. To obtain reference data, all measurements were done on commercially available pure Fe, FeO, Fe_3O_4, γ-Fe_2O_3 and α-Fe_2O_3 as well.

4.2.3 Measurements of XANES Spectra

X-ray near edge absorption spectroscopy (XANES) (KEK (High Energy Accelerator Research Organization)-Photon Factory, BL-7C and BL-12C) [49, 50] measurements were performed on the silver/iron or iron oxide nanocluster composites using specimens prepared by mounting on tape powder obtained from grinding the nanocluster composite pellet. As is conventional, the background subtracted absorption coefficient, m, has been normalized to the absorption step at the edge. To emphasize the energy shifts and feature changes in the near edge region, the derivative spectra $\partial\mu/\partial E$ are plotted versus the photon energy E. Figure 4.4 shows the schematic drawing of Beam Line of BL-12C.

XANES absorption spectra at the Fe-K edge of samples are measured at the BL-7C and BL-12C (KEK-PF) [49, 50]. A iron foil is used to calibrate the energy of the absorption edge. Powder samples mounted between polypropylene films were set between two ionization chambers filled with N_2 gas. The double crystal Si (111) monochromator was scanned in 2 arc sec steps across the K-edge within the theta range. This arrangement takes advantage of the strong polarization of the synchrotron radiation in the orbital plane. A computer is used to control stepping motors that drive monochromator crystals. Detectors will produce two intensity at same energy. The voltages from the ion chambers are converted to frequencies at each monochromator step and counted. These values are the intensity of the incident (or reference) beam (I_0) and that of the transmitted beam (I). These I_0 and I values are stored on the computer disk, along with the monochromator and table positrons.

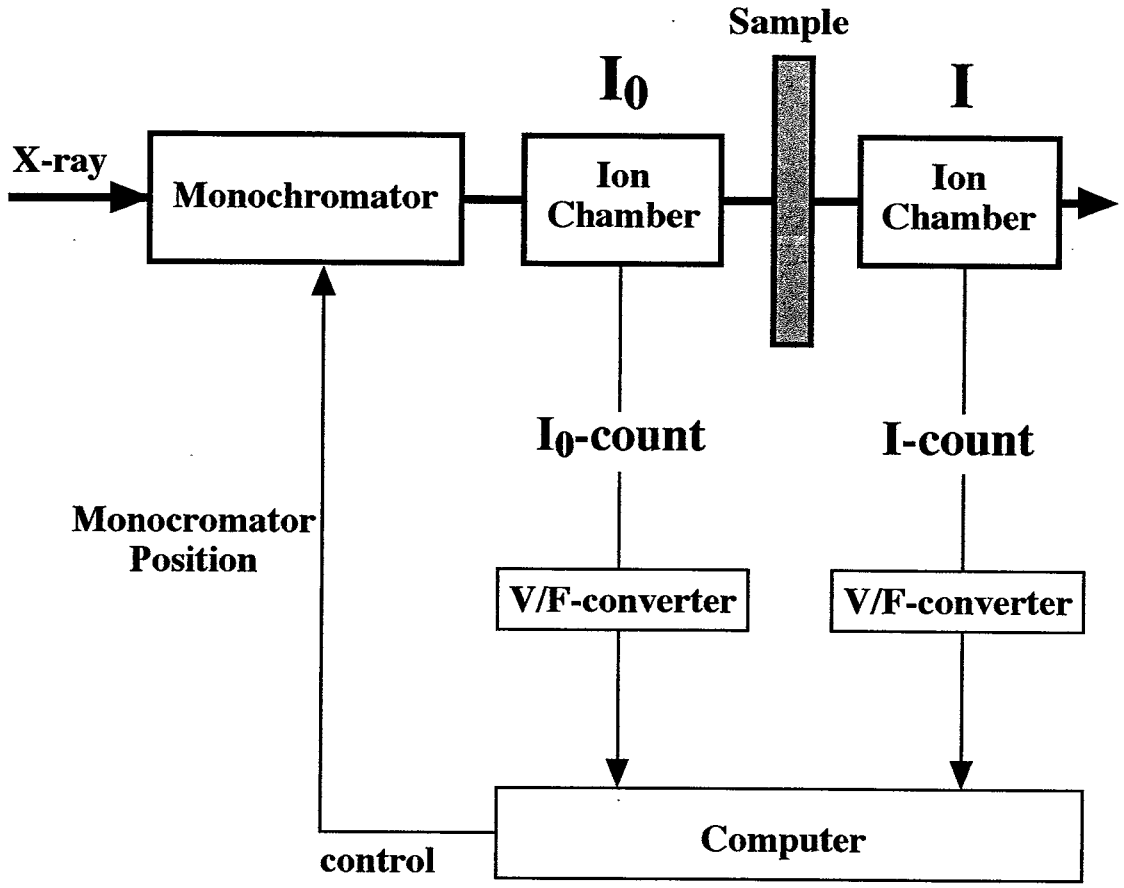

Fig.4.4 Schematic drawing of Beam Line of BL-12C (KEK-PL).

4.3 Results and Discussion

4.3.1 Microstructure

The particle size of the composite mixture is controlled by the inert helium gas pressure from 1 to 10 Torr, and increased with an increase of helium gas pressure for the loose nanocluster composite powder. Figure 4.5 (a-d) shows SEM micrographs of the as-compacted silver/iron or iron oxide nanocluster composites obtained at helium gas pressures of 0.1, 1.0, 5 and 10 Torr, respectively. The average grain size of the nanocomposites was estimated to be 15, 12, 20 and 26 nm, respectively, from the micrographs.

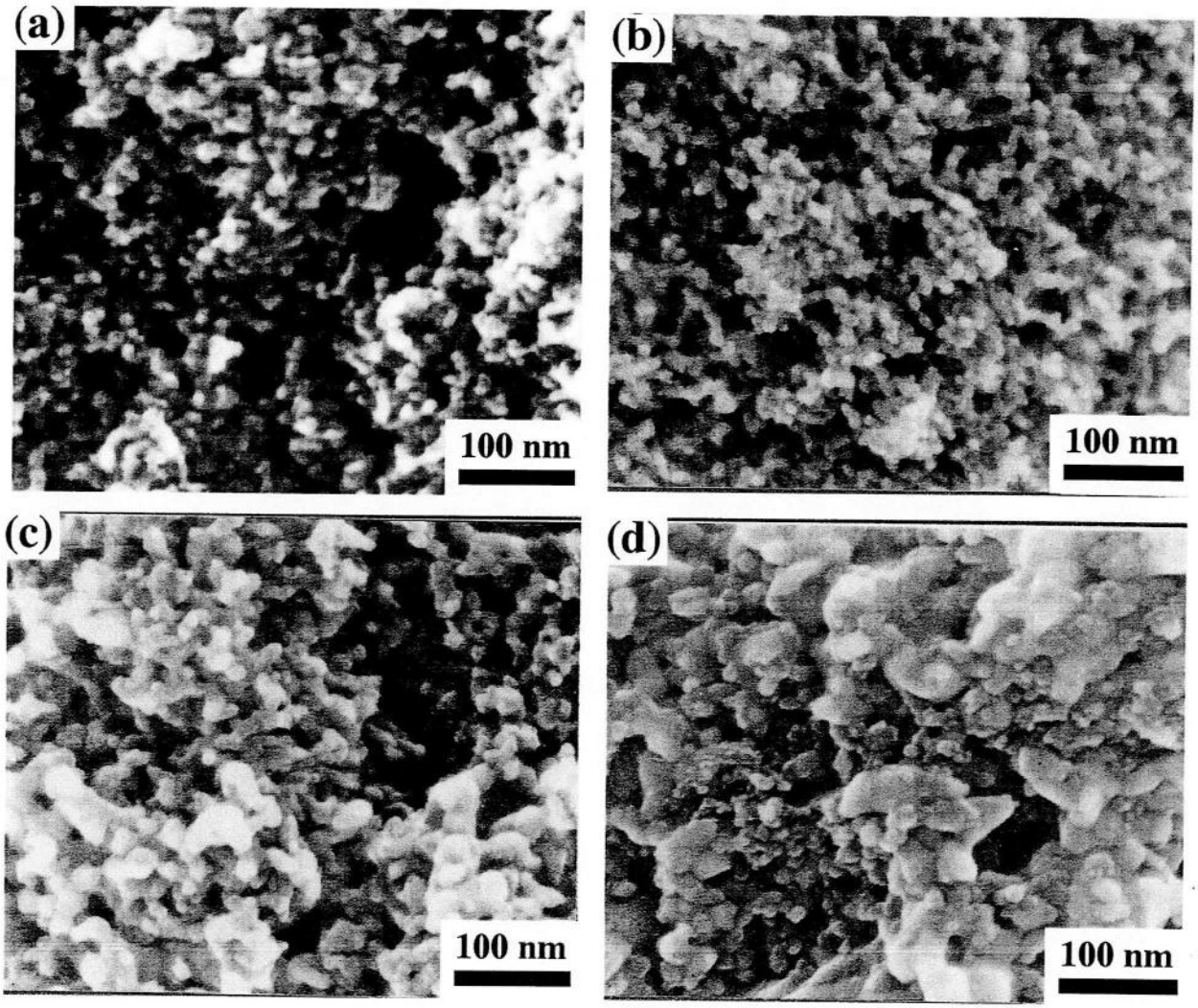

Fig. 4.5 The scanning electron microscopy micrographs of the as-compacted iron-oxide/silver nanocomposites : (a) He gas of 0.1 Torr , (b) 1.0 Torr (ACS), (c) 5.0 Torr and (d) 10 Torr (ACL).

This result suggests that the grain size depends on the helium gas pressure. We investigated the grain size change for two nanocomposites with the smallest (denoted by ACS) and largest (denoted by ACL) grain sizes. The compositions of the nanocluster composites were analyzed by EDS, which indicated that the iron content ranged from 20 to 30 at.%. In addition, a specific microstructure feature for the nanocluster composite prepared at a helium gas pressure of 1.0 Torr was obtained by TEM observations as shown in Fig. 4.6.

Figure 4.6 shows the high magnification TEM micrograph of the nanocluster composite obtained at a helium gas pressure of 1.0 Torr (denoted by ACS), corresponding to Fig. 4.5 (b). The grains were in almost spherical shapes and involved lattice fringes indicating crystalline features. Intragranular iron nanocluster of 1~3 nm was observed within the silver matrix particles. This observation was rationalized by the helium gas pressure. At a high helium gas pressure, each iron and silver vaporized atom rapidly and independently formed first nuclei of its the each other, and these nuclei were grown up. However, at a low helium gas pressure, iron vapor formed the nuclei because of high evaporation rate [36-38], and subsequently, this iron nucleolus acted as a substrate for heterogeneous nucleation of silver. Therefore, it is believed that intragranular iron particles existed within the silver particles. An EDX analysis with an electron beam focused on a region of 20 nm indicated that the components of the grains consisted of silver and iron, as shown in Fig. 4.6 (c), which showed that iron particles of a few nanometers were surrounded by silver grains during the evaporating. However, some large intergranular iron oxide particles are also observed with intragranular particles due to agglomeration.

Figure 4.7 is a micrograph of the same material after heat treatment in the oxidizing atmosphere (subsequently O_2-annealed sample; OAS). As obtained at the grain indicated by arrow in Fig. 4.6 (b), OAS which shows that the substructure of clusters persists in spite of slight, but significant grain growth to 19 nm in average. The average size of the nanoclusters in a grain was found to be grown to 5 nm, and nanocluster number in a grain decreased after the treatment.

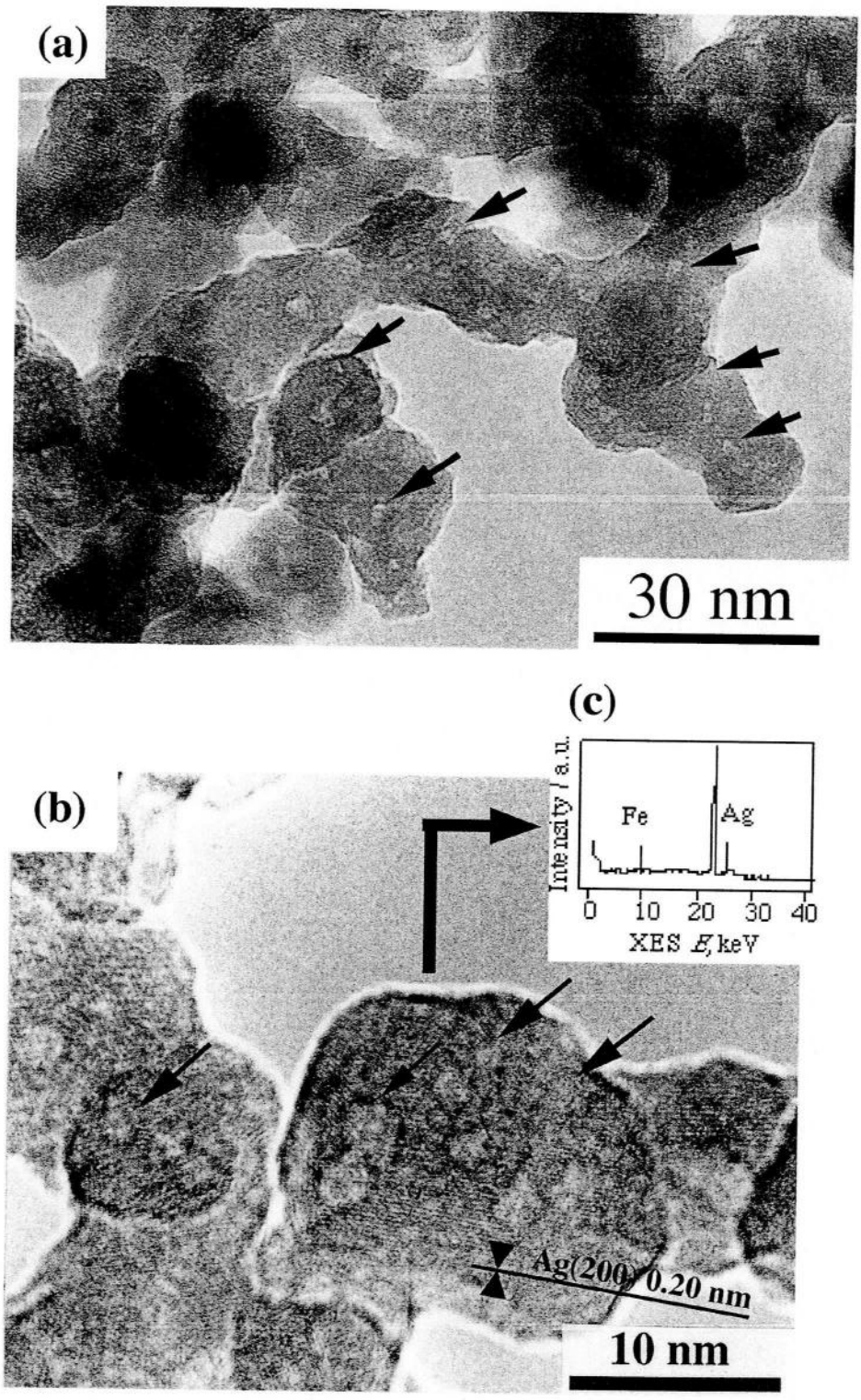

Fig. 4.6 (a), (b) The transmission electron microscopy micrograph of ACS and (c) the energy dispersive X-ray spectroscopy spectrum at the grain of Fig. 4.6 (b).

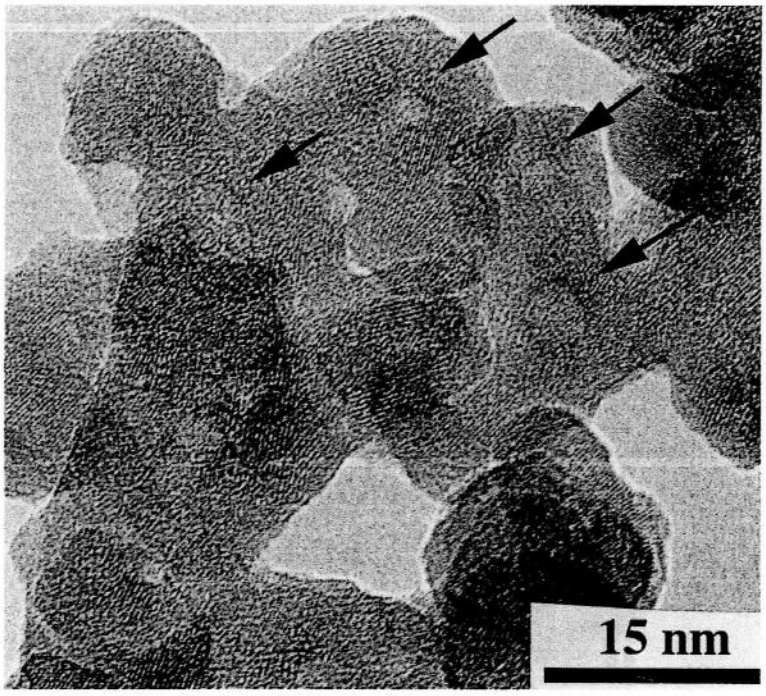

Fig. 4.7 The transmission electron microscopy micrograph of ACL.

The composition of the each nanocluster composite mixture was measured by X-ray near edge absorption spectroscopy (XANES) for as-compacted composites (ACS and ACL) and also measured for heat-treated ACS and ACL in an oxygen atmosphere at 473 K (denoted by OAS and OAL, respectively). Figure 4.7 shows Fe-*K* near edge derivative spectra for the present nanocomposites, along with some reference materials, such as Fe, Fe_3O_4 and γ-Fe_2O_3.

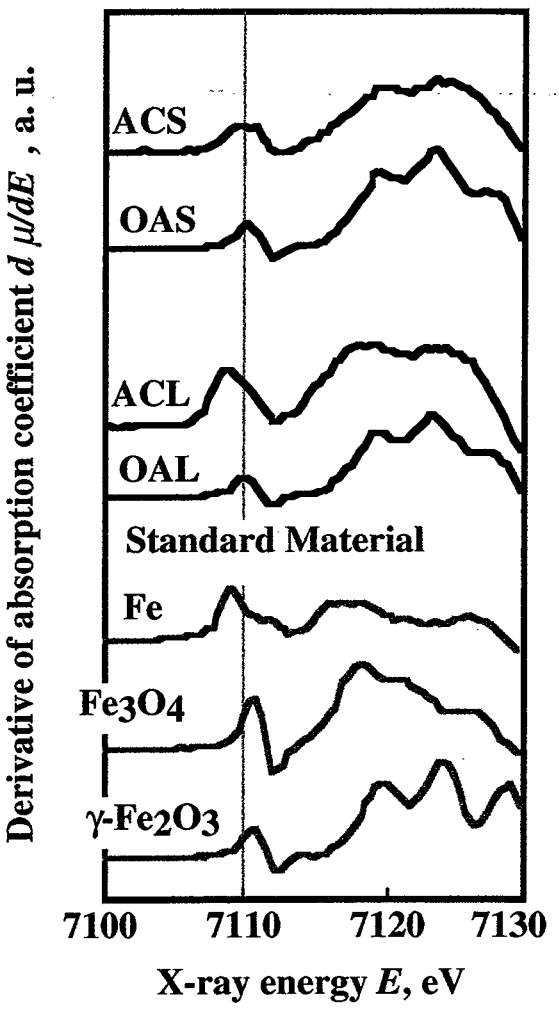

Fig. 4.8 XANES derivative spectra of silver/iron or iron oxide nanocluster composites and some reference materials.

The various features in the Fe-*K* near edge spectra corresponded to transitions from the Fe-1*s* orbital into low lying unoccupied states projected onto the Fe-site [51]. All of the oxide spectra exhibit a pre-edge feature in the 7112-7114 eV range associated with quadrupole allowed 1*s*-> 3*d* transitions. The dominant near edge features in the reference oxides, in the 7114-7132 eV range, are due to dipole 1*s* —> 4*p* and 1*s* —> continuum transitions (note that for pure Fe the onsets of these transitions are shifted down to the 7112-7114 eV range). Since the *s* —> *p* transition spectrum reflects the electronic structure of the covalent electrons in each oxide, its shape and location are characteristic of the specific oxide and important for their identification. As seen in the Fig. 4.8, a distinctive spectral shift to higher energy accompanies increases in the formal Fe valence states of the reference oxides. It should be noted that the present nanocluster composites, especially

the O_2-annealed samples, have spectra quite similar to that of γ-Fe_2O_3. This fact shows that metallic iron subgrains encompassed by silver can be oxidized by O_2-annealing. This is because, the oxygen diffuses more freely through solid silver than through any other metal [43, 44]. The broadening of the these subpeak structure in the nanocomposite spectra is presumably related to local disorder disruption of the final *p*-states [53].

The XANES spectra of the as-compacted samples (ACS and ACL) shows significant differences from γ-Fe_2O_3; both the peaks due to the $1s \longrightarrow 3d$ and $1s \longrightarrow 4p$ transitions have trailing features toward the lower energy direction. These differences are explained by the coexistence of metallic iron and Fe_3O_4 in the ACS and ACL. This metallic feature is much more remarkable in the ACL. This is due to iron with larger grain sizes, which cannot be fully oxidized at the slow oxidation rate.

The composition of the each nanocluster composite mixture was measured by SEM-EDX and TEM-EDX analyses and XANES for as-compacted nanocluster composites and oxidized composites at 473 K. For XANES measurements, the composition of the nanocluster composite was calculated from linear combination Fe-*K* near edge spectra and reference iron oxide spectra as in ref. [52] (Fig. 4.9). From these measurements, the both loose powder contained ca. 25 at.% iron, and the ratio of iron, Fe_3O_4 and γ-Fe_2O_3 was 24.3 at.%, 32.0 at.% and 43.7 at.% for ACS, and was 48.2 at.%, 25.9 at.% and 25.9 at.% respectively for ACL. Magnetic ultrafine particles in the nanometer scale prepared by evaporation are very easy to burn and need a protective coating to resist oxidation when exposed to the ambient. The remaining metallic iron was completely oxidized to γ-Fe_2O_3 by the heat treatment in oxygen atmosphere at 473 K, and silver was found to exist as a stable metal by X-ray diffraction up to 473 K.

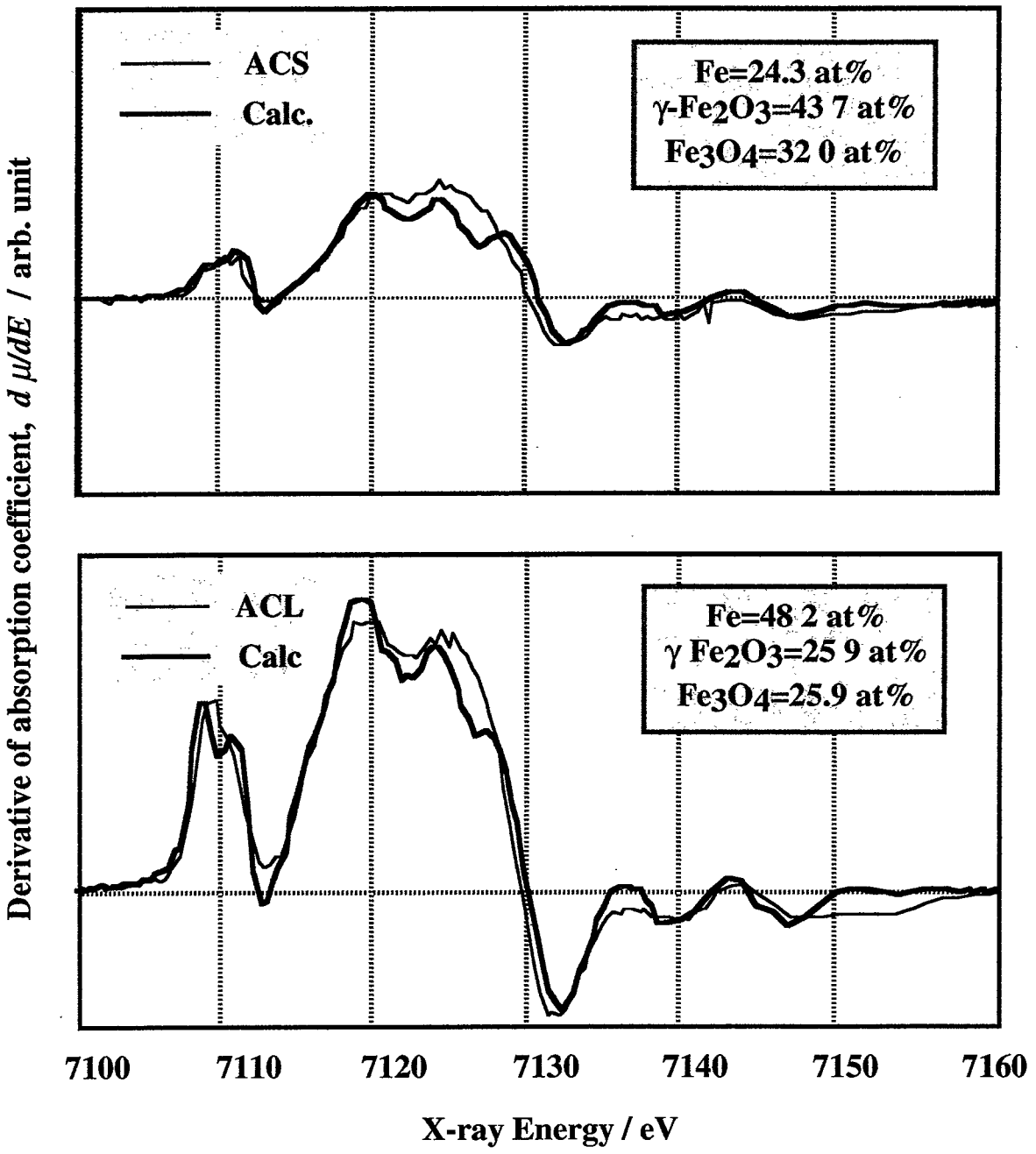

Fig. 4.9 Fe-*K* near edge spectra of nanocluster composites, which are drawn in derivative pf the absorption coefficient in terms of X-ray energy. Comparison of ACS and ACL spectra with a spectra calculated from a linear combination of the reference spectra, Fe, Fe_3O_4 and γ-Fe_2O_3.

4.4 Conclusion

Nanocluster composites with various particle sizes of iron or iron oxide were successfully fabricated by controlling the helium gas pressure from 1 to 10 Torr. The nanostructure and phase transformation of the nanocluster composites was investigated by SEM, TEM and XANES. The nanocluster size of the composites increased with increasing helium gas pressure for the loose powder. For the loose powder prepared at 1.0 Torr, a specific nanostructrure with intragranular iron nanoclusters of 1~3 nm was observed within the silver matrix particles with a size of 12 nm. The XANES and TEM results are consistent and indicate that an inhomogeneous mixture of Fe, Fe_3O_4 and γ-Fe_2O_3 occurs in the as-compacted material. After the O_2-annealed, the iron or iron oxide nanocluster was sticking each other and it turned to the core/shell structure in abroad sense, and these three species (Fe, Fe_3O_4 and γ-Fe_2O_3) were fully oxidized to γ-Fe2O3.

Reference

[1] D.L. Leslie-Pelecky and R.G. Rieke, *Chem. Mater.*, **8** (1996) 1770.

[2] C.L. Chien, in: G.C. Hadjipanayis, G.A. Prinz (Eds.), "*Science and Technology of Nano-structured Magnetic Materials NATO ASI Series B*", **vol. 259**, Plenum Press, 1991, p. 4772.

[3] C.L. Chein, *Annu. Rev. Mater. Sci.*, **25** (1995) 129.

[4] W.T. Coffey, P.J. Cregg, Yu.P. Kalmykov, *Adv. Chem. Phys.*, **83** (1993) 263.

[5] J. Zhang, C. Boyd and W. Luo, *Phys. Rev. Lett.*, **77** (1996) 390.

[6] F. Bodker, S. Morup, M.S. Pedersen, P. Svedlindh, G.T. Jonsson, J.L. Garcia Palacios and F.J. Lazaro, *J. Magn. Magn. Mater.*, **177-181** (1998) 925.

[7] Y.G. Yoo, D.S. Yang. S.C. Yu. W.T. Kim and J.M. Lee, *J. Magn. Magn. Mater.*, **203** (1999) 193.

[8] H. Kronmuller, R. Fischer, M. Bachmann and T. Leineweber, *J. Magn. Magn. Mat.*, **203** (1999) 12.

[9] E.F. Kneller, F.E. Luborsky, *J. Appl. Phys.*, **34** (1963) 656.

[10] R.D. Shull, J.J. Ritter, A.J. Shapiro, L.J. Swartzendruber and L. H. Bennet, *J. Appl. Phys.*, **67** (1991) 248.

[11] R.D. Shull, H.M. Kerch and J.J. Ritter, *J. Appl. Phys.*, **78** (1994) 6840.

[12] J.M.D. Coey, *Phys. Rev. Lett.*, **27** (1971) 1140.

[13] Q.A. Pankhurst and R. J. Pollard, *Phys. Rev. Lett.*, **67** (1991) 248.

[14] K. Haneda, A. H. Morrish, *J. Appl. Phys.*, **63** (1988) 4258.

[15] C.C. Papaefthymiou, *Phys. Rev. B*, **46** (1992) 10366.

[16] A.H. morrish, in: J.L. Dormann, D. Fiorani (Eds.), "*Magnetic Properties of Fine Particles*", Elsevier, Amsterdam, 1991, p. 181.

[17] F.E. Spanda, A.E. Berkowitz and N.T. Prokey, *J. Appl. Phys.*, **69** (1991) 4475.

[18] S. Morup, h. Topsoeand J. Lipka, *J. de Phys.*, **37** (1976) C6-287.
[19] J.C. Slonczewski, *J. Magn. Magn. Mater.*, **117** (1992) 368.
[20] F. Bodker, S. Morup and S. Linderoth, *Phys. Rev. Lett.*, **72** (1994) 282.
[21] L. Zhang, G.C. Papafthymiou and J.Y. Ying, *J. Appl. Phys.*, **81** (1997) 6892.
[22] Q.A. Pankhurst, R.J. Pollard, *J. Appl. Phys.: Condens. mater.*, **5** (1993) 8487.
[23] A.E. berkowitz, F.T. Parker, F.E. Spada, D. Margulies, in: J.L. Dormann, D. Fiorani (Eds.), "*Magnetic Properties of Fine Particles*", Elsevier, Amsterdam, 1991, p. 309.
[24] R.F. Ziolo, US Patent 4474866 (1984).
[25] D.J. Graves, M.A. Burns, US Patent 4675113 (1987).
[26] B.B. Schwartz, N.B. Blakemore, US Patent 4677067 (1987).
[27] J.W.M. Bulte, T. Douglas, S. Mann, R.B. Frankel, B.M. Moskowitz, R.A. Brooks, C.D. Baumgarner, J. Vymazel, M.-P. Strub and J.A. Frank, *Magn. Reson. Imaging*, **4** (1994) 497.
[28] L. Josephson, J. Bigler and D. White, *Magn. Reson. Med.*, **22** (1991) 204.
[29] J.S. Helman and B. Ables, *Phys. Rev. Lett.*, **22** (1976) 1429.
[30] H. Fujimori, S. Mitani and S. Ohnuma, *Mater. Sci. Eng.*, **31** (1995) 219.
[31] T. Furubayashi and I. Nakatani, *Mat. Sci. Eng.*, **A21** (1996) 307.
[32] B. Bian and Y. Hirotsu, *Jpn. J. Appl. Phys.*, **36** (1997) L1232.
[33] B. Bian, Y. Hirotsu and A. Makino, *Nanostruct. Mat.*, **8** (1998) 1057.
[34] K. Sato, B. Bian, Y. Hirotsu and A. Makino, *J. Mag. Soc. Jpn.*, **23** (1999) 1177.
[35] R.D. Shull, R.D. McMichael and J.J. Ritter, *Nanostruct. Mater.*, **2** (1993) 205.
[36] T. Nakayama, T.A.Yamamoto, Y.-H. Choa and K. Niihara, *Key Eng. Mater.*, **161-163**, 497 (1999).
[37] T.A. Yamamoto, R.D. Shull, P.R. Bandaru, F. Cosandey and H.W. Hahn, *Jpn. J. Appl. Phys.*, **33** (1994) L1301.
[38] T. Nakayama, T.A. Yamamoto, Y.-H. Choa and K. Niihara, "*Extended Abstracts of First Asian-Australasian Conference on Composite Materials*", **2** (1998) 505.
[39] T.A. Yamamoto, R.D. Shull and H.W. Hahn, Nanostruct. Mater., **9** (1993) 539.
[40] T.A. Yamamoto, M.C. Croft, R.D. Shull and H.W. Hahn, Nanostruct. Mater., **6** (1995) 965.
[41] D. de Caro, T.O. Ely, A. Mary, B. Chaudret, E. Snoeck, M. Respaud, J.-M. Broto and A. Fert, *Chem. Mater.*, **8** (1996) 1987.
[42] A. Sieverts and J. Hagenacker, *Z. Phys. Chem.*, **68** (1910) 115.
[43] F.G. Donnan and T.W.A. Shaw, *J. Soc. Chem. Ind.*, **29** (1910) 987.
[44] L.J. Swartzendruber, *Bull. Alloy Phase Diagrams*, **6** (1984) 5.
[45] T. Mishima and T. Sato: "*Handbook of Steel Materials*", Maruzen, Tokyo (1967) p. 1444.
[46] J. Stohr: "*NEXAFS Spetroscopy*", Springer, Berlin (1992).
[47] H. Oyanagi and D. Tweet, *J. Surface Sci. Soc. of Jpn.*, **18** (1997) 2.
[48] S. Yoshida, *J. Surface Sci. Soc. of Jpn.*, **18** (1997) 21.
[49] T. Ohta, P.M. Stefan, M. Nomura and H. Sekiyama, *Nucl. Instrum. Methods*, **A 246** (1986) 373.
[50] Y. Kitajima, *J. Electron Spectrosc. Relat. Phenom.*, **80** (1996) 405.
[51] L.A. Grunes, *Phys. Rev.*, **B27** (1983) 2111.
[52] T.A. Yamamoto, M.C. Croft, R.D. Shull and H.W. Hahn, *Nanostruct. Mater.*, **6** (1995) 965.
[53] A.H. Morrish and X.Z. Zohu. "*Science and Technology of Nanostructured Materials, NATO ASI Series B: PHysics vol. 259*", Plenum Press (1991).

CHAPTER 5

Magnetic Properties of Superparamagnetic Nanocluster Composites Composed of Iron-Oxide and Silver

5.1 Introduction

The magnetocaloric effect is a process converting magnetic energy into thermal energy, which is described by a relation of $Q = T\Delta S$ where ΔS is entropy change of magnetic spins contained in a substance and Q is heat absorbed by it [1]. This ΔS is accompanied by an order-disorder transition of the magnetic spin system induced by applying and removing external magnetic field. Most substance gives only a trivial ΔS with an ordinary field strength at ambient temperatures, while some paramagnets and ferromagnets can give significant ΔS and work as magnetic refrigerants. However, they still require a large field of several Tesla even at cryogenic temperatures, lower than 20 K. In early 90's, it was predicted that some kind of nanostructured material would show highly enhanced magnetocaloric effect and make the magnetic refrigeration system work even with lower fields and at higher temperatures [2]. The required material is such that consists of ferromagnetic nanograins behaving as the unit magnetic moment in the material. When the nanograins are single-domained and magnetically isolated each other, and their magnetocrystalline anisotropy energies are smaller than the thermal energy, the superparamagnetism occurs. This magnetism may be the simplest of those expected to occur in the magnetic nanocomposites, and is reasonably described by the classical *Langevin* paramagnetism model. Its magnetocaloric effect was also described on the basis of this model and thermodynamics, indicating a considerable enhancement of ΔS [3].

The main purpose of this chapter is to calculate magnetic entropy change ΔS from magnetization data for examining enhancement in the magnetocaloric effect due to the nanostructure of the superparamagnetic nanocluster composites composed of iron or iron oxide nanocluster dispersed in a silver matrix [4-8]. Another purpose is to compare the magnetic properties with the nanostructure of nanocluster composites.

5.2 *Experimental Procedures*

5.2.1 Nanocluster Composite Samples

The nanocluster composites examined in this chapter are composed of an iron or iron oxide nanocluster and a silver matrix, which were synthesized by the inert gas condensation technique. As their synthesis method, microstructure and phase identification of the magnetic species have been already reported in chapter 4, they are merely briefed here.

5.2.2 Magnetic Properties Measurement

Magnetization Measurement

Magnetization has been measured by a SQUID magnetometer from 300 K down to 5 K. The maximum applied field was 5 T (= 50 kOe ≅ 3978 kA/m). Quarter loops were measured sequentially at intervals of 10-50 degree by cooling down the sample. Magnetization data sets measured at these temperatures were plotted against a function of a parameter, H/T, where T is temperature and H is applied magnetic field.

ZFC/FC Curves Measurement

Two different procedures were used for the DC magnetization experiments: (i) zero-field cooling (ZFC), where the sample was slowly cooled in zero field to a temperature of 5 K at which the measuring field of 100 Oe was switched on and the magnetization was measured after a specified elapsed time of 100 sec as a function of temperature, and (ii) field cooling (FC) where the field of 100 Oe was turned on at a temperature well above the superparamagnetic blocking temperature before the sample was cooled to 5 K.

Magnetocaloric Effect

In this work, magnetic entropy changes, ΔS, of the samples were evaluated from their data sets of M-H relations measured at various temperatures, T, where M is magnetization, and H applied magnetic field [3, 6]. By using thermodynamic Maxwell's relation,

$$(\partial S/\partial H)_T = (\partial M/\partial T)_H, \tag{5-1}$$

these data sets were converted into ΔS accompanied by a demagnetization, $H \rightarrow 0$, at T.

$$\Delta S = \int_H^0 (\partial S/\partial H)_T dH = \int_H^0 (\partial M/\partial T)_H dH. \tag{5-2}$$

This ΔS was numerically calculated by substituting the magnetization data, in which differentials

and integrals were replaced with finite differences and trapezoid areas, respectively. Equation (5-1) is valid only when M is regarded as a state property determined by independent variables of T and H. The ideal superparamagnet has magnetization described as vector sum of magnetic moment vectors which are independent of each other, which is expressed by using Langevin function $L(x)$ as,

$$M = N\mu L(x), \tag{5-3}$$

$$L(x) = \coth x - 1/x, \tag{5-4}$$

where $x = \mu H / k_B T$, k_B is the Boltzmann's constant, μ is size of the elemental moment and N is number of moments existing in the substance. By inserting eqs.(5-3) and (5-4) into eq.(5-2), formulation for ΔS of the ideal superparamagnet is obtained as

$$\Delta S / Nk_B = -1 + x\coth x - \ln\{(\sinh x)/x\}. \tag{5-5}$$

5.3 Results and Discussion

5.3.1 Superparamagnetic Behabior of Nanocluster Composites

The magnetization (emu/g) estimated from the data of iron concentrations from EDX and XANES measurements was plotted against H/T for the nanocluster composite as compacted powder obtained at helium pressure of (a) 1.0 and (b) 10 Torr in Fig. 5.1. All data points of samples lie on a single curve, providing evidence for the occurrence of superparamagnetism [11, 12]. The as-compacted sample prepared at a helium pressure of 1.0 Torr (denoted by ACS) showed superparamagnetic behavior down to 100 K, while the as-compacted sample prepared at a helium pressure of 10 Torr (denoted by ACL) showed this superparamagnetic behabior down to 150 K. This result is attributed to the difference in particle size between the ACS and ACL samples observed by TEM, as shown in Fig. 4.6 (a) and (b) of chapter 4, because the superparamagnetism of the sample with a smaller particle size persisted to a lower temperature.

To investigate the magnetic properties in detail, the magnetization curves, $M_{Total}(H)$, were separated into a ferromagnetic (denoted by FM) part and a superparamagnetic (denoted by SP) part by following the formula [11].

$$M_{Total}(H) = \frac{2M_{FM}^{S}}{\pi}\tan^{-1}\left[\frac{H \pm H_C}{H_C}\tan\left(\frac{\pi S}{2}\right)\right] + N_g\mu\left[\coth\left(\frac{\mu H}{kT}\right) - \left(\frac{\mu H}{kT}\right)^{-1}\right]. \tag{5-7}$$

The first term in equation (5-7) is a function to represent a FM hysteresis curve and the second is the Langevin function to express the SP component. M^s_{FM} and $N_g\mu$ ($=M^s_{SP}$) are saturation magnetizations corresponding to the FM and SP parts, respectively. S is a parameter of the squareness of the FM loop, i.e., the ratio of the remanent magnetization, M_R, to M^s_{FM}. The average magnetic moment giving rise to SP, μ, and number of the moments, N_g, in the SP fraction are obtained from the second term. Typical fits to the magnetization curves are shown in Fig. 5.2 for the ACS and ACL measured at 300 K. From this fitting, the SP fraction M^s_{SP}/M^s_{Total} was calculated for various temperatures as shown in Figure 5.3 In the same manner, the SP fraction, M^s_{SP}/M^s_{Total}, was also obtained for ACS and ACL heat treated in an oxygen atmosphere at 473 K (denoted by OAS and OAL, respectively).

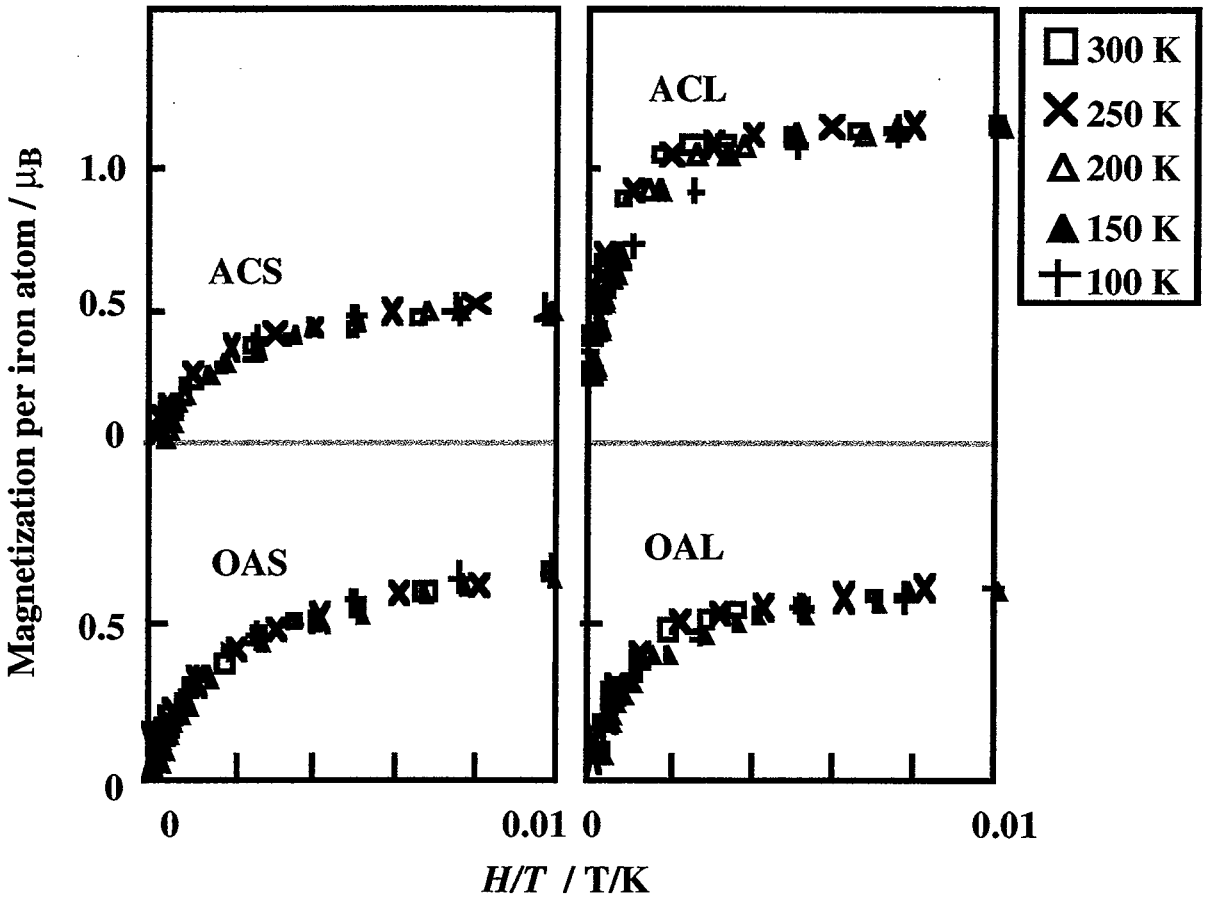

Fig. 5.1 M vs H/T plots indicating superparamagnetism in the silver/iron nanocluster composites.

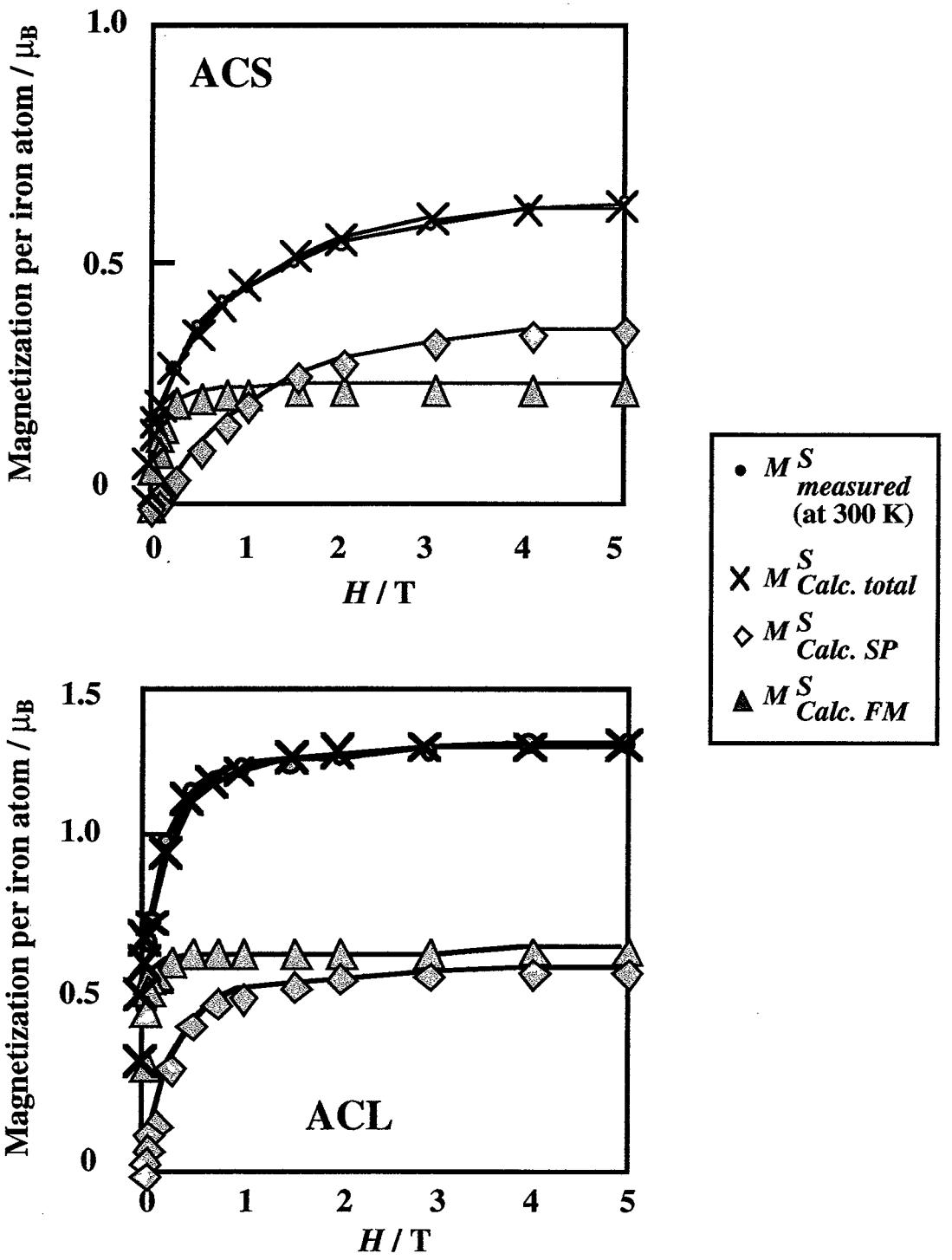

Fig. 5.2 Deconvolution of the total magnetization curves into FM and SP components measured at 300 K.

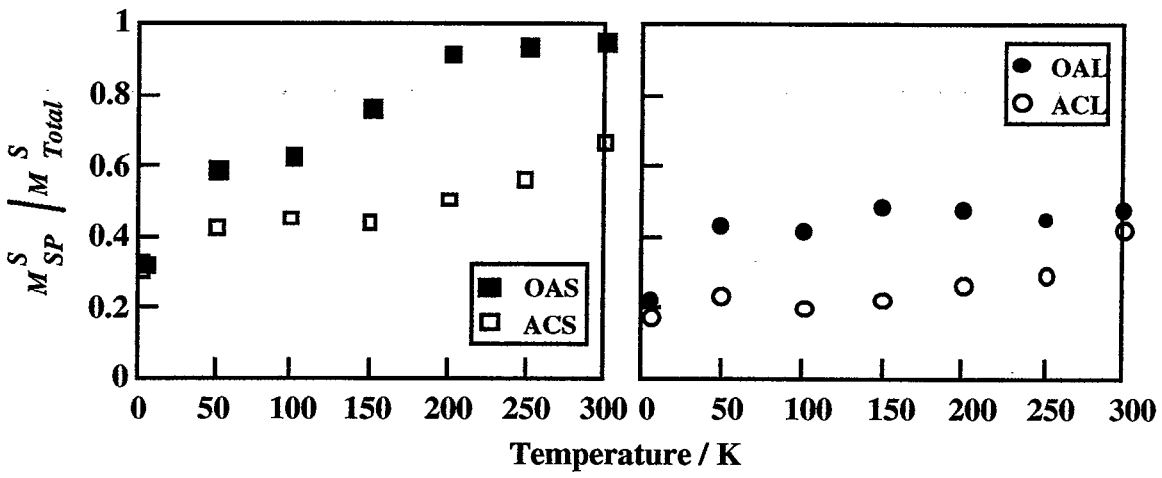

Fig. 5.3 Variation of the superparamagnetic fraction of the total moment, M^S_{SP}/M^S_{Total}.

From this approach, several features were observed; i) the SP fraction M^s_{SP}/M^s_{Total} significantly increased with increasing temperature for ACS and OAS, and the change of fraction for ACL and OAL with temperature was not significant compared with these for ACS and OAS, ii) the fraction for ACS is higher than that for ACL, and iii) the fraction for OAS and OAL is higher than these for ACS and ACL.

For these observations, the following deductions can be made. Firstly, at higher temperatures, the spin direction for magnetic nanoparticles was flipped by the higher thermal energy compared to the magnetic interaction energy and anisotropy energy. Therefore, the SP fraction increased with increasing temperature for ACL and OAL. On the other hand, the change of fraction for ACL and OAL with temperature was not significant compared with ACS and OAS with a lower SP fraction. This is attributed to the larger particle size including in ACL and OAL compared with ACS and OAS, because the larger one is relatively in sensitive to temperature. Secondly, the reason for the lower SP fraction for ACL with an even higher Fe phase content (48.2 at.%) than that for ACS (24.3 at.%) was closely related to the microstructure of each sample. From XANES and SEM-EDX measurements, the both ACS and ACL contained ca. 25 at.% iron, and the ratio of iron, Fe_3O_4 and γ-Fe_2O_3 phase was 24.3 at.%, 32.0 at.% and 43.7 at.% for ACS, and was 48.2 at.%, 25.9 at.% and 25.9 at.% for ACL, respectively. In general, a higher Fe phase content induced a smaller SP fraction due to a higher crystalline anisotropy energy and saturation magnetization for the same particle size compared with other components (Fe_3O_4 and γ-Fe_2O_3) in

the present composite systems, as discussed below. However, a different feature was observed for ACS. This could be caused by the intragranular iron nanoparticle of 1~3 nm within the silver matrix particle, as shown in Fig. 4.6 (a) and (b) of chapter 4. When the iron particle size is 1~3 nm, the iron also shows the superparamagnetism, and as a result, it is believed that the SP fraction for ACS is higher than for ACL.

The reason for observing a higher SP fraction by oxidization was a phase transformation of metallic iron to γ-Fe_2O_3. A γ-Fe_2O_3 phase is more easily in a superparamagnetic state than a metallic iron phase for the same particle size. The critical particle size to be in a superparamagnetic state for γ-Fe_2O_3 is larger than that for metallic iron at the same temperature, because the crystalline anisotropy energy (K_1) and saturation magnetization (σ_s) of γ-Fe_2O_3 are significantly lower than those of metallic iron. K_1 (ergs/cm^3) and σ_s (emu/g) at room temperature are -0.46 and 73.5 for γ-Fe_2O_3 and 4.8 and 217.2 [13] for metallic iron, respectively (see Table 2-I). Therefore, it is believed that a higher SP fraction was observed by oxidization, even though the nanocluster size was increased to 5 nm and 15 nm for OAS and OAL as discussed earlier.

Figure 5.4 shows the temperature dependent magnetization plots at 100 Oe for the ZFC and the FC cases of (a) OAS and (b) OAL sample. The ZFC curve of OAS sample exhibits a maximum at 80 K, which is associated with the average blocking temperature (T_B) of the nanocomposites for τ_m = 100 sec and $H_{appl.}$ = 100 Oe. This maximum shifts toward lower temperature as the applied field increases. The large width of the ZFC curve and the high collapse temperature of the ZFC and ZC curves (ca. 120 K) imply a broad nanocluster size or nanocluster anisotropy distribution in the composites [14-16]. The superparamagnetic blocking temperature was estimated with this method as indicated in Table 5-I. These results are in good agreement with SP fraction (Fig. 5.3) and nanostructure of nanocluster composites (in chapter 4).

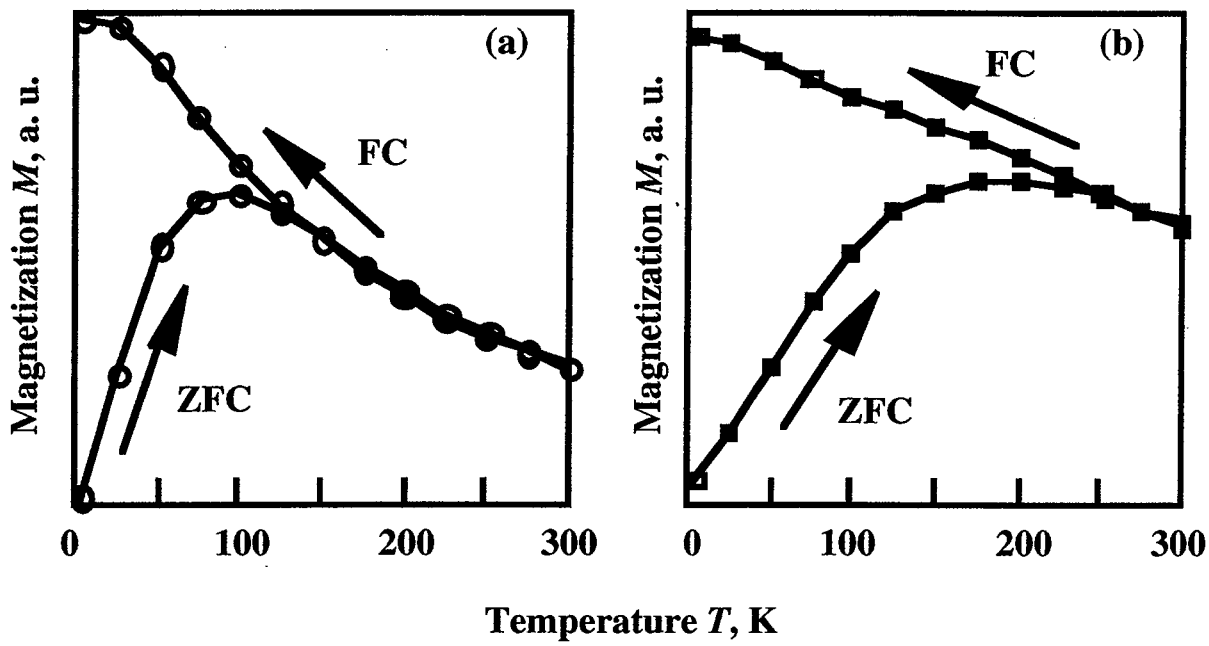

Fig. 5.4 DC magnetization versus temperature curves (FC and ZFC) for samples (a) OAS and (b) OAL, under an applied field $H_{appl.}$ = 100 Öe.

Table 5-I Variation of the superparamagnetic blocking temperature, T_B.

OAS	ACS	OAL	ACL
80 K	100 K	180 K	200 K

5.3.2 Magnetic Entropy Changes of Nanocluster Composites

Magnetic entropy changes were evaluated by substituting these data into eqs. (5-1) and (5-2) and are plotted in Figs. 5.5 against *H/T* for the OAS, ACS, OAL and ACL, respectively. The reliability of the present calculations was examined by checking the reproducibility of results of analytical formula when simulated sparse data were loaded. All samples were measured with larger intervals, and resultant ΔS were estimated to be relatively smaller than true ones about by 20 %.

It is noted that ΔS vs. H/T plots for the OAS and OAL show a clear tendency of falling on a single curve especially at higher temperatures (above 250 K), while not those for the ACS nor ACL. Equation (5-6) predicted such behavior for the ideal superparamagnet. This results are in good agreement with magnetization measurements and ZFC/FC measurements of these composites.

The enhancement in the magnetocaloric effect due to the nanostructure is now examined by comparing the superparamagnetic composite's ΔS with that of a paramagnet containing Fe^{3+} ion, iron ammonium alum. The alum's ΔS was calculated with $J = 5/2$ and $g=2$. The ΔS values for the OAS were compared with those of the paramagnet, iron aluminum alum with Fe^{3+}($\Delta S/k_B \cong 6\times10^{-5}$, at T=150 K, $H_{appl.}$=10 kOe), to find that an iron atom in the OAS ($\Delta S/k_B \cong 2\times10^{-4}$, at same conditions) gives entropy change ca. 30 times as large as that in the alum [17, 18].

The Langevin superparamagnetism should be physically too simple to describe magnetic spins behavior in the present nanocomposites involving much metastabilities, intimate heterogeneous contacts and inherent moment size distributions. It might be, in this sense, surprising that ΔS evaluated from their magnetization data is consistent with the Langevin model and other results of material characterization, though in limited temperature and applied field regions. Therefore, the present ΔS evaluation method would provide an effective guideline for optimizing synthesis process of new material for advanced magnetic refrigeration.

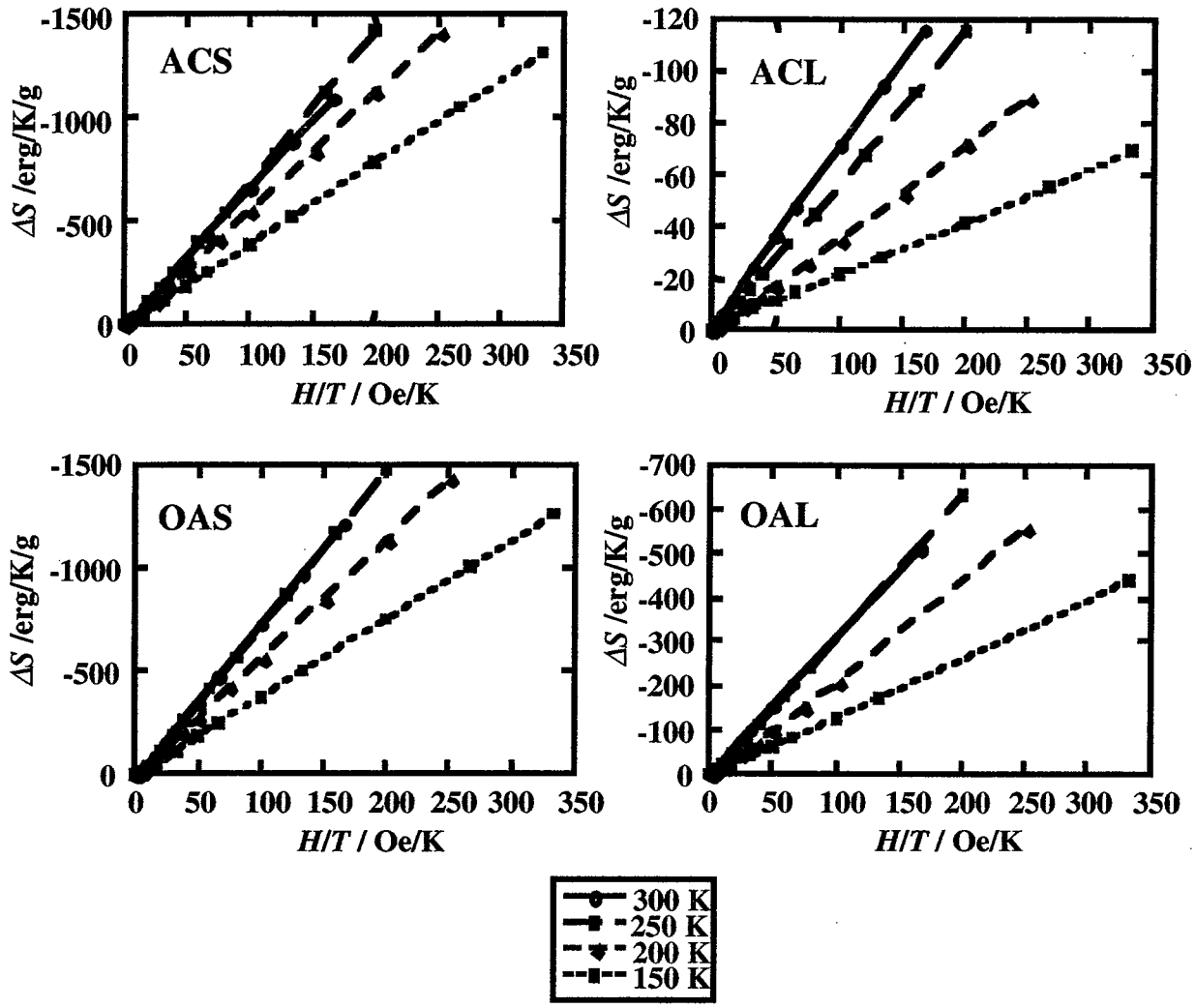

Fig. 5.5 Magnetic entropy change (ΔS) of ACS, ACL, OAS and OAL samples calculated from magnetization data.

5.4 Conclusion

The nanostructure of the iron oxide / silver nanocluster composites was investigated by TEM observation and the magnetic properties were measured by a SQUID magnetometer. The SP fraction of present samples are quite different from the sample with different grain size controlled by varying the helium gas pressures. To investigate the magnetic properties in detail, the magnetization curves, $M_{Total}(H)$, were separated into a ferromagnetic part and a superparamagnetic part. Oxidation of the loose powder induced the phase transformation of iron to γ-Fe_2O_3, and increased the superparamagnetism fraction.

Enhanced magnetocaloric effect due to the nanostructure of superparamagnetic nanocluster composite was demonstrated on the basis of magnetization measurements. The enhancement as ratio of its magnetic entropy change to that of paramagnetic alum containing the same iron atom was ca. 30 times.

References

[1] M.W. Zemansky, "*Heat and Thermodynamics, 5 th.*", McGraw-Hill (1972) p. 461.

[2] R.D. Shull, L.J. Swartzendruber and L.H. bennet: "*Proceedings of 6-th International Cryocoolers Conference*", ed. G. Green and M. Knox, David Tayler Res. Center Publ. #DTRC-91/002, Annapolis, MD (1991) 231.

[3] R.D. McMichael, R.D. Shull, L.J. Swartzendruber, L.H. Bennet and R.E. Watson, *J. Magn. Magn. Mater.*, **111** (1992) 29.

[4] T.A. Yamamoto, R.D. Shull, P.R. Bandaru, F. Cosandey and H.W. Hahn, *Jpn. J. Appl. Phys.*, **33** (1994) L1301.

[5] T. A. Yamamoto, K. Nishimaki, T. Harabe, K. Shiomi, T. Nakagawa and M. Katsura, *Nano-Struct. Mater.*, **12** (1999) 523.

[6] T. A. Yamamoto, M. Tanaka, T. Nakayama, K. Nishimaki, T. Nakagawa, M. Katsura and K. Niihara, *J. Appl. Phys., (to be accepted).*

[7] T. Yamamoto, M.C. Croft, R.D.Shull and H.W.Hahn, *NanoStructured Mater.*, **6** (1995) 965.

[8] K. Nishimaki, T.A. Yamamoto, T. Nakagawa and M. Katsura, *Jpn. J. Appl. Phys., (to be accepted).*

[9] T. Nakayama, T.A.Yamamoto, Y.-H. Choa and K. Niihara, *Key Eng. Mater.*, **161-163** (1999) 497.

[10] T. Nakayama, T.A. Yamamoto, Y.-H. Choa and K. Niihara, "*Proceendings of First Asian-Australasian Conference on Composite Materials*", **2** (1998) 505.

[11] M.B. Stearns and Y. Cheng, *J. Appl. Phys.*, **75** (1994) 6894.

[12] H. Akoh, Y. Tsukasaki, S. Yatsuya and A. Tasaki, *J. Cryst. Growth.*, **45** (1978) 495.

[13] W.D. Kingery, H.K. Bowen and D.R. Uhlmann, "*Introduction to Ceramics*", John Wiley and Sons (1976) pp. 987-1015.

[14] C. Papusoi, Jr., Al. Stancu and J.L. Dormann, *J. Magn. Magn. Mater.*, **174** (1997) 236.

[15] B.H. Sohn, R.E. Cohen and G.C. papaefthymiou, *J. Magn. Magn. Mater.*, **182** (1998) 216.

[16] M.F. Hansen, S. Morup, *J. Magn. Magn. Mater.*, **203** (1999) 214.

[17] T.A. Yamamoto, M. Tanaka, K. Shiomi, T. Nakayama, K. Nishimaki, T. Nakagawa, T. Numazawa, M. Katsura and K. Niihara, "*Proceedings of Material Research Society Symposium*" (in press).

[18] T.A. Yamamoto, M. Tanaka, T. Nakayama, K. Nishimaki, M. Katsura and K. Niihara *Journal of Applied Physics* (in contribution).

Chapter 6

Summary and Conclusions

In this thesis, the development of nanocluster based magnetic materials with multifunctionality was attempted by using both chemical and physical nanoprocessings. This thesis also investigated the influence of various sizes from 1 nm to several μm and dispersions of pure iron, its alloy or oxides on the improved mechanical and magnetic properties. Most efficient material is designed by a function of the targeted property and system, not constraint by nanocluster size (~10 nm), pure phase or clear interface. Special emphasis was placed on realization and application of structures and systems with novel functions via precursor nanoclusters. Use of nanoclusters aims to take advantage of not only properties that are caused by the confinement effects, larger surface area and interactions at length scales but also the possibility of generating transnormal atomic and macroscale structures. The main results and conclusions obtained in this study are summarized as follows:

In Chapter 2, MgO based nanocomposites with ferromagnetic iron particle dispersions were successfully fabricated by reduction and PECS process of MgO/γ-Fe_2O_3 composite powders prepared using a solution chemical route. The typical microstructure of MgO/Fe composites showed that dispersed Fe particles composed of intragranular Fe nano particles of a few 10 nm and intergranular Fe particles of several 100 nm. This distinguished microstructure was due to migration and coalescence of metallic Fe particles during the sintering. After metallic Fe particles were coalesced, the drag force of Fe particles was enhanced and the growth of MgO grain was inhibited. The fracture toughness increased with increasing volume fraction of iron particles. The increased toughness due to the crack deflection and plastic deformation of ductile Fe particles was clearly observed by SEM. Furthermore, MgO/Fe composites showed the enhanced coercive force compared to pure Fe materials, and this is due to intragranular nano-sized iron particles.

In Chapter 3, the MgO-based composites containing a bimodal distribution of intergranularly dispersed sub-micron sized and intragranularly dispersed nano-sized Fe, FeNi or FeCo alloys can be fabricated by a controlled powder preparation process. A fracture toughness of

2.35 MPam$^{1/2}$ was obtained for MgO/40 vol.% Fe composites. This high toughness was due to the crack deflection and bridging by intergranularly dispersed iron metal particles in sub-micron size. The coercive force for MgO/20 vol.% Fe composites was 55 Öe, which was approximately 50 times larger than that of pure Fe metal. It was due to the single-domain structure of intragranularly dispersed nano-sized Fe. In addition, good magnetic response for the applied stress was found in these ceramic/ferromagnetic-metal nanocomposites, showing the possibility of remote-sensing of fracture/deformation of ceramic materials.

In Chapter 4, a magnetic composite composed of iron-oxide and silver was fabricated by the inert gas condensation process combined with co-evaporation technique, *in situ* oxidation and *in situ* compaction techniques. Some of samples was post annealed in an oxidizing atmosphere of 10% O_2/He at 473 K. The particle size was controlled by varying helium gas pressure between 1.0 and 10 Torr, the smallest of which was about 12 nm at 1 Torr. The oxide phase was changed by annealing time. To study the correlation between the structure and the magnetic properties, microstructure and component of the composites were characterized by TEM, SEM and XANES (X-ray absorption near edge spectroscopy), and its magnetization was measured by a SQUID at various temperatures. It was found that some as-compacted samples exhibited the superparamagnetism evidencing magnetically isolated grains in single domain at temperatures higher than 150 K. TEM observation assisted with EDX was consistent with the magnetism, showing some silver grains include iron clusters of a few nanometer. By XANES measurement, as-compacted samples have the feature of metallic iron. After the O_2-annealing, γ-Fe_2O_3 substituted the metallic feature. This fact shows that metallic iron clusters encompassed by silver also oxidized by O_2-annealing.

In Chapter 5, the magnetic properties of the iron or iron-oxide/silver nanocluster composites was investigated by the magnetic properties were measured by a SQUID magnetometer. The superparamagnetic fraction of present samples are quite different from the sample with different grain size controlled by varying the helium gas pressures. The TEM observation assisted by EDX showed that some silver grains embrace nanoclusters of iron. It is also supported by calculated grain size of superparamagnetic part determined by fits of the M vs. H plots. The magnetocaloric effects of these nanocluster composites were evaluated by calculating the magnetic entropy changes from their magnetization data sets measured at various temperatures. The

magnetic nanocluster composite showed entropy changes higher than that of the conventional working substances for magnetic refrigeration, almost by one order. Enhancement of magnetocaloric effect observed for the composites with magnetic nanocluster was inferred as that due to the nanostructure of the grain-constituting phase.

In order to realize multifunctional materials, the novel fabrication method including both chemical process and physical process was devised to develop the nanocluster composite. In consideration of these results, the nanocluster based materials created in this work must be newly developed materials with multiple functionality. Finally, the author hopes that the concepts, findings and strategies obtained in this study will contribute to the progress in science and engineering in near future.

Appendix

The Iron Oxide Nanocrystalline Manufactured by IGC-PECS Process

A.1 Introduction

Recently, there has been a growing interest in a new class of materials called nanocrystalline, nanophase, nanostructured, or ultrafine-grained materials, consisting of nanoscale particles or grains (1-100 nm). These materials, which have a very high surface or interfacial area, exhibit dramatic changes in properties, such as enhanced sinterability at low temperatures, and high hardness [1-5]. Furthermore, much attention have been paid on artificially engineered nanostructured magnetic materials [6].

There are a number of techniques presently available for the synthesis of nanoparticles of oxides and non-oxides. Nanoparticles in the less than several 10 nm ranges are readily synthesized by precipitation in a liquid medium but may be contaminated and agglomerated. One of the primary concerns in powder processing is the control of agglomeration. An agglomerated mass of nanoparticles is of little benefit because coarsening prevails over sintering. The IGC process which is one of the powder synthesis process leading to little agglomeration [7], was accomplished to obtain the nanocrystalline iron-oxide materials.

On the other hand, γ-Fe_2O_3 powders have been used in magnetic tapes, magnetic disks, magnetic cards, etc. However, the mechanical and physical properties of γ-Fe_2O_3, such as hardness, Young's modulus and toughness, are little reported because it is difficult to fabricate the densified γ-Fe_2O_3 materials due to phase transformation containing from γ-Fe_2O_3 to α-Fe_2O_3 during the sintering. Therefore, in order to understand the mechanical/physical properties, it is important to fabricate the densified γ-Fe_2O_3 materials.

To obtain the densified γ-Fe_2O_3 materials, in this appendix, firstly the nanocrystalline powders enhancing the sinterability at low temperatures were prepared by IGC process. Secondly, using PECS method which enables to get the fine microstructure by rapid heating [8-10], the sintering was performed. Finally, the mechanical and physical properties are also described with magnetic property. Specially, in this appendix, much attention was paid on the relationship

between the microstructure and mechanical/magnetic properties of nano-grained γ-Fe_2O_3, comparing with α-Fe_2O_3.

A. 2 Experimental Procedure

A. 2. 1 Fabrication Procedure of Powders

Iron-oxide powder was synthesized by the inert gas condensation (IGC) method [11,12]. Metallic iron as source materials evaporated in an ultrahigh vacuum chamber filled with helium gas of a pressure between 0.1 and 10 Torr and collected the powders onto a rotating cold finger cooled by liquid nitrogen. After evaporating, only the iron particles were stabilized by a slow oxidation with O_2 gas. To compare the some of the properties, γ-Fe_2O_3 (Average particle size; 30 nm, NanoTech Co., Ltd., Illinois. USA.) was used. Sintering was performed by using PECS process which enables to get the fine microstructure by rapid sintering.

A. 2. 2 Pulse Electric Current Sintering

The pulse electric current sintering (SPS 3.20 MK-IV; Sumitomo Coal Mining Co., Ltd.) with an applied uniaxial pressure of 50-100 MPa was accomplished at 973-1273 K for 5 min. under an argon gas atmosphere for pure iron-oxide powder. The heating rate was fixed as 200 K/min for all sintering (applied current; 4000 A, and applied voltage; 3 V). After the given time, the pressure was relaxed and the specimens were immediately cooled. Sintered specimens, 15 mmϕ in diameter, were polished with 9, 3, and 0.5 mm diamond pastes until the specimens possessed mirror surfaces.

A. 2. 3 Evaluation

Phase and crystalline size analyses were done using X-ray diffraction (XRD) (Model RAD-B, RIGAKU Co., Japan), scanning electron microscopy (SEM) (Model S-5000, Hitachi Ltd., Japan) and transmission electron microscopy (TEM) (Model H-8100, Hitachi Ltd., Japan). The phase analysis in the nano-sized iron-oxide or metallic iron, in air as a function of temperature, were tracked using a dynamic high temperature X-ray diffraction (HT-XRD) using Cu*ka* radiation (Model DMS-2000 system, Scintag Co., U.S.A) system. The microstructures of the nanocomposites were studied by a TEM assisted by EDX. Magnetization measurements at room temperature were measured by a SQUID magnetometer (Model, MPMS-5, QUANTUM DESIGN, U.S.A) with the maximum field of 10 kÖe (=1 Tesla).

A. 3 Result and Discussion

A. 3. 1 Preparation of Nanocrystalline Iron-oxide Materials

The particle size fabricated by IGC process depends on the helium gas of a pressure between 0.1 and 10 Torr, and the smallest average particle size (S) was 8 nm for 0.1 Torr, and that of the largest (L), 28 nm for 10 Torr. This results were attributed to mean free path of evaporated particles dependent on helium gas of a pressure, and the shorter mean free path gives to coalescence of particles. The nanopowder, 8 nm, was used for investigation of several properties, and also, γ-Fe_2O_3 (Average particle size; 30 nm, NanoTech Co., Ltd., Illinois. USA.) was used to compare the some of the properties. Figure A.1 (a) and (b) show TEM micrographs of the iron-oxide nanoparticles obtained at helium gas pressures of 0.1 Torr (denoted by sample (S)), and γ-Fe_2O_3 (denoted by sample (L)) manufactured by NanoTech. respectively.

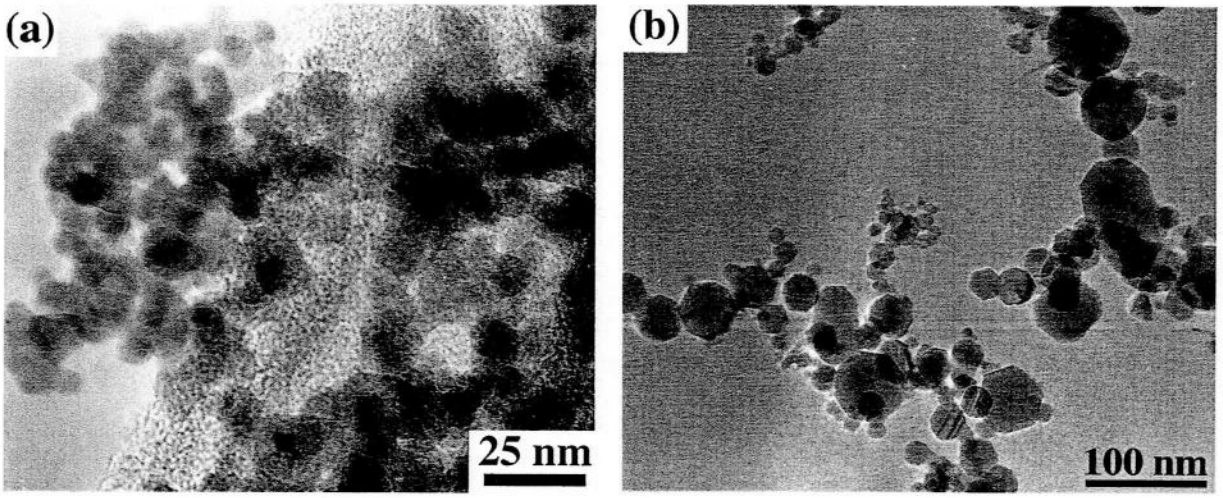

Fig. A.1 The transmission electron microscopy micrographs of (a) powder (S) and (b) powder (L).

Previous XANES and SQUID measurements [12] indicated that starting powders (S) consisted of Fe, Fe_3O_4, and γ-Fe_2O_3. Thermodynamic calculation predicts that most iron should oxidize in air at room temperature. However, the kinetics of the oxidation process are such as to limit the oxide formation to a thin region on the surface of iron. Further oxide formation requires mass transport (diffusion) through the oxide layer, and at a low temperature these diffusion rates are

so slow that the oxidation process can not continue. Therefore, the formation of Fe, Fe_3O_4, and γ-Fe_2O_3 at room temperature is due to the kinetics of oxidation process.

The phase analysis in sintered bodies from powder (S) and (L) at 1073 K, were tracked using a XRD system as shown in Fig. A.2. This result indicated that powders (S) and (L) consisted of γ-Fe_2O_3 and α-Fe_2O_3, respectively. It is well known that α-Fe_2O_3 phase is stable phase at high temperatures and it transforms to γ-Fe_2O_3 phase about 873 K [13]. The fully oxidized γ-Fe_2O_3 powder (L) transforms to α-Fe_2O_3 phase during the sintering and sintered materials is to be α-Fe_2O_3 at the room temperature. On the other hand, for sample (S), even sintered at 1073 K, γ-Fe_2O_3 phase still remained. This may be due to oxidation of Fe and Fe_3O_4 and rapid sintering rather than the formation of α-Fe_2O_3 during the sintering.

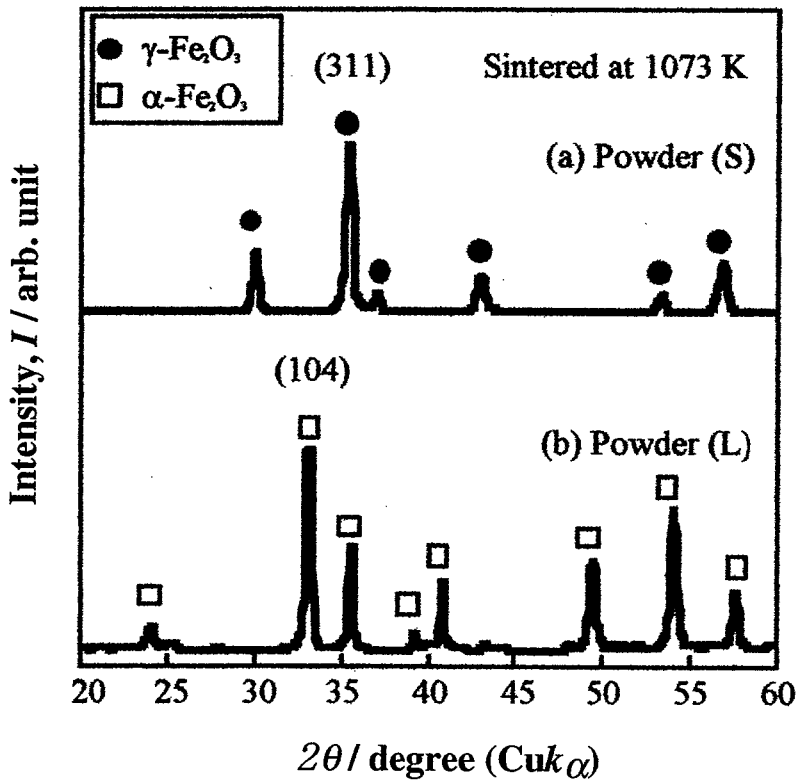

Fig A.2 X-ray diffraction patterns of sintered materials from (a) powder (S) and (b) powder (L) fabricated by the pulse electric current sintering process.

Figure A.3 shows typical SEM micrographs of the fractured surfaces of sintered bodies fabricated by PECS process. It may be observed that the microstructure of powder (S) is uniform and fine-grained; the grain size is in the range 5 to 50 nm, while the grain size for powder (L) is 10 to 150 nm. The grain size of sintered body is also calculated by Scherrer formula [14] were shown at Table A-I.

Table A-I Calculated grain size for sintered materials from powder (S) and (L).

PECS Temperature, T / K	**From Poeder (L) ($d_{av.}$=28 nm)**	**From Poeder (S) ($d_{av.}$=8 nm)**
873	**46.2**	—
973	**54.2**	—
1073	**60.4**	**37.6**
1173	**80.4**	—
1273	**58.9**	—

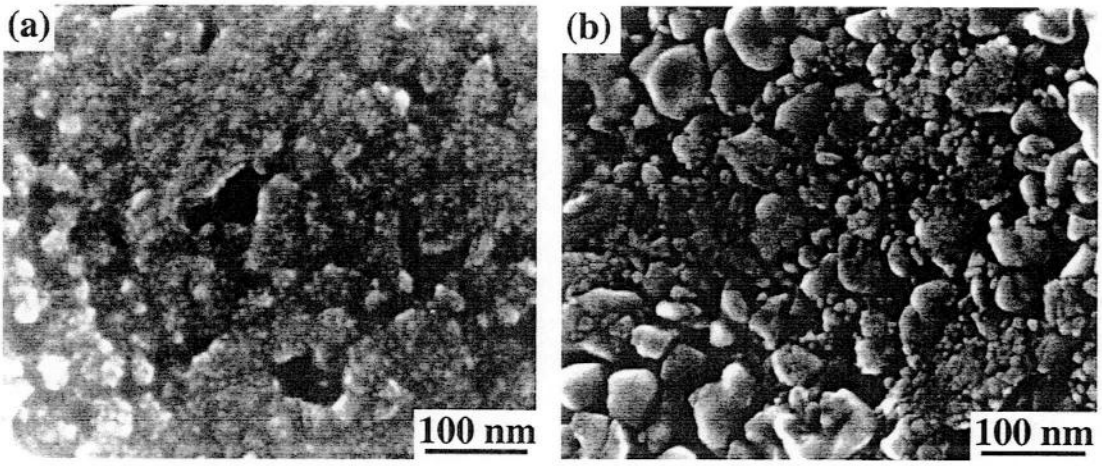

Fig. A.3 The typical scanning electron microscopy micrographs of sintered materials from (a) powder (S) and (b) powder (L) fabricated by the pulse electric current sintering process.

Figure A.4 shows typical HREM micrographs, in which several individual nanocrystalline grains can be identified. The lattice fringes visivle in this micrograph have spacings corresponding to the 0.295 nm (220) interplanar distances of the γ-Fe_2O_3 lattice. The structure of sintered body is almost fully crystalline and there is negligible evidence of extensive areas of amorphous and intergranular porosity. Lateral displacements of the lattice planes can be noted in the largest grain. These displacements indicate the existence of crystallographic shear planes (CSP). These kinds of lattice defects may be induced by rapid cooling of PECS.

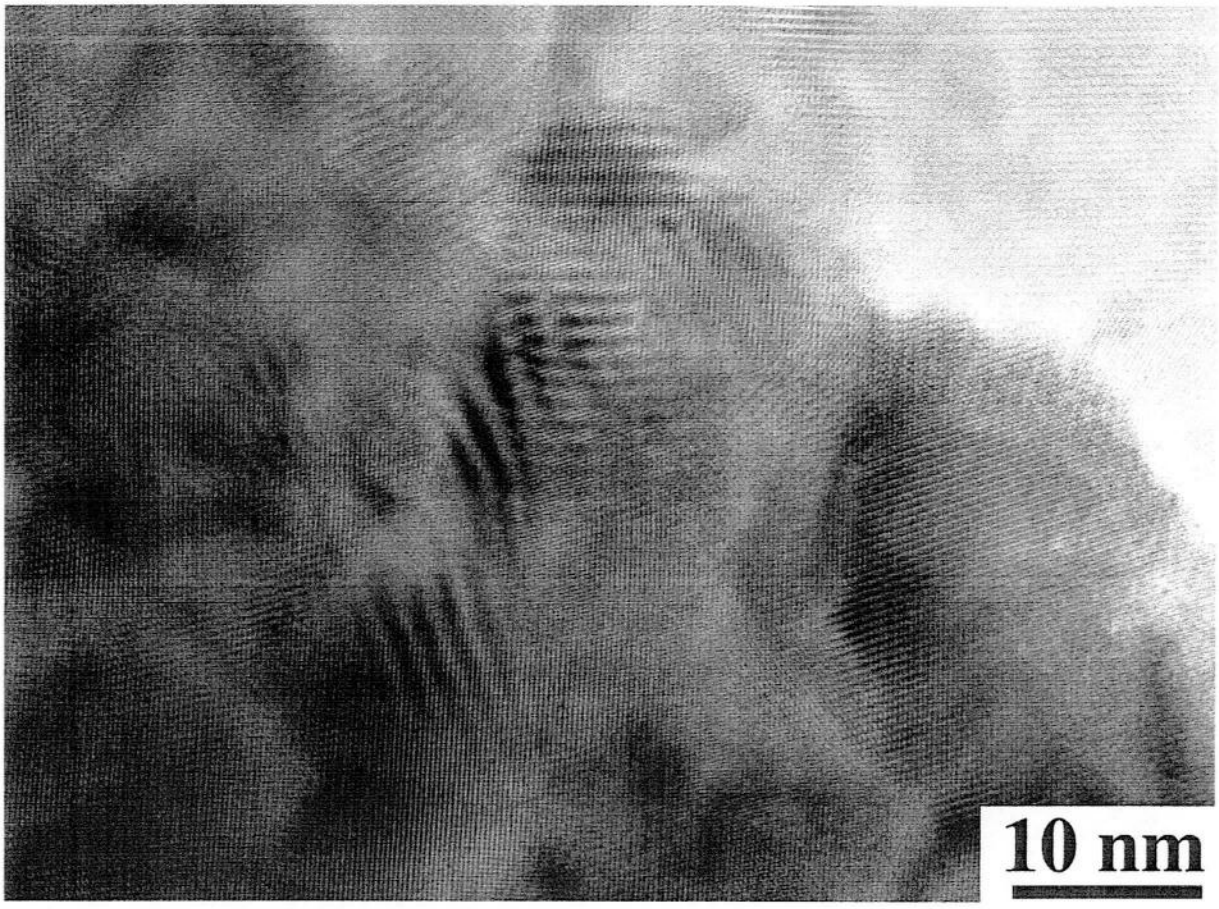

Fig. A.4 The typical high resolution transmission electron microscopy micrographs of sintered materials from powder (S) fabricated by the pulse electric current sintering process.

Figure A.5 shows the variation of relative density with sintering temperature and applied pressure of nanocrystalline iron oxide under the holding time of 5 min. It is obvious that the densification of powder (S) is much faster than that of powder (L) and the sintering temperature for full densification is lower. Relative densities above 99 % were obtained by PECS at 1073 K (powder (S)) and 1173 K (powder (L)) at applied pressure of 100 MPa. It is attributed to finer starting particle size as well as saving the transformation energy from γ- to α-phase for sample (S).

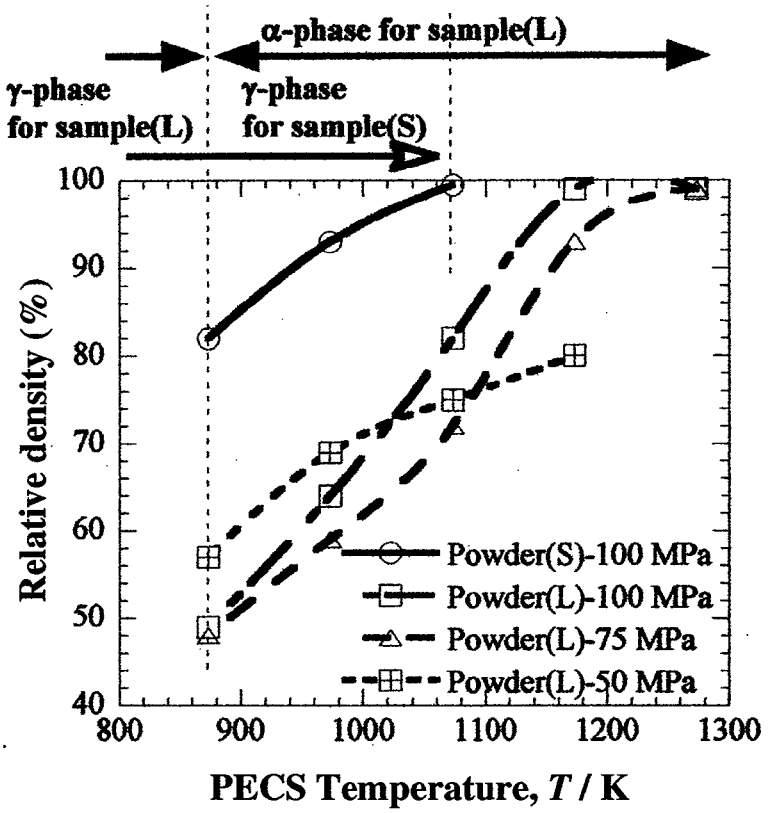

Fig. A.5 The variation of relative density with sintering temperature and applied pressure fabricated by the pulse electric current sintering process.

A. 3. 2 Mechanical Properties

Most extent experimental results on the mechanical behavior of nanocrystalline materials come from measurements of hardness [2-5]. It is commonly measured by Vickers hardness tester. It has long been observed experimentally in conventional materials that the hardness varied with the grain size through the empirical *Hall-Petch* relation. As expected from the results in conventional materials, the nanocrystalline γ-Fe_2O_3 material from powder (S) shows the higher hardness value

than reference data [15] as shown in Table A-II. Several previous reports on nanocrystalline ceramic materials admitted that the smaller grain size contributed to the hardening [2-5, 16]. A similar mechanism may be expected in the present case.

Table A-II The variation of Vickers Hardness for densified materials.

materials	Vickers Hardness (GPa) Fe
α-Fe_2O_3	5-7 *
γ-Fe_2O_3	4.04 *
α-Fe_2O_3 in this study	10.8-13.1
γ-Fe_2O_3 in this study	6.78

*** Reference data [15]**

Young's modulus measured by ultra sonic resonance method is increased with sintering temperature as shown in Fig. A.6. These results closely related to the relative density, and also saturated points show the sintering temperature to obtain the densified materials. It well agrees with the relative density data, and with the fact that the Young's moduli of γ-Fe_2O_3 and α-Fe_2O_3 are 150 GPa and 240 GPa, respectively.

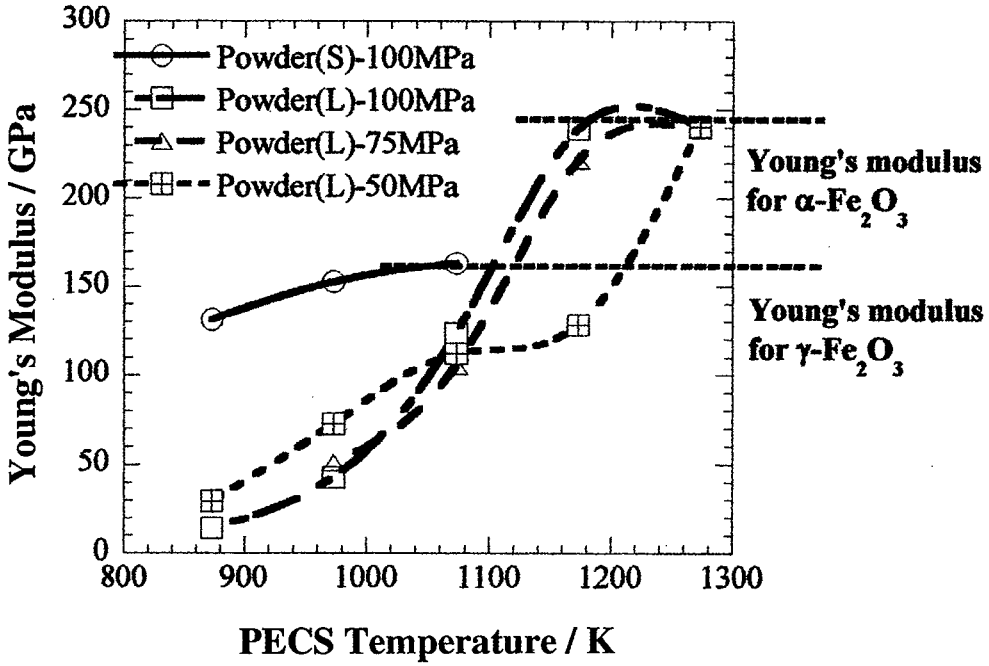

Fig. A.6 The variation of Young's modulus with sintering temperature and applied pressure.

A. 3. 3 Magnetic properties

In the former section, densified nano-grained γ-Fe_2O_3 can be fabricated by IGC process and following PECS method. In this section, the magnetic properties will be discussed for the nano-grained γ-Fe_2O_3 (from powder (S)) and α-Fe_2O_3 (from powder (L)) as reference materials. The dependence of magnetization (*M*) on the applied magnetic field (*H*) was shown in Fig. A.7.

The shape of the magnetization curve and the observed small hysteresis for γ-Fe_2O_3 suggests the ferromagnetic and superparamagnetic behavior. The saturation magnetization is achieved in applied magnetic fields that are above of 10 kÖe or below a value of –10 kÖe. Is is found to be 70 emu/g and 0.7 emu/g, which is almost same value with those of α-Fe_2O_3 and γ-Fe_2O_3 at room temperature, about 70-75 emu/g and 0.4 emu/g, respectively. However, the coercive force

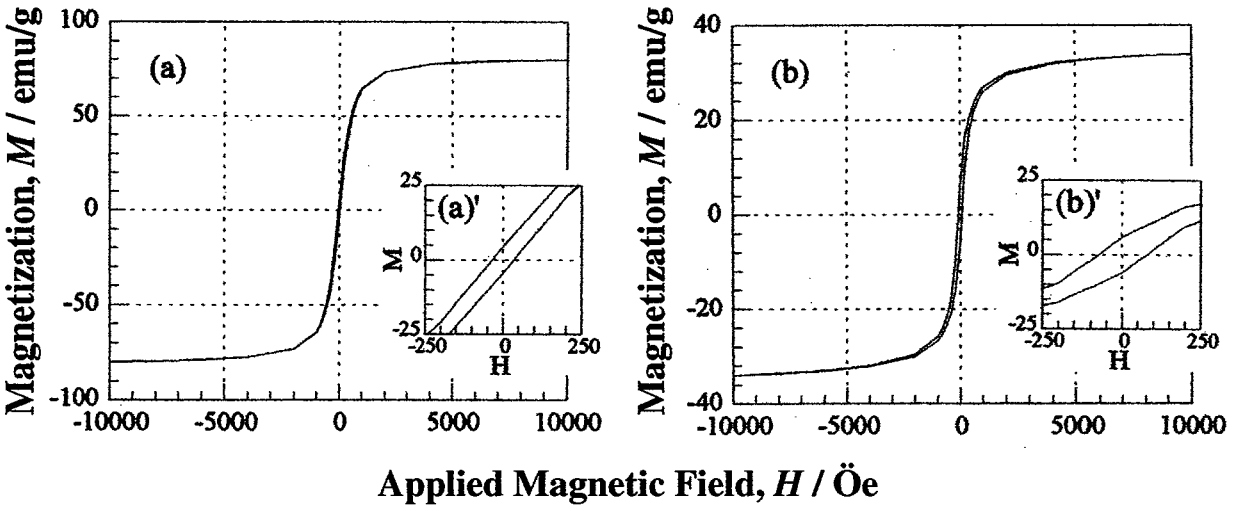

Fig. A.7 Room-temperature magnetization versus applied magnetic-filed curve for (a) γ-Fe_2O_3 (from powder (S)) and (b) α-Fe_2O_3 (from powder (L)) fabricated by the pulse electric current sintering process at 1073 K.

(H_C) of γ-Fe_2O_3 prepared from sample (S) is 35 Öe, which is approximately one order of magnitude lower than that of typical γ-Fe_2O_3 (200-450 Öe). Hc is well known to be strongly dependent on the particle size and shape [17, 18]. When the particle size of a magnetic material decreases, its magnetic structure varies from a ferromagnetic state to a paramagnetic state, to reduce the total magnetic energy of the system; hence, low H_C is presented [18]. Magnetic measurement of γ-Fe_2O_3 particles revealed that H_C decreased when the particle size was < 30 nm. The extremely low value of H_C was reported for particle size in the range of about 20 nm [19], which corresponds to the superparamagnetic structure. In the present experiments, the average grain size of nanocrystalline γ-Fe_2O_3 was 40 nm, and the grain size was distributed from 10 to 50 nm. It seems that the nanocrystalline γ-Fe_2O_3 powder might have a mixed structure composed of ferromagnetic and superparamagnetic structure. Furthermore, in case of γ-Fe_2O_3, particle shape also closely relates to H_C. There are two factors to determine H_C for γ-Fe_2O_3. One is due to magnetic anisotropy of crystallography, and another is due to magnetic anisotropy of particle shape (depends on aspect ratio). The prediction values of H_C for γ-Fe_2O_3 due to magnetic anisotropy of crystallography and magnetic anisotropy of particle shape are 110 Öe and 1150 Öe in the random distribution, respectively. Therefore, H_C was predicted to be 110 Öe for the nano-grained γ-Fe_2O_3 (from powder (S)) because the particle shape is spherical. Generally, the particles are usually packed tightly together so that the residual magnetization or induction in high. However, if the particles are packed together too tightly, they lose their single-domain characteristics and coercive force is reduced. Consequently, the low H_C value of the densified γ-Fe_2O_3 is attributed to the spherical particle shape and high density.

A.4 Summary

Nanocrystalline iron-oxide powder was prepared by an inert gas condensation (IGC) method combined with evaporation, and the densified nano-grained γ-Fe_2O_3 was fabricated with the IGC process and PECS method. For these materials, the following results were obtained :

(1) The grain size of nanocrystalline iron oxide materials could be controlled by varying the helium gas pressures and sintering temperature.

(2) The densified γ-Fe_2O_3 with 40 nm in grain size was obtained at sintering temperature of 1073 K from nanocrystalline powder which was prepared under lower helium gas pressures.

(3) The higher hardness of ≈7 GPa was obtained for the densified nanocrystalline γ-Fe_2O_3 with ≈40 nm in grain and the Young's modulus of γ-Fe_2O_3 was 160 GPa.

(4) The densified γ-Fe_2O_3 materials and its nanocrystalline powders exhibited the combined properties of ferromagnetism and/or superparamagnetism and their magnetic properties strongly depended on the microstructure and particle morphology.

References

[1] H. Gleiter, *Progress in Mat. Sci.*, **4** (1990) 33 .

[2] R. Uyeda, *Progress in Mat. Sci.*, **5** (1991) 15 .

[3] R.W. Siegel and G.E. Fougere, *Nanostuct. Mater.*, **6** (1995) 205.

[4] F. Wakai, S. Sakaguchi and Y. Matsuno, *Adv. Ceram. Mater.*, **1** (1986) 259.

[5] T.G. Nieh and J. Wadswonh, *Acta Metall.*, **38** (1990) I 121 .

[6] T. Yamamoto, R.D. Shull and H.W. Hahn, *NanoStruct. Mater.*, **9** (1997) 539.

[7] G. Skandan and B. H. Kear, *Materials Science Forum*, **243-245** (1997) 217.

[8] N. Tamari, T. Tanaka, K. Tanakla, I. Kondoh, M. Kawahara and M. Tokita , *J. Ceram. Soc. Jpn.*, **103** (1995) 740.

[9] I. Kondoh, T. Tanaka, and N. Tamari , *J. Ceram. Soc. Jpn.*, **102** (1994) 505.

[10] Y. H. Choa, H. Kawaoka, T. Sekino, and K. Niihara, *Key Eng. Mater.*, **132-133** (1997) 2009.

[11] T. Yamamoto, R. D. Shull, P. R. Bandaru, F. Cosandey, and H. W. Hahn, *Jpn. J. Appl. Phys.*, **33** (1994) L1301.

[12] T. Nakayama, T.A. Yamamoto, Y. H. Choa, and K. Niihara, *Key Eng. Mater.*, **161-163** (1999) 497.

[13] T. Yamakuchi and H. Yanakida: "*Magneto Ceramics*", Ceramics Science series vol. IV, Gibouto Pub. Com. (1985) p. 178.

[14] B.D. Cullity: "*Elements of X-ray Diffraction*", 2nd Edition, Addison-Wesley Pub. Com. Inc. (1984) p. 102.

[15] I.J. McColm: "*Ceramic Hardness*", Plenum Pub. Corp. (1990) p. 282.

[16] H. Hahn and K. A. Padmanabhan, *NanoStruct. Mater.*, **6** (1995) 191.

[17] J.E. Knowles, *IEEE Trans. Mag.*, **MAG-16** (1980) 62.

[18] S. Tochihara, and Y. Imaoka, *IEEE Trans. Mag.*, **MAG-6** (1973) 808.

[19] T. Yamakuchi and H. Yanakida: "Magneto Ceramics", Ceramics Science series vol. IV, Gibouto Pub. Com. (1985) p. 241.

List of Publications

1) Structures and Magnetic Properties of Iron-Oxide/Silver Nanocomposite
T. Nakayama, T. Yamamoto, Y.-H. Choa and K. Niihara
Key Engineering Materials, **161-163** (1999) 497-500.

2) The Iron Oxide Nanocrystalline Manufactured by IGC-PECS Process
T. Nakayama, Y.-H. Choa, T. A. Yamamoto and K. Niihara
Journal of the Japan Society of Powder and Powder Metallurgy, **42** (1998) 1207-1210.

3) Synthesis and Mechanical/Magnetic Properties of Nano-Grained Iron-Oxides Prepared with an Inert Gas Condensation and Pulse Electric Current Sintering Process
Y.-H. Choa, T. Nakayama, T. Sekino and K. Niihara
Metals and Materials, **5** (1999) 135-139.

4) Synthesis and Magnetic Properties of Nanocluster Composite
T. Nakayama, T. A. Yamamoto, Y.-H. Choa and K. Niihara
Ceramic Transaction (in press).

5) Fabrication of Nano-sized Metal Dispersed Magnesia Based Composites and Related Mechanical and Magnetic Properties
Y.-H. Choa, T. Nakayama, T. Sekino and K. Niihara
The Korean Journal of Ceramics (in press).

6) Powder Preparation and Microstructure for Nano-sized Metallic Iron Dispersed MgO Based Nanocomposites with Ferromagnetic Response
T. Nakayama, Y.-H. Choa, T. Sekino and K. Niihara
Journal of the Ceramic Society of Japan (in contribution).

7) Structure and Magnetic Properties of Iron Oxide Dispersed Silver Based Nanocluster Composite
T. Nakayama, T. A. Yamamoto, Y.-H. Choa and K. Niihara
Journal of Material Science (in contribution).

List of Supplementary Publications

1) Control of Preferred Orientation and Magnetic Property of Mn_2Sb Thin Films Fabricated by Solid State Reaction
T. Nakayama, T. Matsui and K. Morii
Journal of the Japan Society of Powder and Powder Metallurgy, **43** (1996) 955-960.

2) （解説）磁気冷凍機能をめざす新しいナノ複合材料の展望
山本 孝夫、中山 忠親、新原 晧一
ニューセラミックス, **5** (1998) 9-14.

3) Iron-Oxide / Silver Nanocomposite Produced by Inert Gas Condensation Process
T. Nakayama, T. A. Yamamoto, Y.-H. Choa and K. Niihara
Proceedings of First Asian-Australasian Conference on Composite Materials, **Vol. II** (1998) 505-1~4.

4) Formation and Structure of Ge and Si Nanoparticles
T. Oku, T. Nakayama, Y. Nozue, T. Hirano, K. Asami, L. R. Wallenberg, K. Niihara, T. A. Yamamoto and K. Suganuma
Proceeding of NCF3 & IMA'99, (1999) 193-196.

5) Formation and Photoluminescence of Ge and Si Nanoparticles Encapsulated in Oxide Layers
T. Oku, T. Nakayama, M. Kuno, Y. Nozue, L. R. Wallenberg, K.Niihara and K. Suganuma
Microelectronic Engineering (in press).

6) Microstructure, Mechanical, and Tribological Properties of Si_3N_4-TiB_2 Composites
H.-J. Kim, S. W. Lee, T. Nakayama and K. Niihara
Korea Ceramic Society Journal (in press).

7) Microstructure, Mechanical, and Tribological Properties of Si_3N_4-TiC Composites
H.-J. Kim, S. W. Lee, T. Nakayama and K. Niihara
Korea Ceramic Society Journal (in press).

8) Magnetic Entropy Change of Nanocomposites Composed of a Silver Matrix and Grains of Iron-Oxide or -Nitride
T. A. Yamamoto, M. Tanaka, K. Shiomi, T. Nakayama, K. Nishimaki, T. Nakagawa, T. Numazawa, M. Katsura and K. Niihara
Proceedings of Material Research Society Symposium (in press).

9) Magnetocaloric Effect of Superparamagnetic Nanocomposite Composed of Iron-Oxide and Silver
T. A. Yamamoto, M. Tanaka, T. Nakayama, K. Nishimaki, M. Katsura and K. Niihara
Journal of Applied Physics (in contribution).

10) Characterization and Optical Properties of Nano-sized Powder of Ceria and Copper Oxide Produced by Inert Gas Condensation Process
T. Nakayama, B. Skarman, L. R. Wallenberg, Y.-H. Choa, T. Sekino, T. A. Yamamoto and K. Niihara (in preparation).

11) Characterization and Catalytic Properties of CeO_2/CuO Nanocomposites Produced by Inert Gas Condensation Process
B. Skarman, T. Nakayama, L. R. Wallenberg, Y.-H. Choa, T. Sekino, T. A. Yamamoto and K. Niihara (in preparation).

Acknowledgment

This work has been carried out under the guidance of Professor Koichi Niihara at the Institute of Scientific and Industrial Research (ISIR), Osaka University. The author would like to express his grateful gratitude to Professor Koichi Niihara for his kind guidance, helpful suggestions and invaluable encouragements throughout this work. The author is would like to thank Professors Yasushi Kai and Seiichi Tagawa at Department of Materials Chemistry for reviewing this thesis and their helpful advice.

The author is very grateful to Professor Takao A. Yamamoto at Osaka University for his impressive instructions and suggestion. The author very much appreciates to Drs. Tohru Sekino, Yong-Ho Choa, Takafumi Kusunose and Atsuo Koreeda at Professor Niihara's group and Dr. Satoru Ueda for their helpful discussion, guidance and encouragement throughout this work.

The author thanks to Professor Lars Reine Wallenberg at Lund University, Professor Horst Harn at Darmstadt Institute of Technology, Professor Dong-Woo Shin at Kyongsang National University and Professor Soo Wohn Lee at Sun Moon University for their helpful discussion, guidance and encouragement.

The author wishes to make grateful acknowledge to Professors Yutaka Nakayama, Kenji Morii, Taichiro Ito, Kiyohito Okamura and Ryuichiro Oshima and all other members in their research groups at Osaka Prefecture University for giving the opportunity to come to Osaka University and their hearty encouragement.

Acknowledgment are given to Professors Katsuaki Suganuma, Yoshihiko Hirotsu and Takeo Oku and Drs. Ken-ichi Ota, Tadakatsu Ohkubo, Shuuhei Seki, Masahiro Inoue, Hidekazu Tanaka, Takeshi Hanada and Takashi Nakagawa and Mr. Michiaki Kakuichi, Mr. Noriyuki Ogawa, Mr. Tamotsu Yamamoto, Mr. Masayoshi Ohnishi, Mr. Hiroaki, Matsukawa, Mr. Takanori Tanaka, Mr. Katsuhiro Nishimaki, Mr. Kazuhiro Shiomi, Mr. Masato Tanaka, Mr. Kazushi Asaka and Mr. Kazuhisa Sato at Osaka University for their experimental help and helpful advice.

The author wishes to make acknowledge to Professor Jitendra P. Singh at Argonne National Laboratory, Mr. Bjorn Skarman at Lund University, Professor Atsushi Nakahira at Kyoto Institute of Technology, Professor Henryk Morawiec at Silesian University, Professor Jackie Y. Ying at the Massachusetts Institute of Technology, Mr. Atsufumi Hirohata at University of Cambridge, Drs. Tatsuki Ohji, Masanobu Awano, Yoshikazu Suzuki, Jian-Feng Yang and Hiroyuki Hayashi at National Industrial Research Institute of Nagoya, Drs. Ichiro Matsubara and Ryoji Funahashi at Osaka National Research Institute, Dr. Ken-ichi Kakimoto at Max-Planck-Institut für Metallforschung, Dr. Takabumi Minamisawa at IBM Research, Tokyo Research Laboratory and Mr. Hiroki Kasumi at Carnegie Mellon University for their helpful advices and encouragements.

The author wish to express his great gratitude to The Mitsubishi Trust Yamamuro Memorial Scholarship Foundation, The Nakanishi Scholarship, The Japan Scholarship Foundation (Nihon Ikueikai), Sasakawa Scientific Research Grant from The Japan Science Society, Research Fellowships of Foundation Advanced Technology Institute, Osaka Kogyo-Kai and Fundation For C&C Promotion for providing generous financial support and facilities for studying.

And, many thanks would be extended to Ms. Emiko Kitaura and Ms. Rie Suehiro for their hearty encouragements and helpful assistance. The author thanks to the author's colleagues Dr. Manwar Hussain, Dr. Doh-Hyung Riu, Mr. Yamato Hayashi, Mr. Chunliang Li and all other members of Professor Niihara's group for their friendships and helps.

Finally, the author wishes to express the deep appreciation to the author's parents, grand mother, brothers and best freiends, Hitoyoshi Nakayama, Hiroko Nakayama, Syukuko Sasaki, Syozo Nakayama, Yoshinori Nakayama, Masaki Nagano and Keiichi Niwa for their hearty encouragements, understandings and support.

Tadachika Nakayama

Tadachika NAKAYAMA

January, 2000

Osaka, JAPAN